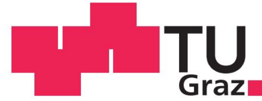

Manuel Kleinbichler, B.Sc.

Investigation of Al Diffusion in Thin Polycrystalline Cu Films by SIMS Analysis and FEM Simulations

Diplomarbeit

zur Erlangung des akademischen Grades

Diplom-Ingenieur

Masterstudium Technische Physik

eingereicht an der

Technischen Universität Graz

Betreuer

Sprengel, Wolfgang, Assoc.Prof. Dipl.-Phys. Dr.rer.nat.

Institut für Materialphysik

in Kooperation mit Infineon Technologies Austria AG

Graz, Februar 2018

EIDESSTATTLICHE ERKLÄRUNG

Ich erkläre an Eides statt, dass ich die vorliegende Arbeit selbstständig verfasst, andere als die angegebenen Quellen/Hilfsmittel nicht benutzt und die den benutzten Quellen wörtlich und inhaltlich entnommenen Stellen als solche kenntlich gemacht habe. Das in TUGRAZonline hochgeladene Textdokument ist mit der vorliegenden Diplomarbeit identisch.

Datum	Unterschrift

Kurzfassung

In dieser Arbeit wurde die Diffusion von Al in Cu und Reaktions-Diffusions-Prozesse im Al-Cu System untersucht sowie deren theoretische Simulation durchgeführt. Cu und Al wurden zusammen mit TiW, was als effektive Barriere für Diffusion von Cu in Si gilt, auf Si auf Waferbasis mittels Magnetronsputtern (PVD) abgeschieden. Es wurde der Einfluss der unterschiedlichen Prozessparameter (Druck, Substrattemperatur) auf die Kornsstruktur und die Korngröße des abgeschiedenen Kupfers mittels AFM- und FIB-Analysen untersucht und mit den theoretischen Vorhersagen aus Thorntons Diagramm verglichen. Um Diffusionsprozesse und Phasenbildung im Al-Cu System zu untersuchen, wurden Proben zwischen 100 °C und 300 °C für unterschiedliche Zeiten getempert und mittels ToF-SIMS depth profiling untersucht. Klassische Diffusion wurde bis zu einer Temperatur von ca. 175 °C beobachtet, was als Grenztemperatur angesehen werden kann, bevor Phasenbildung einsetzt. Unter Verwendung der Softwarepakete Python mit FEniCS wurden die gemessenen ToF-SIMS Tiefenprofile mit Hilfe der Fick'schen Diffusiongleichung sowie dem semiempirischen Gray-Scott Modell simuliert. Die Simulationen zeigten eine präferentielle Phasenbildung an den Korngrenzen, was durch nanoSIMS-Untersuchungen experimentell belegt werden konnte.

Abstract

During this thesis diffusion of Al in Cu and Al-Cu reaction diffusion processes as well as their theoretical simulation were studied. Cu and Al together with a TiW layer as an effective barrier for diffusion of Cu in Si were deposited on Si wafers using magnetron sputtering (PVD). The effects of varying process parameters (pressure, substrate temperature) on the Cu grain structure and the size according to Thornton's diagram were investigated using AFM and FIB. Annealing processes within a temperature range from 100 °C to 300 °C were performed in order to trigger diffusion processes and phase formation that were analyzed using ToF-SIMS depth profiling. Diffusion only was observed till a temperature of approximately 175 °C that can be seen as the limiting temperature before phase formation starts. Using the software packages of Python and FEniCS, the ToF-SIMS depth profiles were simulated using the Fickian diffusion equation and the semiempirical Gray-Scott model to describe reaction diffusion. The simulations showed, that phase formation preferentially takes place at grain boundaries which was confirmed experimentally by using nanoSIMS imaging.

Acknowledgements

At this point, I want to give sincere thanks to all the people helping and assisting me during several steps at this thesis.

Writing a thesis is more than just working in the lab and that's the reason, why my biggest thank goes to Dr. Stefan Krivec, my supervisor at Infineon. As a mentor and an ideal in some way, he provided me a professional working environment, enabled me possibilities to work with superior analytical and processing tools, gave advice in any kind of issue, promoted my work so that I got the chance to present my thesis in front of a wider audience and a lot more that simply cannot be brought to paper. Together with the theoretical input by Prof. Wolfgang Sprengel, my supervisor at Graz University of Technology, I got the opportunity to get a great overview and deeper understanding of diffusion-reaction processes and their importance in industry.

Furthermore I want to thank my dad Reinhard Kleinbichler who inspired my interest in technology through his everyday work at Infineon for more than 20 years, what influenced myself to study technical physics and made this all even possible. He was the one who talked to my manager Alexander Binter 3 years ago, what opened the opportunity for writing my bachelor's and now my master's thesis. For any kind of problem I had, Alex had a solution and I am really thankful for that.

Many colleagues at Infineon assisted me during the last 9 months. Just to mention some, Werner Salzmann provided the lab furnaces for annealing experiments, Ralph Perdacher, Wolfgang Krammer and Pieber Daniel helped me with sawing and YY Tan as well as Sergey Ananiev assisted me with fruitful discussions about reaction processes and their simulation in Al-Cu layer system. There are even more who became much more than colleagues during the time and made this a great experience and therefore, thanks to all of them.

Another important part in terms of analytics regards people in Vienna. First of all, the students Andreas Amsüss and Stefan Schwab as well as their supervisor Prof. Herbert Hutter from Vienna University of Technology are gratefully acknowledged for providing their support with ToF-SIMS measurements and discussions. Another person I want to mention is Arno Schintlmeister from the University of Vienna who gave me the chance to work 3 days at a nanoSIMS tool.

For simulation and nanoIndentation, my colleagues at KAI have to be mentioned as well. A special thank goes to Mirko Bernardoni for giving me a great introduction to FEM and ANSYS and Johannes Zechner for performing and interpreting the nanoIndentation measurements as well as Michael Nelhiebel who made this cooperation even possible.

Last but not least, I had to fight several troubles concerning hard- and software problems during simulation. Many of those problems would not have been solved without the help of my brother Patrick Kleinbichler, providing me support in any kind of computational issue.

A master's thesis does not always stay at company and thoughts about work often followed me home. That is where I have to give special thanks to all my friends and family, who supported me at any time. Beside my brother and my dad especially my mother Andrea, grandfather Andreas, grandmother Irmgard and my beloved girlfriend Magdalena. Without all of you, mentioned or not, that would not have been possible in that way - Thank you!

Contents

1 Introduction **1**

2 Basics **3**

2.1 Example for a Reaction-Diffusion System: The Al-Cu System 3
2.2 The Ni-Cu and Ag-Cu System 4
2.3 Diffusion in Solids 6
2.4 Thornton's Diagram 14

3 Experimental Methods **16**

3.1 Sputter-Deposition 16
3.2 Physical Analytics 19
3.2.1 Secondary Ion Mass Spectroscopy (SIMS) 19
3.2.2 Imaging 23
3.3 Mechanical Characterization 27
3.3.1 nanoIndentation 27

4 Computational Methods and their Implementation **29**

4.1 Finite Difference Method (FDM) 29
4.2 Finite Element Method (FEM) 33
4.2.1 Basics of the Finite Element Method 33
4.2.2 Application of the FEniCS Package for Python and Additional Software 36
4.2.3 The Diffusion Model - Simulation via FEM 36
4.2.4 The Diffusion-Reaction Model - Simulation via FEM 39

5 Experimental Results **41**

5.1 Sample Description and Synthesis 41
5.2 Initial Characterization 43
5.3 Diffusion-Reaction Investigation in Al-Cu system 46
5.4 ToF-SIMS Depth Profiling 47
5.5 Phase Formation in Al-Cu system 54
5.6 Determination of the temperature dependence for Al-Cu Diffusion using FDM 58
5.7 Mechanical Characterization 60
5.8 NanoSIMS Investigations 62

6 Simulation Results 72

6.1 The Diffusion Model for a NiV-Cu and Ag-Cu 72

6.2 The Diffusion-Reaction Model 86

7 Summary 91

References 93

Appendix 96

Python-Code for Diffusion Simulation Using FEniCs 96

Python-Code for Diffusion-Reaction Simulation Using FEniCs 99

1 Introduction

Semiconductor devices are nowadays one of the fundamental parts of modern technology and their application. Everyone knows terms like transistors, capacitors or diodes that are simplifying our lives in many different ways: efficient working, system controls and many more. And not only in terms of assisting our everyday life, semiconductor devices are also fundamental for several security applications.

Infineon Technologies is one of world's leading companies in semiconductor industry with the main objective of producing semiconductor devices such as computer chips for various applications. From the chip in the ATM card to the airbag sensor in modern cars there is a wide range of applications, but they all have on thing in common: a high level of quality and security at any time and condition has to be ensured. In terms of efficiency, the development goes into a distinct direction - smaller in size and stronger in terms of reliability and efficiency.

Material properties are essential for the function and the reliability of semiconductor devices. Cu metallizations on Si wafers are nowadays frequently used, often in contact with a layer of Al. When applied, those layers often have to resist high temperature over long time ranges, what enables diffusion and reaction processes. To estimate the effects on reliability and functionality during the lifetime of semiconductor devices, a detailed knowledge of diffusion processes, possible phase formation and influence on material properties is necessary.

In chapter 2, the basic knowledge for understanding this thesis is discussed. At first, a quick introduction to the theory of diffusion according to the textbook by Helmut Mehrer [1] is given, discussing the basics of bulk diffusion, grain boundary diffusion, different diffusion regimes, equations and approximations. Additionally, phase diagrams [2, 3] for Al-Cu, Cu-Ni and Ag-Cu are shown to see the difference between material systems with expected diffusion-reaction and systems, where almost no reaction is observed. Furthermore, Thornton's diagram [4] as one of the pioneer works regarding the influence of temperature and pressure on the structure of a material is presented leading then to the description of the principle of magnetron sputtering.

Chapter 3 explains several analytics used during this work starting with a description of sputter deposition as a Physical Vapour Deposition (PVD) process used for creating thin films. For characterization, physical analytics like Secondary Ion Mass Spectroscopy (SIMS)

or Transmission Electron Microscopy (TEM) are necessary and presented briefly in this part of this work.

Chapter 4 deals with the basics of the simulation part of this thesis. The Finite Difference Method (FDM) and the Finite Element Method (FEM) were the numerical methods used and the fundamentals are described at first. Due to it's mathematical complexity, only the rough and necessary basics of FEM are described to understand the background of the simulation. The software used for simulation is the FEniCS [5] package for Python, an open source program for creating FEM simulations close to mathematical formulation. Weak forms of equations are a fundamental part for setting up a simulation and therefore, two sections deal with the derivation of weak forms for diffusion and diffusion-reaction equations.

Chapter 5 of this thesis is about experimental facts and analytical results. Deposition parameters, annealing conditions as well as Cu grain size and structure are discussed. The second section takes a closer look at Time-of-Flight Secondary Ion Mass Spectroscopy (ToF-SIMS) results and phase formation processes. Additionally, nanoSIMS images for determining diffusion paths and nanoIndentation results for characterizing mechanical properties of the layer are shown and discussed.

Finally, chapter 6 presents the results of the FEM simulation and tries to explain ToF-SIMS results and FIB/TEM images from a theoretical point of view. The final comparison of theory and experiment tries to give possible explanations for diffusion-reaction phenomena in Al-Cu thin films.

2 Basics

There is a wide range of possible applications for metallizations. Al, Cu and Ni are frequently used materials in, e.g., semiconductor devices, and are often part of ternary systems as well. In every application, the properties of it's base materials play an important role and are responsible for the functions of the device. These properties can immediately change with starting diffusion or formation of IMC. For material systems like Al-Cu, a lot of different IMC phases exist and all of them have different functions. In terms of reliability, a detailed knowledge of phase formation and diffusion processes is important for semiconductor industry.

2.1 Example for a Reaction-Diffusion System: The Al-Cu System

The complexity of reaction-diffusion processes in the Al-Cu system can be already estimated by a look at the phase diagram showing a wide variety of possible intermetallic compounds [2]:

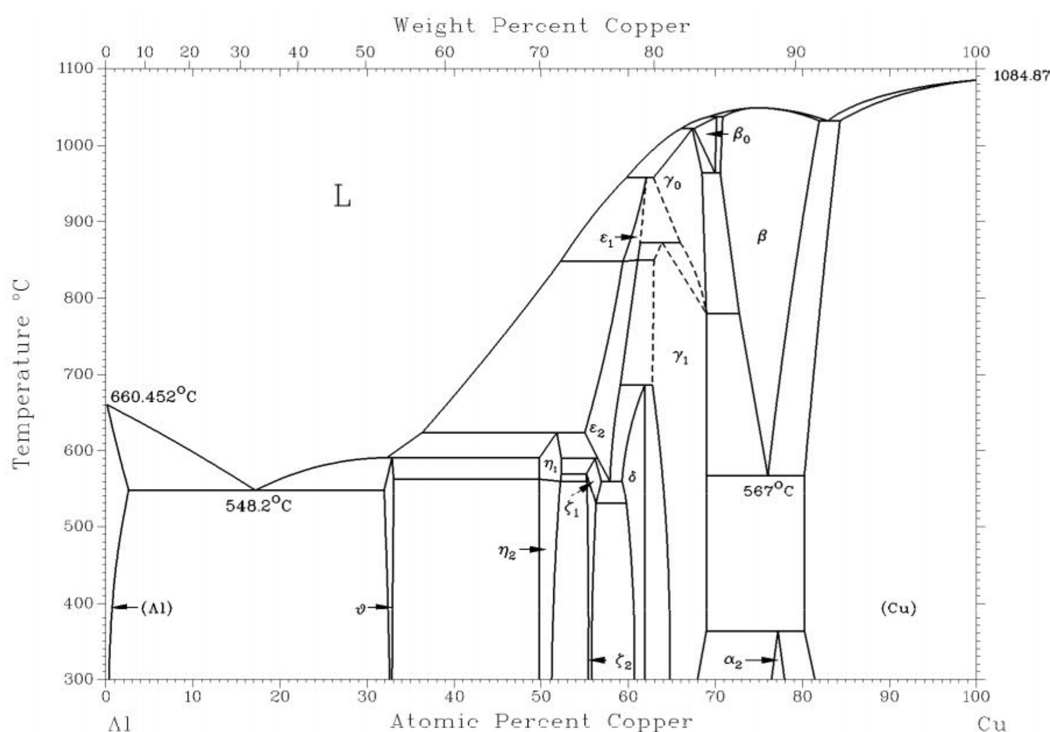

Fig. 2.1: The phase diagram of the Al-Cu system [2]: The binary phase diagram shows the formation in dependency of temperature and element composition

It has to be taken into account, that this phase diagram is for temperatures above 300 °C. Experiments in thesis have been performed in the temperature regime from 100 °C to 300 °C.

Phases in this temperature regime have been studied by YY Tan et al. [6]. Due her studies, Al-rich phases form first, getting replaced by Cu-rich phases with increasing temperature. The two notable phases in this phase diagram for this thesis are the Θ-phase (Al_2Cu) with a composition of 31.9 to 33.0 at% Cu and the γ_1-phase (Al_4Cu_9) with 62.5 to 69.0 at% Cu. As seen in Fig. 2.1, there are many possible phases as soon as the temperature is high enough. For more information, the collection of phase diagrams by Massalski [2] and advanced literature mentioned therein are recommended.

2.2 The Ni-Cu and Ag-Cu System

To investigate diffusion only, reaction processes and other disturbing effects should be eliminated as far as possible. Therefore, an appropriate temperature range and/or an almost reactionless system are necessary. Due to the fact, that diffusion in Al-Cu is hard to investigate because of starting phase reaction at 175 °C, alternative material systems were chosen additionally. Important in semiconductor industry are also the Ni-Cu and the Ag-Cu system:

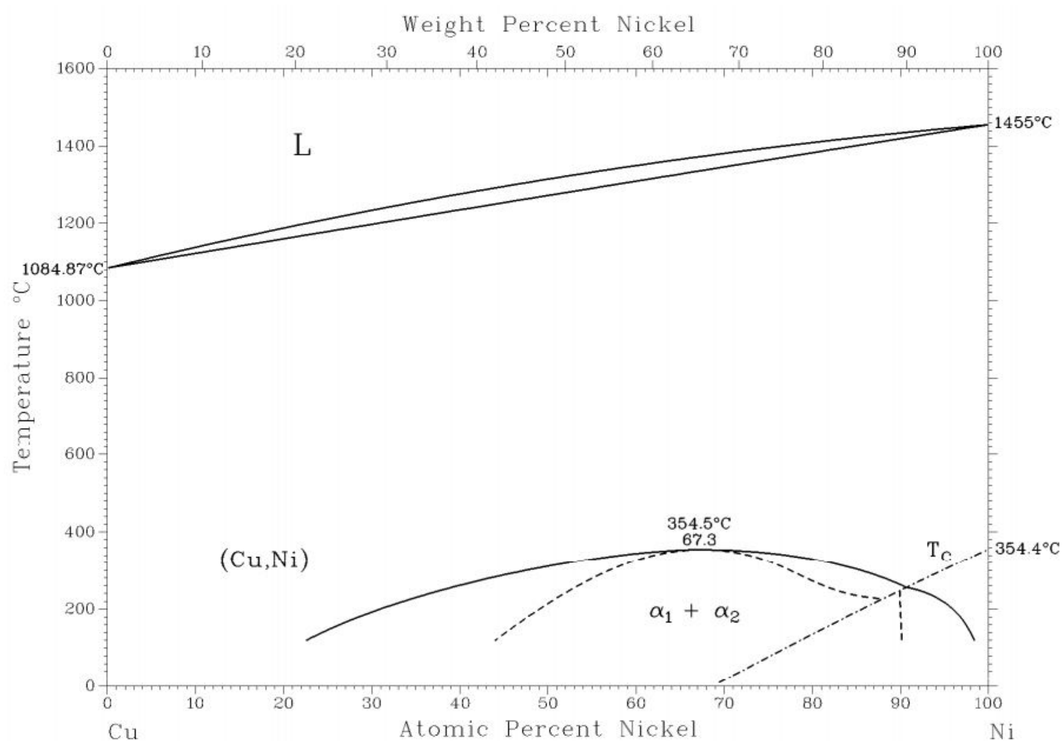

Fig. 2.2: The phase diagram of the Ni-Cu system [2]: The binary phase diagram shows the formation in dependency of temperature and element composition

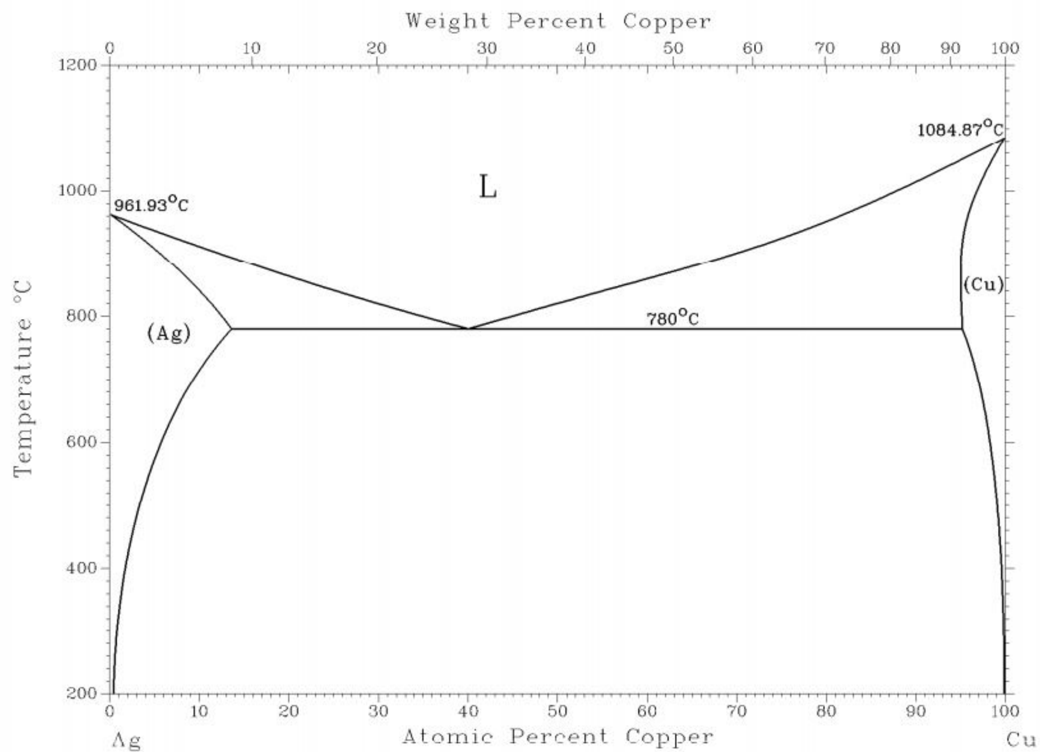

Fig. 2.3: The phase diagram of the Ag-Cu system [2]: The binary phase diagram shows the formation in dependency of temperature and element composition

The Ni-Cu system is completely miscible to high temperatures and the Ag-Cu system shows according to Massalski [3] no phase formation. The Ni-Cu system encounters a phase separation at 354.5 °C and 67.3 at% Cu to form α_1 and α_2. Due to their thermal stability, those systems are predestined for bulk and grain boundary diffusion investigations, which were already performed by Divinski et al. [7, 8]. The tabulated values therein were used to set up the diffusion simulations.

2.3 Diffusion in Solids

General

Transport processes are important in several parts of physics. Whether there is convection, heat flux, heat radiation, transport of liquids or the transport of charged particles in electrical conductors, all those processes are described by **transport equations**. The best known equation in that context is Ohm's Law ($U = R \cdot I$). The easiest way to write down a transport equation for constant coefficients is:

$$\vec{v} \cdot \nabla u(x) = f(x) \tag{2.1}$$

Hereby, a function *f(x)* will be described by the gradient ∇ of another function *u(x)* and a proportionality constant or function $\vec{v}$.

But where in this context is diffusion in solids? Diffusion in solids is also a type of material transport and can be described by a transport equation as well – the Diffusion equation introduced by Adolf Fick in the 19th century.

The Fickian laws are the basics for several diffusion processes in solids and describe the transport of material as an empirical issue. Adolf Fick introduced the concept of a diffusion coefficient and proposed a linear relationship between the flux of particles and the concentration gradient in a mixture of salt and water (this work was treated by Josef Fourier earlier for the convection of heat). This approach is a macroscopic one neglecting atomic mechanisms. A different understanding of diffusion in solids is based on the "Random Walk Theory" and atomic mechanisms of diffusion. [1]

In isotropic media, physical and chemical quantities are independent of the direction, in contrast to the anisotropic case, where favored directions appear. For example diffusion in gases, most liquids, glass-like solids, polycrystalline materials without texture, ikosaeder-like quasicrystals and cubic crystals is isotropic.[1]
Especially for technical applications, materials with cubic crystal structure are important. Examples therefore are face-centered-cubic metals (fcc: Cu, Au, Al, Ni ...), body-centered-cubic metals (bcc: W, β-Ti, ...) and particularly for semiconductor industry the elemental semiconductors Si and Ge with their cubic diamond structure.

First Fickian Law

The mass flux of diffusing particles, e.g. atoms, molecules or ions, is a vector quantity $\vec{J}(x, y, z)$ in 1, 2 or 3 dimensions. It is defined as mass of diffusing material flowing through a unit area per time. The direction of the flux is in general chosen parallel to the normal vector of this unit area. Fick proposed, that the mass flux is proportional to the concentration gradient, what enabled the possibility to formulate the **1st Fickian law** in isotropic media as a transport equation. If *v* in Eq. 2.1 is substituted by *D*, *u(x)* by the concentration *C* and *f(x)* by the particle flux *J*, this leads to [9]:

$$J_x = -D\frac{\partial C}{\partial x}$$
$$J_y = -D\frac{\partial C}{\partial y} \tag{2.2}$$
$$J_z = -D\frac{\partial C}{\partial z}$$

The minus-sign considers the fact, that flux and concentration gradient are pointing in opposite directions. The 3-dimensional generalization is finally:

$$\vec{J} = -D\nabla C \tag{2.3}$$

The proportionality constant defines the diffusion coefficient D.

Continuity Equation

The next step for a successful description of diffusion in solids is the validity of the **continuity equation**. In general, the particle number in diffusion processes is constant, which implies, that there are no internal sources and sinks for the diffusing components. If that is not the case, an additional term must be introduced to ensure that the particle number stays constant. This fact leads to the formulation of the continuity equation.

Therefore, a random point *P = (x,y,z)* is chosen. The flux $\vec{J}$ varies in a test volume with a size of Δx, Δy and Δz. If the inflow into the volume doesn't compensate the outflow anymore, an 'accumulation' or 'loss rate' has to appear. In mathematical formulation, this means [1, 9]:

$$\begin{aligned} [J_x(P) - J_x(P + \Delta x)] \cdot \Delta y \Delta z &+ \\ [J_y(P) - J_y(P + \Delta y)] \cdot \Delta x \Delta z &+ \\ [J_z(P) - J_z(P + \Delta z)] \cdot \Delta x \Delta y \ &= \ loss\ rate \end{aligned} \tag{2.4}$$

The expansion of the flux components in a Taylor series leads to:

$$-\left[\frac{\partial J_x}{\partial x} + \frac{\partial J_y}{\partial y} + \frac{\partial J_z}{\partial z}\right] \Delta x \Delta y \Delta z = \frac{\partial C}{\partial t} \Delta x \Delta y \Delta z \tag{2.5}$$

The part of this equation in the brackets can be identified as the flux divergence, what finally creates the known form of the continuity equation [1, 9]:

$$-\nabla \cdot \vec{J} = \frac{\partial C}{\partial t} \tag{2.6}$$

Second Fickian Law

Combining the 1st Fickian law (Eq. 2.3) with the continuity equation (Eq. 2.6) leads to a form of **Fick's 2nd law**.

$$\frac{\partial C}{\partial t} = \nabla(D \nabla C) \tag{2.7}$$

Mathematically, this is a 2nd order partial differential equation. If the diffusion coefficient is concentration independent (e.g. in ideal and homogeneous systems), the equation simplifies to:

$$\frac{\partial C}{\partial t} = D \Delta C \tag{2.8}$$

This form of Fick's law is also known as 'linear diffusion equation'. It combines dependencies in space and time. Due to the fact that the diffusion equation is a 2nd order equation, 2 initial or boundary conditions are needed, to find solutions for a concentration field *C(x,y,z,t)* [1, 9].

Symmetries in the geometry of the diffusion problem can sometimes be used for simplification. These are for instance [9]:

Linear flow for $D =$ const:

$$D \frac{\partial^2 C}{\partial x^2} = \frac{\partial C}{\partial t} \tag{2.9}$$

Linear flow for $D =$ variable:

$$\frac{\partial}{\partial x}\left(D\frac{\partial C}{\partial x}\right) = \frac{\partial C}{\partial t} \tag{2.10}$$

Axial symmetric flow for $D =$ const.:

$$D\left(\frac{\partial^2 C}{\partial r^2} + \frac{1}{r}\frac{\partial C}{\partial r}\right) = \frac{\partial C}{\partial t} \tag{2.11}$$

Axial symmetric flow for $D =$ variable:

$$\frac{1}{r}\frac{\partial}{\partial r}\left(rD\frac{\partial C}{\partial r}\right) = \frac{\partial C}{\partial t} \tag{2.12}$$

Spherical symmetry for $D =$ const.:

$$D\left(\frac{\partial^2 C}{\partial r^2} + \frac{2}{r}\frac{\partial C}{\partial r}\right) = \frac{\partial C}{\partial t} \tag{2.13}$$

Spherical symmetry for $D =$ variable:

$$\frac{1}{r^2}\frac{\partial}{\partial r}\left(r^2 D\frac{\partial C}{\partial r}\right) = \frac{\partial C}{\partial t} \tag{2.14}$$

Analytical solutions for those equations are practically uncommon and only possible for specific initial and boundary conditions. One possibility contains an instant, flat source with the initial condition C_0 distributed like the Dirac delta function $\delta(x)$, which leads to the **thin-film solution**:

$$C(x,t) = \frac{M}{\sqrt{\pi D t}} \cdot exp\left(-\frac{x^2}{4Dt}\right) \tag{2.15}$$

According to its shape, this solution is often called the **Gaussian solution**.

$$\int_0^\infty exp(-pt)\frac{\partial c}{\partial t}dt = D\int_0^\infty exp(-pt)\frac{\partial^2 c}{\partial t^2}dt \tag{2.16}$$

Another analytical solution can be found for a constant surface concentration in a semi-infinite medium (x $>$ 0). With the application of a Laplace transformation, the problem can be rewritten in an integral form [10].

The boundary conditions $c(x = 0) = c_s$ and the inverse Laplace transform leads to a

solution with the complementary error funtion (erfc)[10]:

$$c = c_s \cdot erfc\left(\frac{x}{2\sqrt{Dt}}\right) \tag{2.17}$$

If D is concentration dependent, the diffusion equation is a non-linear partial differential equation. The dependent diffusion coefficient in this case is the "interdiffusion coefficient". For that case, the equation is mostly not solvable analytically, what leads to the application of numerical methods such as the Finite Difference Method (FDM) or the Finite Element Method (FEM) [1].

Bulk Diffusion, Grain Boundary Diffusion and Diffusion Regimes

The methods explained above show, how to treat the diffusion problem in general. In polycrystalline materials, diffusion takes place into the bulk and also along the grain boundaries. Experiments showed that the diffusion ratio at low temperature can be magnitudes higher in the grain boundaries than in the bulk. Another point is the orientation of the grains, which affects the diffusion process along those crystal defects [11].

In contrast to bulk diffusion, grain boundary diffusion in solids is more complex. To consider all possible effects on grain boundary diffusion, a characterization of the problem is important. One possibility is the classification by Harrison [12], where 3 regime types (A, B and C) are introduced. Those describe the different options for the diffusion lengths between bulk and grain boundary diffusion. The classification by Harrison is the most common one for polycrystals [1].

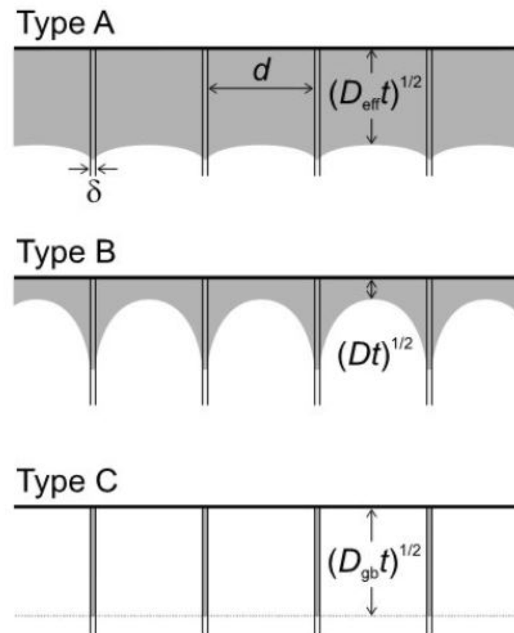

Fig. 2.4: Schematic representation of Harrison's classification for polycrystals [1]
A, B and C mark the different regime types, δ is the grain boundary width and d the distance between two neighbouring grains.

For this thesis, B- and C-regime have the highest importance. Due to complexity, B-regime diffusion will be described in more detail.

Type A diffusion appears at high temperatures, for really long diffusion times and/or large grains under the following condition:

$$\sqrt{Dt} \geq \frac{d}{8} \tag{2.18}$$

With the bulk diffusion coefficient D, the annealing duration t and the grain width d.

Here, in diffusion from neighbouring grain boundaries overlap in the crystallites during the run of a diffusion experiment. Therefore, neighbouring grain boundaries cannot be treated as isolated, what leads to a weighted, effective diffusion coefficient for bulk and grain boundary diffusion combined.

Kinetics for B-regime is mostly found in diffusion experiments with moderate temperature and annealing time. Furthermore, materials with large grain size tend to favor type B diffusion

processes. The criterion for type B kinetics is [1]

$$s\delta << \sqrt{Dt} << d \tag{2.19}$$

with the segregation factor s, the grain boundary width δ, the bulk diffusion coefficient D, the annealing duration t and the grain width (or distance between to neighbouring grain boundaries) d.

In this model, diffusion in one grain boundary does not affect the diffusion processes in the neighboring one. Mathematically, the grain boundaries can be treated as isolated from each other. Starting from Fickian diffusion, one can create an equation for 2 grains separated by a grain boundary with the width δ. This leads in the 2-dimensional case to [10]:

$$\frac{\partial c}{\partial t} = D\left(\frac{\partial^2 c}{\partial y^2} + \frac{\partial^2 c}{\partial z^2}\right) \tag{2.20}$$

$$\frac{\partial c_{gb}}{\partial t} = D\left(\frac{\partial^2 c_{gb}}{\partial y^2} + \frac{\partial^2 c_{gb}}{\partial z^2}\right) \tag{2.21}$$

In general, this problem is a 3-dimensional one. Here, it is reduced to the x-y plane, while the x-z plane is the grain boundary plane. Under the assumption, that the grain boundary width is small compared to the bulk and that $D_{gb} >> D$, an equation for grain boundary diffusion can be created, where bulk and grain boundary diffusion are coupled [10].

$$\frac{\partial c_{gb}}{\partial t} = D_{gb}\frac{\partial^2 c_{gb}}{\partial y^2} + \frac{2D}{\delta}\frac{\partial^2 c}{\partial z^2} \tag{2.22}$$

The credit for the exact solution of this problem goes to Whipple [13]. But due to the fact, that an exact solution can cause problems for practical applications, Le Claire published a numerical solution with the additional variable β [14, 15].

$$\beta = \frac{(\Delta - 1)\delta}{2\sqrt{Dt}} \cong \frac{D_{gb}}{D} \cdot \frac{\delta}{2\sqrt{Dt}}; \quad \Delta = \frac{D_{gb}}{D} \tag{2.23}$$

Le Claire showed, that grain boundary diffusion for $\beta > 10$ gets basically independent from β itself. In a plot concentration vs. width to the power of (6/5), the GB diffusion can be approximated linearly. This leads to following equation for the GB diffusion coefficient.

This equation shows importance for practical problems, where solution like the exact one

of Whipple cannot be found. [15]

$$\delta D_{gb} = 1.322\sqrt{\frac{D}{t}}\left(-\frac{\partial ln(\bar{c})}{\partial z^{\frac{6}{5}}}\right)^{\frac{5}{3}} \tag{2.24}$$

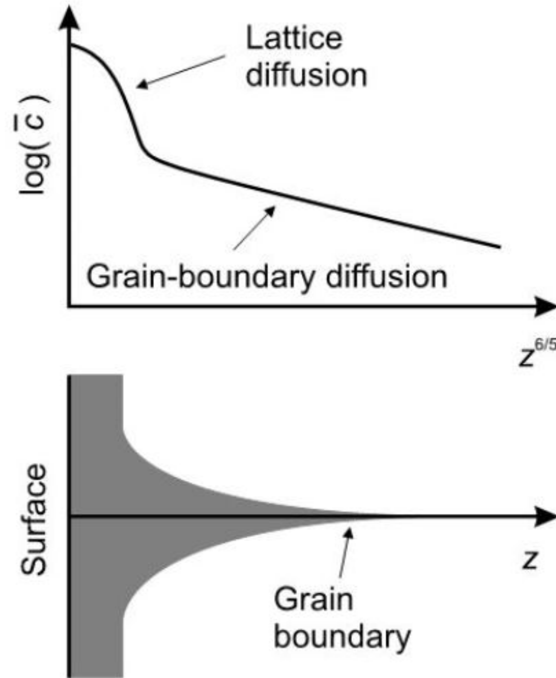

Fig. 2.5: Theoretical concentration curve (log(c)) for diffusion processes in solids with bulk and grain boundary diffusion in dependency of the distance z ($z^{\frac{6}{5}}$) from the surface [1]
In the grain boundary zone, the linear slope proposed by Le Claire can be recognized [14]

At lower temperature or for very short diffusion times, type C diffusion appears. For that regime, diffusion only takes place along the grain boundaries under the condition:

$$\sqrt{Dt} << s\delta \tag{2.25}$$

With grain boundary diffusion coefficient D_{gb}, annealing duration t, segregation factor s and grain boundary width δ. For this regime, the concentration is proportional to x^2. Therefore, gaussian fits are used as approximation:

$$f(x) = ae^{-\frac{(x-b)^2}{2c^2}} \tag{2.26}$$

with the real constants a, b and c.

2.4 Thornton's Diagram

Sputtering is one of the main physical vapour deposition (PVD) processes and can be used to create thin layers with good uniformity. Due to its complexity, there are many possible parameters that influence the properties of the resulting sputtered film. One of the basic works about the influence of pressure and temperature on the grain structure of a polycrystalline material was done by John A. Thornton [4]. Starting from his paper, many modifications and applications to other systems have been performed (e.g. by Anders 2010 [16])

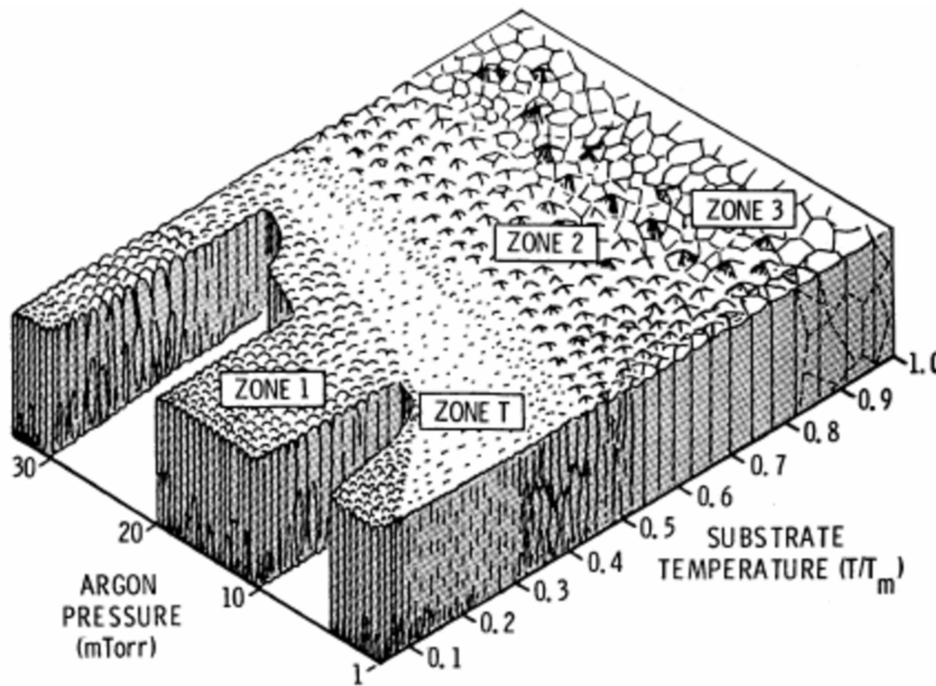

Fig. 2.6: Thornton's diagram [4] relating the resulting microstructure to argon pressure and substrate temperature, e.g., for a sputtering process

This diagram can be divided in 4 different zones (Zone 1, T, 2 and 3 [4]). It shows the expected grain structure in dependency of temperature (substrate temperature) and pressure (argon pressure, e.g., as inert gas). In Zone 1, the grains are very small and almost amorphous. Therefore the substrate temperature has to be small. For Cu with a melting point T_M of 1085 °C, the temperature has to be below 100 °C. For diffusion, this means a higher amount of grain boundaries per area leading to faster diffusion and reaction. Zone T is a transition zone, where grains are growing with temperature increase. The higher the substrate temperature, the larger and more columnar the grains become. This leads to the zones 2 and 3, where the grains orientate themselves columnar. As can be seen in Fig. 2.6 the substrate temperature is the most important parameter. The pressure has a minor

impact. To sum it up, going to higher temperatures leads to a further growth in grain size until the grain structure is finally columnar. The ideal diffusion properties can be reached for columnar grains and grain boundaries.

3 Experimental Methods

For the production and investigation of several metallizations, proper methods are necessary. One possibility to create thin layers with good uniformity is sputter deposition as an example for an physical vapour deposition (PVD) process. PVD processes are using physical interactions between particles to manufacture thin layer systems. For a proper investigation, many physical analytics are available to get information about element composition, atom concentration, grain size and structure or mechanical properties.

3.1 Sputter-Deposition

Sputter-Deposition is a physical vapour deposition (PVD) process and one of the most common methods in thin-film-technology. Hereby, pure material (from the target) or reaction products with the reactive gas in the vacuum chamber can be deposited onto the so-called substrate. With this procedure, conducting as well as non-conducting materials can be coated and the deposition rate can be held quite constant over large areas.

In principle, a setup for sputter deposition consists of an anode, a cathode and an inert gas, e.g., Ar in a vacuum chamber. Anode and cathode create an electric field for accelerating ions in the direction of the $\vec{E}$ field vector. The inert gas serves as a source for ions. The amount of inert gas in the chamber determines the pressure (Ar-pressure p) and is one parameter in Thornton's diagram (2.6, [4]).

If Ar atoms are colliding elastically, there is a probability that an ion is created. Higher temperature in the chamber means higher ion mobility and therefore enhanced collision probability. If the average energy of the ions is higher than the Ar ionization energy, the plasma ignites and sustains afterwards by secondary electrons emitted from the target. The temperature is determined by the power that can be varied in common sputter tools. The temperature of the plasma T_p leads to an increase of the substrate temperature, what is the second and most important parameter for changing grain properties according to Thornton [4].

When Ar ions are hitting the target, a collision cascade is launched and several secondary products are created and emitted: uncharged particles, ions, secondary and backscattered electrons, X-rays and many more. For sputter deposition uncharged particles, ions and secondary electrons are important. Furthermore, the energy distribution of the backscattered

ions is lower than the binding energy of surface atoms (several eV), that no damage underneath the surface appears. Still a small part of the backscattered inert gas (particles, ions, ...) can be found. If the substrate is used as a cathode, sputtering can be used for cleaning the substrate before the deposition process itself [17].

There are 2 common setups: the ion-beam and the glow-discharge setup. For this thesis and the sample production, the glow-discharge setup is important and will be described in advance.

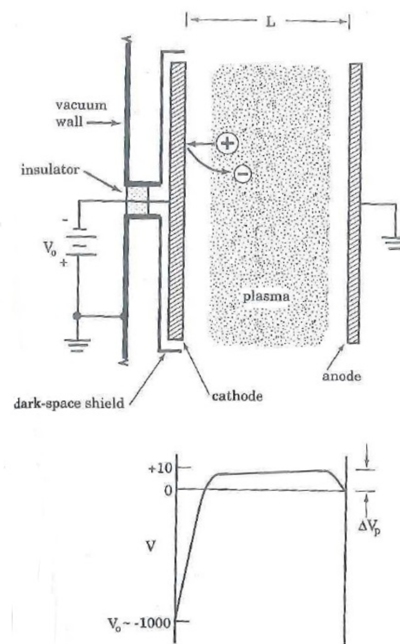

Fig. 3.1: Principle scheme of the glow-discharge setup for sputtering processes [17]

The principle of a glow-discharge sputter tool is described in Fig. 3.1. A modification of this setup works with an additional magnet positioned above the target ("Magnetron Sputtering"). Hereby, charged particles are forced on a cycloid trace due to the electric and magnetic field of the moving magnet. That leads to a higher ionization ability and sputter ratio. Furthermore, the whole setup works at lower pressure, because the plasma ignites easier due to an enhanced collision ratio [18].

In this setup, the target is the cathode while the chamber wall is grounded. The substrate is in general on floating potential. The chamber volume is filled with an inert gas, which can be

mixed with a reactive gas (eg. Ar, N_2 ..., pressure: 10^{-3} – 10 mbar). The self-ionization of argon atoms by application of a voltage is high enough to ignite the plasma. The fact, that the area of the anode is larger than the area of the cathode leads to a voltage drop on the cathode. Through application of a voltage, argon ions are accelerated towards the target and cause a collision cascade there, where many different particles such as secondary electrons (for sustaining of the plasma), secondary ions or uncharged particles are emitted out of the target. Uncharged particles are coating the substrate underneath the target. The size of the particles influences the momentum transfer of the chosen sputter gas to the target. For pure materials such as Cu or Al, this fact has consequences for the overall sputter ratio. In the case of a composite target, e.g., TiW, this leads to the effect of "preferential sputtering". This means, that due to size of the Ar atoms, Ti is more likely to be sputtered than W. After some time, an equilibrium is reached, because the probability to sputter a W atom gets equal to the one of sputtering a Ti atom (less Ti atoms in target anymore). This issue influences the stoichiometric composition of Ti and W on the substrate significantly [17, 18].

One way to manipulate the stoichiometric composition of two different materials is by back-sputtering. During the bombardment of the target, Ar^+ ions can be released in the collision cascade. Due to their charge, these ions are accelerated towards the substrate. Three cases can be distinguished:

- $\underline{\lambda > d_{t-s}}$: If the pressure is low enough (about 10^{-3} mbar), the mean free path becomes longer than the distance target-substrate ($\lambda > d_{t-s}$) and the Ar atoms only lose little energy on their way to the substrate. There they can, analogous to the target, launch a collision cascade, where more likely Ti is to be sputtered. This decreases the Ti percentage in the substrate until equilibrium is reached again, when the probability of sputtering Ti and W are the same [17, 18].

- $\underline{\lambda < d_{t-s}}$: In an unusual case when the pressure is higher (10^{-2} – 10^{-1} mbar), the mean free path is lower than the target-substrate distance ($\lambda < d_{t-s}$). Here, the ions collide with many other particles on their way to the substrate and lose so much kinetic energy, that they are not able to start a collision cascade anymore. In this case and without RF bias, the composition of the two materials on the substrate matches the one of the target.

- Introduction of a RF-bias: Another possibility to change the composition is based on the so-called RF-bias. Between gas and anode there is a particle-free space, the "dark space", which works as a capacitor with the gas as a cathode and Si as an anode.

Between those “capacitor-plates” is a voltage V_p due to a self-bias. By application of a DC-bias, V_p can be increased (Fig. 3.1). As a result, electrons are forced to a sinusoidal vibration the heavier ions cannot follow. This voltage now determines the energy of the backsputtered ions crashing onto the substrate. Higher ion energies lead to more sputtering, what means in case of TiW less Ti in the substrate. Similar to before, this only works as long as equilibrium is not yet reached [17].

3.2 Physical Analytics

Many physical analytics are based on the principle that a beam of particles or waves is shot onto a sample. There, an interaction takes place and secondary signals to be analysed are produced. There a many possible combinations: in Secondary Electron Microscopes (SEM), the primary beam consists of electrons interacting with the sample surface and releasing secondary and backscattered electrons for image formation. In case of Secondary Ion Mass Spectroscopy (SIMS), the primary and the secondary beam consist of ions. In the following chapter, some of the analytics used in this thesis are described.

3.2.1 Secondary Ion Mass Spectroscopy (SIMS)

As already mentioned SIMS is a physical analytical method where a primary ion beam is fired onto the sample surface. Accelerated by a voltage in kV-range, the primary ions start a collision cascade on the surface and near regions underneath. Due to the fact that hard particles are colliding, elastic and inelastic collisions take place so that the conservation of momentum and energy is valid [19]:

$$M_1 \cdot v_1 = m_1 \cdot v_1' + m_2 \cdot v_2' \tag{3.1}$$

$$\frac{1}{2} \cdot m_1 \cdot v_1^2 = \frac{1}{2} \cdot m_1 \cdot v_1'^2 + \frac{1}{2} \cdot m_2 \cdot v_2'^2 \tag{3.2}$$

v_1 and v_2 mark the particle velocity before and v_1' and v_2' after a collision and m_1/m_2 are the masses of the colliding particles. With a certain probability, this collision cascade near the surface can overcome the binding energy of a particle at the surface. Those particles can be ionized as well (with a probability in the range of 10^{-3}). Those knocked out particles are so-called secondary ions. Mass and energy of the primary ions determine the penetration depth of the collision cascades. The number of knocked out particles per primary ion is called the "total sputter yield", Y_{tot}. A fraction of it can be measured in the detector. This quantity is called "useful sputter yield" Y_u. The measured ion intensity is described by the

fundamental SIMS equation [19]:

$$I^{\pm}(A) = z \cdot I_p \cdot c_A \cdot Y_u \tag{3.3}$$

Here, $I^{\pm}(A)$ is the positive or negative secondary ion current of component A in amperes, I_p the primary ion current in amperes, z the atomic number and c_A the concentration of substance A and $I^{\pm}(A)$ is the measurement output. To get quantitative results, c_A of a known sample is necessary for calibration.

As shown by this equation, a SIMS measurement is dependent on several different parameters. To obtain quantitative values, the measured results have to be normalized with external standards (RSF factor) [19]:

$$RSF = \frac{I_M}{I_A} \cdot c \tag{3.4}$$

In principle two different operating modes of SIMS exist:

- static SIMS
- dynamic SIMS

Static SIMS is a surface-sensitive method where very low ion current densities are used (ion current of nA and less). The border between the static and the dynamic method is defined via the static limit, being approximately $10^{13}\ \frac{at}{cm^2}$ of primary ion dose (material dependent). From there on, molecules or various materials are destroyed irreversibly. To prohibit this border, the ion current densities are lowered further by operating in a pulsed mode (pA range). Furthermore, a high lateral resolution is appreciated, leading to the development of liquid metal ion guns (LMIG). Nowadays, typically bismuth (Bi) is used as primary ion source.

To accelerate the knocked out ions toward a detector, an additional acceleration voltage U_a is applied. The particles are accelerated to a specific kinetic energy governed by U_a and separated by masses afterwards. The kinetic energy (E_{kin}) is described by the well-known equation [19]:

$$E_{kin} = \frac{mv^2}{2} = z \cdot e \cdot U_a \tag{3.5}$$

with the particle mass m in kg, the particle velocity v in m/s, the charge z in coulomb, the unit charge e in coulomb and the external acceleration voltage U_a in volts.

Due to high mass resolution and transmission, Time-of-Flight (ToF) detection is the most

common mode for static SIMS. The biggest advantage is the simultaneous acquisition of all secondary ions of a specific polarity. Till a specific mass, the analyzer can detect ions, the signal will be processed afterwards (e.g. conversion in electrons with following amplification, usage of a scintillator, time-digital-converter ...). The result is measured intensity I vs. the mass to charge ratio m/z (mass spectrum).

To enable the possibility of recording depth profiles with ToF-SIMS, the method of "dual beam depth profiling" was developed. This method is destroying the surface, what makes the static method to a quasi-dynamic one. Besides the primary ion gun, a second sputter gun is applied. After every primary ion pulse, a part of the surface is removed. With the combination and change between SIMS analysis and sputtering, depth profiles of samples can be created. O_2^+ and Cs^+ are often used as sputter projectiles to use the advantage of their signal enhancing properties. The measured ToF-SIMS depth profile delivers a distribution intensity vs. sputter time, that can be converted into concentration vs. depth by an appropriate method. [19].

ToF-SIMS's main advantage is the good overview of the ingredients in a sample with a surface-friendly method. The creation of mass spectra or a destruction-free elementary or molecular mapping of the surface is possible, what makes it interesting for applications in biology (e.g. proteins) as well.

The main difference of the **Dynamic SIMS** compared to static one is the use of higher primary ion currents. This enables simultaneous analysis and excavation by one single ion beam. Those beams are in the nA range leading to a surface destruction, but to a generation of higher secondary ion currents. Analyzers in that case are double-focussing sector fields, where secondary ions are energy-filtered within an electric field before being split according to their $\frac{q}{m}$ ratio in a magnetic field. The big advantage to ToF-SIMS is a larger dynamic range with a 2-3 magnitudes lower detection limit. Disadvantages are the destruction of the sample and the fact, that only a few elements can be measured simultaneously. A prior knowledge about the sample and their contents is required. Dynamic SIMS is used for quantitative element analysis, elemental mapping and investigations of interactions between several materials.

An improvement in terms of lateral resolution ($<$ 100 nm) is the **NanoSIMS** method [20]. The theory is analogous to the described one for ToF-SIMS. The main difference here is, that

sputter and measurement beam are the same. That is in general the definition of a dynamic SIMS method. Technically, the nanoSIMS is a dynamic, double focussing, magnetic-sector, multi-collecting ion probe [20].

The fundamental difference that distinguishes this tool from other SIMS instruments is the possibility to create small primary beam diameters (50 nm for Cs^+ ions and 200 nm for O^- ions). Those ions are accelerated from a potential of +/- 8 keV at the source and the same at the sample resulting in an impact at the sample with an energy of 16 keV. A complex set of electromagnetic lenses and electrostatic fields then focus the beam onto the sample surface.

The secondary particles released due to the interaction with the primary beam are reflected in the same direction the primary ions came from. There, a system of electric fields and slits change the direction of the secondary beam towards the detector system. They are entering an electrostatic spherical analyzer, where the secondary ions are split according to their energy. Finally, the beam enters a magnet, where the mass separation takes place. Across the focal plane of the magnet, the detectors are located and the final signal can be recorded. By moving the primary beam across the sample in a raster, isotope distribution images can be created [20].

In comparison to the ToF-SIMS technique, nanoSIMS has a superior mass resolution and is able to measure isotopic compositions of low ion signals. The big advantage of ToF-SIMS are the detections of all secondary ions simultaneously, little sample destruction and preservation and sub-micrometre spatial resolution [20]. Summarized, the ToF-SIMS is good for getting an overview over the material composition of the sample as long as enough ion signal is available. For a more detailed look at the element distribution, imaging and better mass resolution, the nanoSIMS method is the one to choose.

3.2.2 Imaging

Scanning Electron Microscopy (SEM)

One of the most important methods in imaging analytics for many different materials is the scanning electron microscope (SEM). A good introduction of the basics of SEM imaging is given in the book by Goldstein et. al [21]. The physical principle is based on the interaction between electrons and matter. There are two notable interaction processes of the electrons: elastic and inelastic scattering. During those interactions, many different secondary particles are created. The most important for SEM are the secondary electrons (SE), the backscattered electrons (BSE) and the characteristic X-rays (for Energy Dispersive X-ray Spectroscopy - EDX).

A SEM consists of several components: An electron source emits electrons, which are accelerated towards the anode (the sample) in an electric with a defined voltage (typically between 0.1 and 30 keV). The kinetic energy is proportional to the acceleration voltage of the electrons and controls therefore the impact of those particles on the sample. The electron beam is focused through electromagnetic lenses. The spot on the sample (and furthermore the interaction volume and beam damage) is held as small as possible. Therefore, a set of lenses is used. Several condenser lenses bundle the beam before it gets focused on the sample with an objective lens. Because of the EM-field of the inductor, the electron beam can be controlled and moved across the sample. That is a scanning process. Due to the fact that electrons should not collide with other particles on their way to the surface (= large mean free path), the SEM is placed within a vacuum system. This prohibits on the one hand a deflection of the electron beam, on the other hand electrical flashovers, which can destroy tool and sample. The last part are the detectors. In common SEMs, those are detectors for SE, BSE and characteristic X-rays (EDX) [21].

The image formation in the SEM is based on the detection of secondary electrons. During the interaction between the electron beam and the sample, SE are emitted, which can be "collected" by the electrical field of the detector. There, they are hitting a scintillator and a photomultiplier, which enhance the signal and transform it finally. Images can be created by backscattered electrons as well, but the BSE ratio is proportional to the atomic number. Summarized, SE are most suitable for topography contrast and create images similar to light microscope images. BSE show better material contrast and provide additional information about the composition of the sample.

Energy Dispersive X-ray Analysis (EDX)

Additionally to the creation of SE and BSE, several other signals are emitted during the interaction process. The formation of characteristic X-rays resulting from the bombardment of the sample with high-energy electrons leads to the analytic discipline of X-ray spectroscopy. One well known part is the energy-dispersive X-rays analysis (EDX). This method is important for identification of elements and phases with a so-called microprobe [21].

One example for an EDX-detector is the semiconductor detector. Here, the incoming X-ray creates several electron-hole-pairs in semiconductor crystals, e.g., Si(Li) or HPGe. The number of charge carrier pairs is proportional to the energy of the X-rays and can be used for characterization of elements. To suppress effects like diffusion inside the crystal or noise, the whole detector system is cooled. The energy resolution of common EDX-spectrometers is at approximately 100 eV.

Beside the more qualitative investigation with EDX, a more quantitative analysis with higher accuracy is possible as well. At first, the concentration of an element in the sample is proportional to the intensity of the signal. In general, the measured concentration will not be equal to the standard samples, what means, that a correction has to be done. This happens via ZAF correction factors (k_Z, k_A, and k_F)

k_Z considers effects due to the atomic number, k_A effects of a possible absorption of X-rays in the sample and k_F the fact, that X-rays from atom A can lead to fluorescence in atom B.

Focused Ion Beam Techniques (FIB)

Together with electron microscopy, focused ion beam (FIB) techniques became more and more important [22]. Starting as fairly expensive possibility for sample preparation, the improved FIB revolutionized the TEM-sample preparation and became notable as analytical method in industry and science. With this technique, precise cuts through ductile materials are possible, what makes it interesting for investigation of layers and phase formation as well as for the creation of cross-sections.

The standard FIB tool consists of a vacuum system, a "liquid metal ion source" (LMIS, or LMIG), an ion column, a sample holder, detectors, a gas supply system and a computer for controlling the system. The LMIS provides ions for the FIB. It consists of a reservoir, working as a metal source, and a W needle attached. The most common LMIS is gallium (Ga). The LMIS system creates an ion beam with a diameter of about 5 nm. The Ga+ ions are accelerated inside the ion tube with acceleration voltages up to 50 keV. Via an optical system comparable to the one in the SEM, the beam is optimized before hitting the sample. The sample holder can be moved in 3 directions and turned around 2 axes (x,y,z,r and t). Detectors such as multi-channel-plates or electron multipliers are used for image formation. FIBs can be used as standalone analysis tools, but they are mostly coupled to other systems such as SEM, TEM, SIMS, AES and many more. The most common coupled system consists of an electron and an ion tube and is used in a SEM [22].

Transmission Electron Microscopy (TEM)

Compared to the SEM, the transmission electron microscope (TEM) creates images in transmission. Those images are always a projection and the TEM-information is a mean signal over the whole thickness of the sample. An unfortunate side effect is the damage of sample through ionizing radiation (especially for polymers, biological samples, various ceramics ...). A good introduction to TEM is given by Williams and Carter [23].

The biggest difference between SEM and TEM is in the thickness of the sample itself. For TEM measurements, it has to be as thin as possible, while thin means "electron transparent" in this case. The maximum thickness for electrons with an energy of about 200 keV is about serveral 100 nm. The sample preparation is the most challenging part of a TEM measurement. There, FIB is also a frequently used technique for creating thin samples. During the investigation, the structure of the sample as well as its chemical composition can be changed. A standard TEM consists of an electron gun, condenser lenses to bundle the beam, the sample, an objective lens after the sample and a projection system with screen. Compared to the SEM, the interpretation of TEM images is not that straight forward due to several considerable effects and contrasts, which are not explained in this thesis.

A TEM modification is the energy-filtering TEM (EFTEM). The additional energy filter enables the possibility to represent the elementary composition of samples. The big advantages of the EFTEM are short measurement times (1 to 5 minutes per element), a good

spatial resolution and the possibility of a quantification.

The superior resolution (nm range) in combination with an EDX detector makes the TEM a proper analytic method for the investigation of interfaces,e.g., reaction processes.

Atomic Force Microscopy (AFM)

The atomic force microscopy (AFM) is a method where no interaction between primary particles and a specimen with a resulting generation of secondary paricles takes place. The AFM is a combination of the principles of the Scanning Tunneling Microscope (STM) and a stylus profilometer. In this setup, the STM is able to measure the motion of a cantilever beam with a small mass, so that the measured distances can be as small as 10^{-5} nm. The forces to reach such a distance change are at about 10^{-18} N, that is the force between single atoms [24]. This sensitivity is the main advantage of this method. The principle of a measurement according to Ref. [24] can be seen in Fig. 3.3.

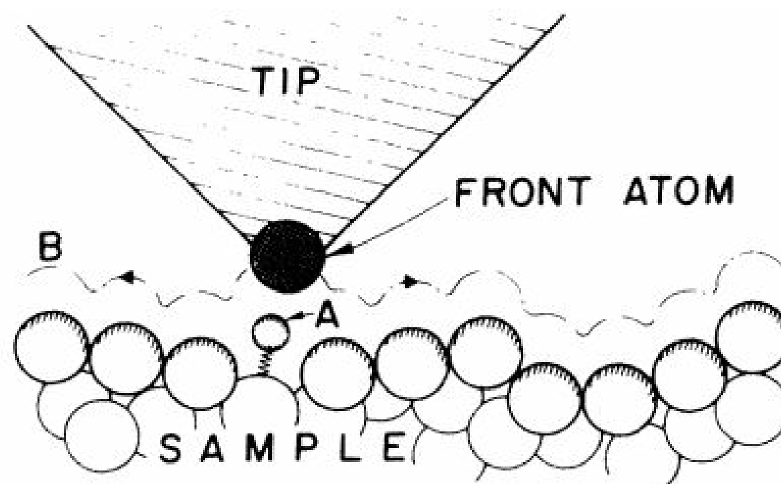

Fig. 3.2: The measurement principle of a AFM: The tip fixed at the cantilever beam follows the trace B along the surface. Small changes are detected and measured. [24]

The cantilever with the attached stylus is attached to a small piezoelectric element and is locked between the AFM sample and the tip. During the measurement, the force on a sharp tip is recorded. This force is tried to keep small and at a constant level with a feedback mechanism to detect changes on the surface [24]. With this principle, surface images with a lateral and height resolution in the nm range can be recorded.

3.3 Mechanical Characterization

3.3.1 nanoIndentation

NanoIndentation is a well-established technique for mechanical investigations of specimens. The idea is to record the the depth of penetration of an indenter into the specimen along with the measured applied load to determine the area of contact. In this thesis, a Berkovich indenter was used [25]. This indenter form is quite common because its mechanical properties are known, it cannot be damaged easily, is relatively easy to manufacture and its relatively large included angle minimizes the influence of friction [26].

During the measurement, the indenter is pressed into the sample. Force dependent, there are 3 different phases during the recording: Elastic contact, transition zone and fully developed plastic zone [25].

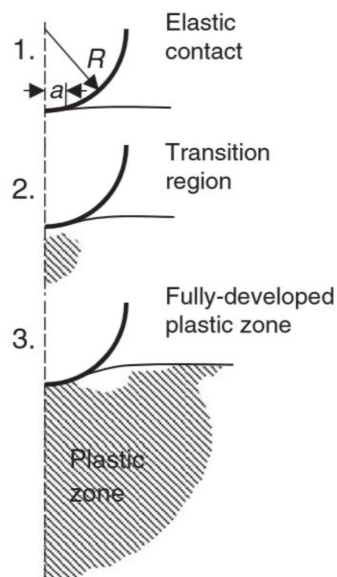

Fig. 3.3: Schematic description of the 3 different force-dependent zones during a nanoIndentation measurement [25].

The result is an experimental force-displacement curve. From that, several different quantities can be derived: elastic modulus, strain-hardening index, fracture toughness, yield stress or residual stress are just some examples [25]

It has to be taken into account that the measurement always influences an interaction volume. If a stack of different materials is measured, the result is related to the whole stack, not only a single layer. Another point is, that the penetration depth is not equal to the measured

depth. During the measurement process, the tip pressing onto the surface is penetrating deeper layers as well. For the calculation of the hardness, the measured volume is 3 times the penetration depth, for Young's modulus 10 times. This has to be taken into account when interpreting nanoIndentation results [25, 26].

4 Computational Methods and their Implementation

Many physical processes and problems are described by differential equations and their analytical solutions are often able to describe the ideal behaviour. When additional influences, that are common in real engineering problems, appear, exact solutions are sometimes not possible anymore. Then numerical methods and approximations are necessary. Over the last years, the development of computers with high computational power and specialized software made it possible to simulate the physics of many problems with computational methods to good accuracy. Two of those methods, the Finite Difference Method (FDM) and the Finite Element Method (FEM), are described in more detail in the following.

4.1 Finite Difference Method (FDM)

In this thesis, the diffusion equation is highly relevant. The most common method to approximate this 2nd order differential equation is the Finite Difference Method (FDM) via Crank-Nicholson formula, of which the according derivation will be described next [27].

The introduction of dimensionless quantities in numerical methods is in principle not necassary, but delivers some mathematical advantages in this case. For the diffusion equation, the following dimensionless quantities are defined:

$$X = \frac{x}{l} \tag{4.1}$$

$$T = \frac{Dt}{l^2} \tag{4.2}$$

$$c = \frac{C}{C_0} \tag{4.3}$$

where the unit of the thickness l of the plate is in m and of the diffusion coefficient D in $\frac{m^2}{s}$. The quantity C describes the concentration and C_0 the starting concentration, x and t are variables for penetration depth and time, respectively. This substitution leads to:

$$\frac{\partial C}{\partial x} = \frac{\partial C}{\partial X}\frac{dX}{dx} = \frac{\partial C}{\partial X}\frac{1}{l} \quad \rightarrow \quad \frac{\partial^2 C}{\partial x^2} = \frac{\partial^2 C}{\partial x^2}\frac{1}{l^2} \tag{4.4}$$

$$\frac{\delta C}{\delta t} = \frac{\delta C}{\delta T}\frac{\delta T}{\delta t} = \frac{\delta C}{\delta T}\frac{D}{l^2} \tag{4.5}$$

For the diffusion equation, this yields:

$$\frac{\delta C}{\delta t} = D\frac{\delta^2 C}{\delta x^2} \quad \rightarrow \quad \frac{\delta c}{\delta T} = \frac{\delta^2 c}{\delta X^2} \tag{4.6}$$

Here it has to be noted, that the diffusion coefficient D is now in the transformed variable T.

The simplest problem to investigate is the flow through a flat wall (Fig. 4.1).

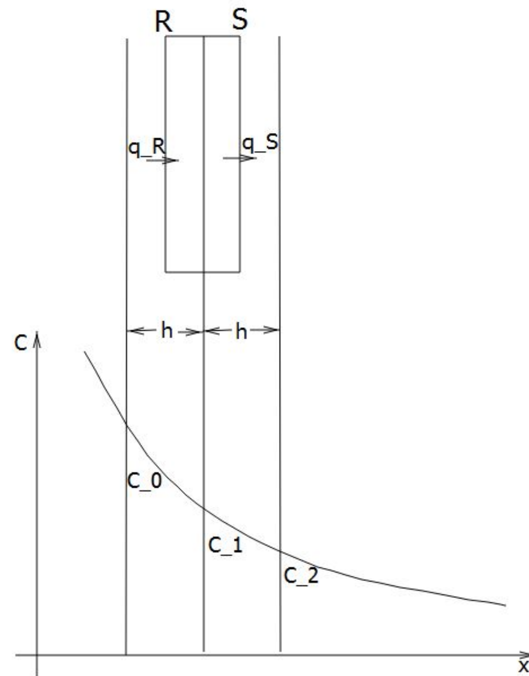

Fig. 4.1: Schematic representation of an approximation via finite differences [27]
The figure shows an equidistant division in subintervals of length h. The corresponding concentration values can be read from the curve.

If the surface is divided into 2 parts, this leads to:

$$q_R = -D\tau\frac{(C_1 - C_0)}{h} \tag{4.7}$$

describing flow into the surface and

$$q_S = -D\tau\frac{(C_2 - C_1)}{h} \tag{4.8}$$

describing flow out of the surface. Here, h marks the intervall length and τ is a short time duration. The net flow results from the difference of both parts:

$$q_R - q_S = -\frac{D\tau}{h}(C_1 - C_0 - C_2 + C_1) = \frac{D\tau}{h}(C_0 - 2C_1 + C_2) \tag{4.9}$$

This is a discretization in space.
If C_1 is used to calculate an average concentration in a region, the concentration difference can be written as:

$$(C_1' - C_1) \cdot h = \frac{D\tau}{h}(C_0 - 2C_1 + C_2)$$

$$C_1' - C_1 = \frac{D\tau}{h^2}(C_0 - 2C_1 + C_2) \tag{4.10}$$

where C_1' marks the concentration at the end of the interval τ. The transition from C_1 to C_1' can be interpreted as a discretization in time. For $\frac{D\tau}{h^2} = \frac{1}{2}$, the result is the arithmetic mean of the concentrations C_0 and C_2:

$$C_1' = \frac{1}{2}(C_0 + C_2) \tag{4.11}$$

If the concentration at a point at time $t + \tau$ is known at the edge of an interval, the concentration in the whole space can be determined iteratively in time steps τ.

If this is applied generally to N points, this is known as the explicit method or finite difference solution. An area X is divided in equidistant intervals δX and the time T in intervals of δT. The coordinates of a random point (X,T) can be written as $(i\delta X;j\delta T)$ for i and j to be real integers. Here, i is the integer for the space-coordinate and j for the time-coordinate. The concentration c at a point $(i\delta X,j\delta T)$ is denoted as $c_{i,j}$. The development in a Taylor expansion in T direction at constant X leads to:

$$c_{i,j+1} = c_{i,j} + \delta T \left(\frac{\partial c}{\partial T}\right)_{i,j} + \frac{1}{2}(\delta T)^2 \cdot \left(\frac{\partial^2 c}{\partial T^2}\right)_{i,j} + ... \tag{4.12}$$

The first derivative in T is:

$$\left(\frac{\partial c}{\partial T}\right)_{i,j} = \frac{c_{i,j+1} - c_{i,j}}{\delta T} + O(\delta T) \tag{4.13}$$

The application of the Taylor expansion in X direction with constant T is:

$$c_{i+1,j} = c_{i,j} + \delta X \left(\frac{\partial c}{\partial X}\right)_{i,j} + \frac{1}{2}(\delta X)^2 \cdot \left(\frac{\partial^2 c}{\partial X^2}\right)_{i,j} + ... \tag{4.14}$$

$$c_{i-1,j} = c_{i,j} - \delta X \left(\frac{\partial c}{\partial X}\right)_{i,j} + \frac{1}{2}(\delta X)^2 \cdot \left(\frac{\partial^2 c}{\partial X^2}\right)_{i,j} - ... \tag{4.15}$$

The addition of (4.14) and (4.15) leads to the second derivative in X:

$$\left(\frac{\partial^2 c}{\partial X^2}\right)_{i,j} = \frac{c_{i+1,j} - 2c_{i,j} + c_{i-1,j}}{(\delta X)^2} + O(\delta X)^2 \tag{4.16}$$

Inserting (4.13) and (4.16) in (4.6) results to:

$$c_{i,j+1} = c_{i,j} + r(c_{i-1,j} - 2c_{i,j} + c_{i+1,j}) \tag{4.17}$$

Inserting $r = \frac{1}{2}$ in Eq. 4.17 delivers a formula analogous to the arithmetic mean. A formula like (4.17), where an unknown is described by known values, is called explicit finite difference formula.

A in well-established numerical method was published by Crank and Nicolson [27]. The "Crank-Nicolson Implicit Method" approximates the second derivative of the concentration in X ($\frac{\partial^2 c}{\partial X^2}$) via FDM. This leads to the following approximation of Eq. 4.6:

$$\frac{c_{i,j+1} - c_{i,j}}{\delta T} = \frac{1}{2} \cdot \left(\frac{c_{i+1,j} - 2c_{i,j} + c_{i-1,j}}{(\delta X)^2} + \frac{c_{i+1,j+1} - 2c_{i,j+1} + c_{i-1,j+1}}{(\delta T)^2}\right) \tag{4.18}$$

For $\frac{\delta T}{(\delta X)^2} = r$:

$$-rc_{i-1,j+1} + (2 + 2r)c_{i,j+1} - rc_{i+1,j+1} = rc_{i-1,j} + (2 + 2r)c_{i,j} + rc_{i+1,j} \tag{4.19}$$

In Eq. 4.19 it can be seen, that the left side only contains terms with the unknown $(j+1)$ time step and the right side only variables with the known j time step. For in points within the interval, this leads to N equations for N unknown variables in every time step. For the boundary values $i = 0$ and $i = N+1$, those equations can be solved simultaneously known as an implicit method. This Crank-Nicolson formula in combination with a least squares approximation (e.g. Levenberg-Marguardt algorithm [28, 29]) can be used as a fit for diffusion depth profiles.

4.2 Finite Element Method (FEM)

4.2.1 Basics of the Finite Element Method

The Finite Element Method (FEM) has become one of the most frequently used solution methods for many different kinds of differential equations. The big advantage is its generality enabling FEM to solve a wide range of equations from many different parts of science: mechanics, thermo-dynamics, fluid-dynamics, diffusion and many more. A second advantage of this method is the flexibility in formulation. Almost any parameter regarding discretization and approximation can be controlled allowing to adapt many simulations to the available hardware. The theory of FEM in detail is quite complicated and only the basic concepts will be discussed in this thesis. For a more detailed discussion see ,e.g., the FEniCs Book [30], Larson and Bengzon [31], Gockenbach [32] or the master's thesis by Nils Möse [33].

In this thesis, FEM will be explained using an example described in Ref. [30]. Equivalent to the "Hello World!" program for learning programming, the Poisson equation is the basic problem for learning FEM. Before going deeper into the mathematical solution, a few considerations about the prerequisites of the problem should be made. First, deciding whether it is a 2-D or a 3-D problem and what quantity actually should be calculated.

Generation of the Geometric Model

At first, a proper model has to be created. Commercial tools like ANSYS or COMSOL and also the "pdetool" toolbox of MATLAB already have an editor for creating models. For using the open source software FEniCS, external software like "Gmsh" is highly recommended. Drawing a model is straight forward and has not to be discussed in detail. Although, this part of a FEM simulation is often the most time-consuming process and has to be taken with high care.

Meshing

After this step, the mesh has to be created. A mesh is a fine web of finite elements crossing each other. The crossing points are the so-called nodes. Nodes are the points, where solutions are actually calculated and interpolated for the whole function space. There are many types of finite elements varying in shape and behaviour that can be used for simulation, such as Lagrange, Morley, Arnold-Winther, Raviart-Thomas and many more. For the example

of the Poisson equation and for solving the diffusion equation in this thesis, the Lagrange (Continuous Galerkin - CG) elements were used, which are intervals in 1-D, triangles in 2-D and tetrahedrons in 3-D. The meshing step is the discretization of the model drawn with those finite elements. The smaller the elements and the finer the resulting grid, the more computationally expensive the simulation will be.

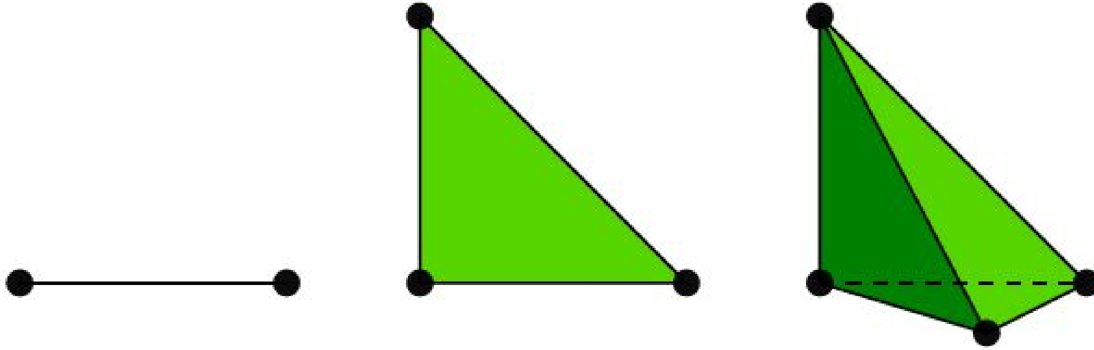

Fig. 4.2: The finite Lagrange element for 1, 2 and 3 dimensions [30]

Mathematical Description of the Physical Problem

After those preparations, the mathematical problem itself can be formulated. As already mentioned, the Poisson problem is the most basic example for FEM:

$$-\nabla^2 u(x) = f(x), \quad x \; in \; \Omega, \tag{4.20}$$

$$u(x) = u_D(x), \quad x \; in \; \partial\Omega \tag{4.21}$$

$u = u(x)$ is the unknown function, $f = f(x)$ is a prescribed function, ∇^2 is the Laplace operator containing the sum of derivatives over the 3 dimensions in space, Ω is the spatial domain and $\partial\Omega$ is the boundary of Ω. The Poisson problem therefore is an example for a boundary-value problem. For the usage of FEniCS by integration of thee respective packages into the Python source code, the following steps are necessary:

- Identification of the computational domain (Ω, the PDE, its boundary conditions and source terms (f)
- Reformulation of the PDE as a finite element variational problem

- Writing of a Python program which defines the computational domain, the variational problem, the boundary conditions and the sources terms
- Call of FEniCS to solve the boundary value problem (and optionally extend the program to visualize the results or perform other types of post-processing)

The only tricky part of setting up the calculation is the variational formulation of the problem. In fact, one can use FEniCS without any knowledge of FEM if one is able to construct the variational form. The idea is to get rid of second derivatives by multiplying the whole equation with a function and performing an integration by parts afterwards. This function v will be called test function and the function u to be approximated is the trial function:

$$-\int_{\Omega}(\nabla^2 u)v dx = \int_{\Omega} f v dx \tag{4.22}$$

The integration of the left-hand side yields:

$$-\int_{\Omega}(\nabla^2 u)v dx = \int_{\Omega} \nabla u \cdot \nabla v dx - \int_{\partial\Omega} \frac{\partial u}{\partial n} v ds \tag{4.23}$$

The trick is, that the test function v is required to vanish at parts of the boundary where the solution u is known. In this problem, this leads to:

$$\int_{\Omega} \nabla u \cdot \nabla v dx = \int_{\Omega} f v dx \tag{4.24}$$

resulting in the following canonical notation:

$$a(u,v) = L(v) \tag{4.25}$$

for:

$$a(u,v) = \int_{\Omega} \nabla u \cdot \nabla v dx \tag{4.26}$$

and:

$$L(v) = \int_{\Omega} f v dx \tag{4.27}$$

where $a(u,v)$ is known as the mathematical bilinear form, and $L(v)$ as the linear form. Solving Eq. 4.25 in Python-FEniCS it the solution of the differential equation, what is the final step.

4.2.2 Application of the FEniCS Package for Python and Additional Software

One of the big advantages of commercial FEM distributions such as COMSOL and ANSYS is the completeness after installation. Model building, calculation and post-processing can all be done with one tool that already includes all the functions. FEniCS can be taken into account as an alternative. Beside the big advantage that it is an open source code that can be used by everyone, this package leaves a lot of free space to adjust several parameters of FEM simulations: starting from model and equation over all types of different solver parameters to the solution itself. Installing FEniCS is analogous to the installation of any other Python package.

Though pre- and post-processing is possible with the FEniCS package itself, additional software may be helpful in several situations. One of them is Gmsh, a freeware mesh generator. As a really intuitive tool, it can be used for creating models and proper meshes. The workflow is straight forward: First, points in a model are specified. The points can be connected to lines and lines to surfaces. The mesh size can be specified at each point, so that areas with finer and coarser grid size can be defined. A further advantage can be found in the definition of physical groups, e.g., surfaces can be combined to physical groups with identical properties, i.e., density, thermal or diffusion coefficient, electrical conductivity and many more. Those groups can be used to specify properties of the equations in a specific area. In the simulation of this thesis, physical groups were used to distinguish between bulk and grain boundary diffusion zones.

For post-processing tasks, the free software package ParaView is recommended. Each solution step from the FEniCS simulation can be saved in .pvd files. Those can be opened in ParaView to visualize the solutions afterwards, edit legends and ranges, representation color and more. Furthermore, single images can be combined to movies. There are many more functions this programme can be used for, again in an intuitive and straight forward way.

4.2.3 The Diffusion Model - Simulation via FEM

There are many ways to simulate diffusion processes. Molecular dynamics [34] as well as FEM are the most common approaches so far. Diffusion as already mentioned in chapter 2 can be described as a transport equation. In this case, the diffusion equation known as Fick's 2nd law has to be used. This equation is analogous to the heat equation, an often used equation in FEM simulations and can be adapted easily. As mentioned in section 4.2.1,

the weak form of this equation has to be derived. This derivation will be done in this chapter according to the well-described explanation in the FEniCs tutorial by Langtangen and Logg [5].

At first, the whole problem will be stated:

$$\frac{\partial u}{\partial t} = \nabla^2 u + f \quad in\ \Omega\ \times\ (0,T], \tag{4.28}$$

$$u = u_D \quad on\ \partial\Omega\ \times\ (0,T], \tag{4.29}$$

$$u = u_0 \quad at\ t\ =\ 0 \tag{4.30}$$

Here, u is the concentration. This means, that the equation is valid in a space Ω with a known boundary condition u_D and an initial value named u_0. The function f are source terms, where other effects beside diffusion, e.g., reaction can be considered.

The difficulty in treating this equation can be found in its time-dependence. One approach is a straight forward one, where the time derivative is approximated via the finite difference method. This yields to a sequence of stationary equations, which can be transferred into a set of variational problems:

$$(\frac{\partial u}{\partial t})^{n+1} = \nabla^2 u^{n+1} + f^{n+1} \tag{4.31}$$

The time-derivative can now be approximated by a diffence quotient. In terms of simplicity and stability, a backward difference is one possibility for an approximation:

$$(\frac{\partial u}{\partial t})^{n+1} \sim \frac{u^{n+1} - u^n}{\Delta t} \tag{4.32}$$

Combining those two equations yields to:

$$\frac{u^{n+1} - u^n}{\Delta t} = \nabla^2 u^{n+1} + f^{n+1} \tag{4.33}$$

known as a so-called backward or implicit Euler discretization. This is now the time-discrete form of the heat and/or diffusion equation.

Now we can reorder the equation in two different ways: In a first way so that the left-hand side only contains u^{n+1} or unknown values and the right side consists of u^n terms, which are already known from the previous step. By using the initial condition $u_0 = u^0$, one

can write the equation as:

$$u^{n+1} - \Delta t \nabla^2 u^{n+1} = u^n + \Delta t f^{n+1}, \quad n = 0, 1, 2... \tag{4.34}$$

A second possible formulation is created by collecting all terms on one side:

$$u^{n+1} - \Delta t \nabla^2 u^{n+1} - u^n - \Delta t f^{n+1} = 0, \quad n = 0, 1, 2... \tag{4.35}$$

In this way we have successfully treated the time dependence. But how to proceed with the second derivative in space ∇^2? Here, the weak form is needed. To achieve that, Eq. 4.34 has to be multiplied with a test function v. To remove the second derivative, an integration by parts has to be performed, what leads to two possible formulations. The standard notation with:

$$a(u, v) = L_{n+1}(v) \tag{4.36}$$

with:

$$a(u, v) = \int_\Omega (uv + \Delta t \nabla u \nabla v) dx \tag{4.37}$$

$$L_{n+1}(v) = \int_\Omega (u^n + \Delta t f^{n+1}) v dx \tag{4.38}$$

or the abstract formulation with:

$$F_{n+1}(u, v) = 0 \tag{4.39}$$

with:

$$F_{n+1}(u, v) = \int_\Omega (uv + \Delta t \nabla u \nabla v - (u^n v + \Delta t f^{n+1} v)) dx \tag{4.40}$$

Now, we can solve the problem for each time step. Finally, only the initial condition has to be turned into a variational problem as well:

$$a_0(u, v) = L_0(v) \tag{4.41}$$

with:

$$a_0(u, v) = \int_\Omega uv dx \tag{4.42}$$

$$L_0(v) = \int_\Omega u_0 v dx \tag{4.43}$$

Under these assumptions, the equation can be implemented in FEniCs and solved iteratively.

4.2.4 The Diffusion-Reaction Model - Simulation via FEM

Solving the diffusion or heat equation is one of the basic examples for FEM simulations. A more challenging (and computationally much more expensive) simulation arises, when one additionally tries to consider reaction processes, e.g., phase formation. For this effect, the source term in Eq. 4.28 has to be considered. There are many different approaches like the Fisher equation for chemical reactions or the Zeldovich equation, which are all semi-empirical ones. One approach used in biology, that considers even 2 different partners or elements (e.g. Al and Cu), is the Gray-Scott-Model [35]:

$$\frac{\partial u}{\partial t} = D_u \nabla^2 u - uv^2 + f(1-u)$$

$$\frac{\partial v}{\partial t} = D_v \nabla^2 v + uv^2 - (f+k)v \tag{4.44}$$

One can recognize the first part of both equations as the standard diffusion equation. Here, u and v name the concentrations of the reaction-diffusion partners. The rest can be summed up as source terms with the parameters f (feed rate) and k (kill rate). Those are actually reaction parameters. Physically the feed rate is introduced to specify, how fast atoms are consumed by a phase. Numerically this term has to be scaled that the amount of atom A does not exceed the maximum concentration 1. The kill term is the counterpart to the feed rate and removes atoms of type B as soon as a phase is forming. Numerically, this term ensures that the concentration of atoms B in the system never drops below 0. In this work, those parameters were chosen to find a good convergence and a phase formation duration comparable to reality.

Similar as for the diffusion equation, the Gray-Scott equations have to be transformed into their weak forms as well. This can be done separated. The approximation of the time-derivative is analogous to the diffusion equation and will not be repeated at that point.

After this, the test function (now p and q) have to be multiplied and an integration by parts has to be done. For solver reasons, the abstract formulation will be used here.

$$F^1_{n+1}(u,v,p) = \int_\Omega (up - u_n p + D_u \nabla u \nabla p \Delta t + uv^2 p \Delta t - f(1-u)p\Delta t)dx \tag{4.45}$$

$$F^2_{n+1}(u,v,q) = \int_\Omega (vq - v_n q + D_v \nabla v \nabla q \Delta t - uv^2 q \Delta t + (f+k)vq\Delta t)dx \tag{4.46}$$

Under the assumption that:

$$F^1_{n+1} + F^2_{n+1} = 0 \tag{4.47}$$

and the analogous transformation for the initial conditions into variational form, the Gray-Scott equations can be solved by the software package FEniCs.

5 Experimental Results

5.1 Sample Description and Synthesis

To investigate diffusion-reaction in the Al-Cu system based on the information from the previous chapters, different samples where produced using the sputter deposition. Single-wafer sputter chambers attached to a main frame enabled the possibility of in-situ deposition of all layers in one process. Thus, the sample never left the vacuum during the whole production process. So, Al-Cu-TiW, Ni-Cu-TiW or Ag-Cu-TiW layer stacks are possible to manufacture in one PVD tool. As mentioned in section 2.4, the grain size and the structure of the deposited material can be tuned by varying the pressure during sputtering (in this case Ar sputter gas pressure) as well as the temperature on the substrate. According to Thornton's diagram (Fig. 2.6), a lower temperature should lead to fine grains, the higher the temperature, the larger and more columnar the grains should become. This can be used to influence the diffusion-reaction behaviour. The idea behind this is the following: diffusion is faster in grain boundaries than in the bulk, so smaller grains exhibit more grain boundaries per area and therefore faster diffusion. Furthermore, the mechanical behaviour of the material should be influenceable as well. The schematic overview of the material stacks produced are shown in Fig. 5.1.

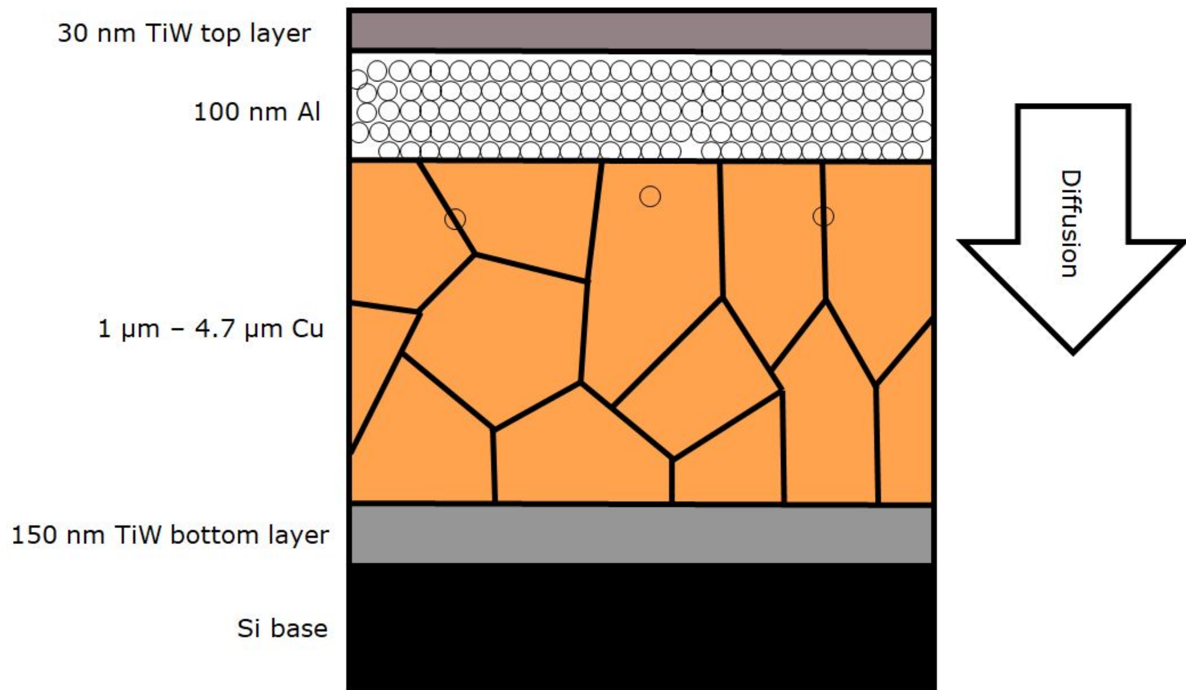

Fig. 5.1: Schematic overview of the samples produced for the investigation of Al-Cu diffusion-reaction processes: During the annealing process, Al atoms are forced to diffuse into the grained Cu layer

Starting with Si at the bottom as base material, at first a 150 nm thick TiW-layer was deposited. This layer is necessary as a diffusion barrier to protect the Si from interacting with the above Cu-layer and to reduce mechanical stress.
The Cu-layer itself varies from 1 to 4.7 μm in thickness. This is a process-related problem. To obtain fine-grained Cu-layers, a low substrate temperature is necessary. To achieve that, the sputter ratio and therefore the sputter power has to be as low as possible. This leads to very long process times, so that 4.7 μm thick samples were not produceable. Additionally, fine-grained Cu-layers apply a lot of mechanical stress on the whole system. This can for instance lead to a peeling-off of the Cu-layer from the sample.
The third layer is the Al-layer, that serves as a Al atom source. Due to the fact, that only a few monolayers of Al would be sufficient to saturate the grain boundaries, this layer can be seen as an infinite source for diffusing Al atoms.
Finally, there is another 30 nm thick TiW-layer on top. This final top layer of the stack is to protect the Al-Cu system from environmental influences.

Based on the information from Thornton's diagram (Fig. 2.6), different samples were pro-

duced of which the parameters are summarized in Tab. 5.1):

Tab. 5.1: Sample production conditions / parameters: the substrate temperature given is the temperature of the wafer during the deposition process. Argon is the inert gas and the Ar-pressure is a quantity to describe the amount of gas in the chamber. The Al- and Cu-thickness give the amount of deposited material for each sample produced.

Substrate Temp. [°C]	**Ar-Pressure [mTorr]**	**Al-Thickness [nm]**	**Cu-Thickness [nm]**
60	10	100	1000
60	3	100	1000
200	3	100	1000
300	3	100	1000
200	3	100	2000
300	3	100	2000
290	3	100	4700
410	3	100	4700

The substrate temperature below 250 °C were measured with temperature stripes. The temperature values above 250 °C are estimations. The Cu-layers deposited at a substrate temperature below 100 °C belong to Zone 1 in Thornton's diagram (Fig. 2.6). There, grains are expected to be small and almost amorphous. This would lead to a higher density of grain boundaries per area followed by an enhanced diffusion. A substrate temperature of between 200 °C and 300 °C provides the conditions for the transition zone T. There, grains are growing and orientating themselves columnar. Larger grains with columnar orientation are ideal for diffusion experiments. The exact theoretic approaches explained in section 2.3 are valid for grain boundaries at an angle of 90° with respect to the substrate surface.

For that reason, diffusion-reaction analysis and analysis for the Arrhenius law were performed with the samples with a Cu-layer thickness of 4.7 μm at a substrate temperature of 410 °C.

5.2 Initial Characterization

For an initial characterization, the layers produced were investigated using imaging methods. To get a top view on the Cu structure, samples without TiW top layer and Al layer were produced and imaged using AFM (Fig. 5.2). For investigation of the cross section, combined FIB-SEM-images were created. In the following, those images are named FIB-

images. Therefore, a cut through the sample using focussed ion beam technique was used. FIB-SEM-images of the investigated samples can be found in Fig.5.3.

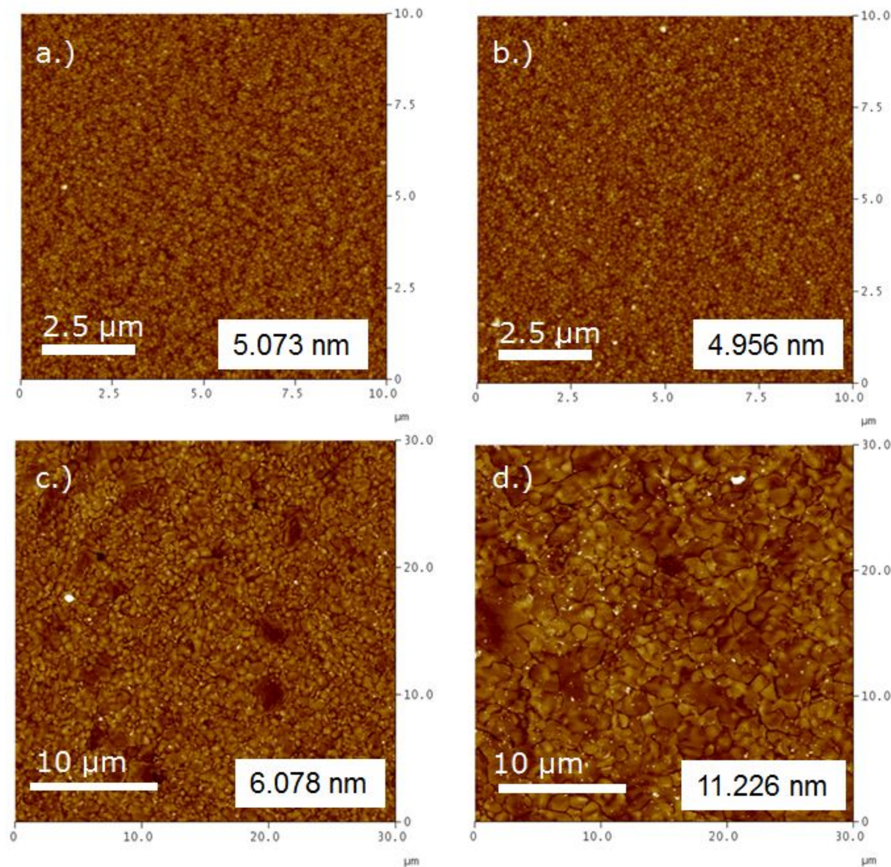

Fig. 5.2: Micrographs of AFM analysis for Cu grain size and structure investigation in dependency of process parameters substrate temperature and Ar-gas pressure: a.) $\sim$ 60 °C and 10 mTorr; b.) $\sim$ 60 °C and 3 mTorr; c.) $\sim$ 320 °C and 3 mTorr; d.) $\sim$ 410 °C and 3 mTorr

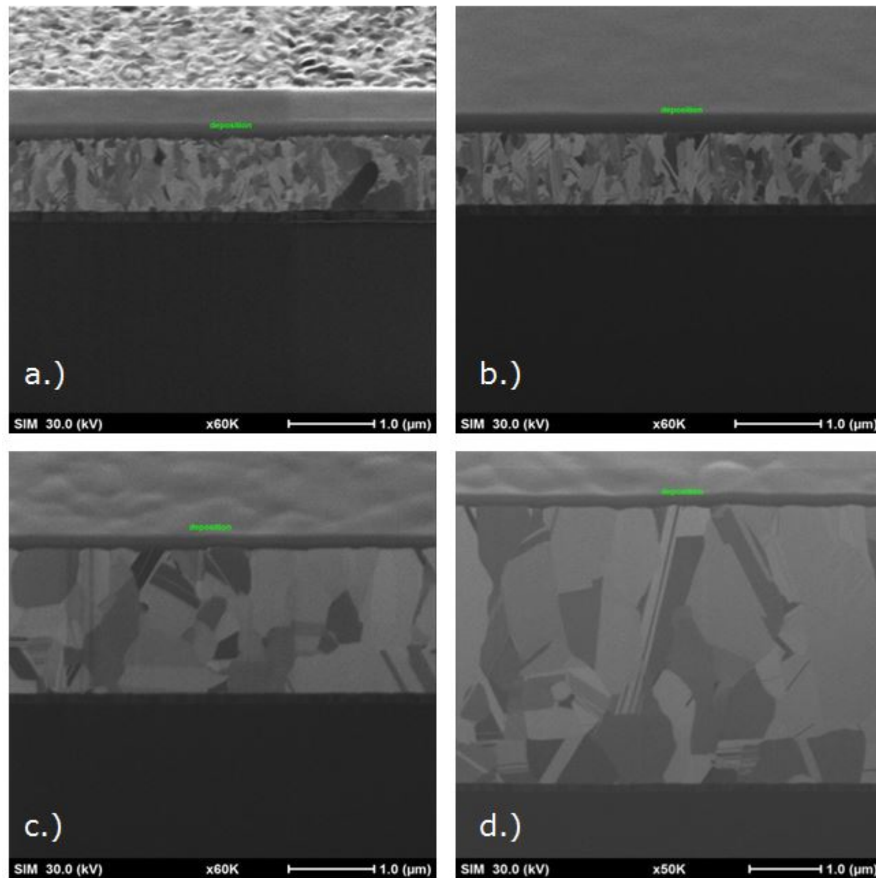

Fig. 5.3: Micrographs of FIB analysis for Cu grain size and structure investigation in dependency of process parameters substrate temperature and Ar-gas pressure: a.) ∼ 60 °C and 10 mTorr; b.) ∼ 60 °C and 3 mTorr; c.) ∼ 320 °C and 3 mTorr; d.) ∼ 410 °C and 3 mTorr

As one can see, the images a.) and b.) in Fig. 5.2 appear almost identical. The grain size as well as the roughness are quite equal implying that varying Ar-gas pressure between 3 mTorr and 10 mTorr during the process does not influence the grain properties. In comparison, a difference in temperature has a higher impact to grain size and structure.

The findings from the AFM images are confirmed by FIB-Cuts. The pictures a.) and b.) have a very small, almost amorphous grain structure. The higher the temperature, the larger the grains become. Furthermore, the structure gets more and more columnar making the layer suitable for diffusion investigations.

Another advantage of this layer is the thickness, which enables larger diffusion lengths. Those are important conditions because diffusion laws are only valid when no saturation is reached. Another fact that has to be taken into account is the different layer thickness. This

is as already mentioned a process related problem with increasing Cu stress with lower grain size. Higher layer thickness also leads to a further growth of grains. Therefore Fig. 5.3 a.) and Fig. 5.3 d.) are not entirely comparable.

5.3 Diffusion-Reaction Investigation in Al-Cu system

To take a closer look at the diffusion-reaction processes, sample annealing was necessary. Due to the fact, that sample surface temperature ranges from 100 °C to 300 °C are interesting for semiconductor industry, primarily B- and C-regime diffusion were investigated. To identify the diffusion regimes, the classification according to Harrison [12] was applied. As mentioned in chapter 2, conditions (Eqs. 2.19 and 2.25) have to be satisfied for B- ($s\delta << \sqrt{Dt} << d$) or C-regime diffusion ($\sqrt{Dt} << s\delta$).

There, s marks the segregation factor, δ the grain boundary width, D the diffusion coefficient, t the diffusion time and d the average grain size (or distance between two neighbouring grain boundaries). With an assumed diffusion coefficient of 10^{-15} cm^2/s, an average grain width of 2 μm, the grain boundary width with the literature value of 0.5 nm, the segregation factor of approximately 50 and an annealing time between 1 (Eq. 5.1) and 400 h (Eq. 5.2), the calculation leads to:

$$2.5 \cdot 10^{-15} \text{ cm} << 2 \cdot 10^{-6} \text{ cm} << 2 \cdot 10^{-4} \text{ cm} \tag{5.1}$$

$$2.5 \cdot 10^{-15} \text{ cm} << 3 \cdot 10^{-5} \text{ cm} << 2 \cdot 10^{-4} \text{ cm} \tag{5.2}$$

Both of these conditions satisfy B-regime diffusion, but one has to take into account, that diffusion coefficient and segregation factor are not known precisely at that point and here are just reasonable guesses. Especially the diffusion coefficient can be even magnitudes lower, because it refers to bulk diffusion, which is actually not measureable.

Under these assumptions, the annealing conditions were developed (Fig. 5.4).

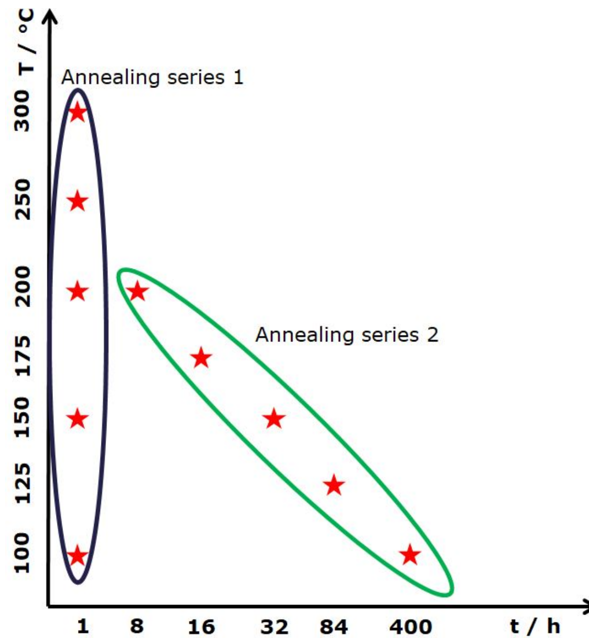

Fig. 5.4: Annealing conditions for investigation of reaction-diffusion processes in Al-Cu system according to Harrison's type-B diffusion regime: the annealing temperature T is plotted against the annealing time t. Annealing series 1 were performed with a variation in temperature at constant time (1 h). Annealing series 2 vary in time and temperature.

The annealing was performed in an N_2-purged lab furnace to secure that no external influences disturb the diffusion-reaction processes. As seen in Fig. 5.4, 10 different annealing processes were performed. The first series for 1 h at 100 to 300 °C was performed to get an overview over the temperature range to answer the question: how much Al can be detected by ToF-SIMS depth profiling? When do phase formation processes start? It could be shown, that reaction processes occur from approximately 175 °C upwards. Therefore, a second series from 100 °C to 200 °C for longer annealing times was performed to investigate diffusion quantitatively. The samples have been analysed using ToF-SIMS depth profiling afterwards. The results of those measurements are given in section 5.4.

5.4 ToF-SIMS Depth Profiling

The diffusion of Al in Cu at different temperatures and for different annealing times were investigated using ToF-SIMS depth profiling as discussed in section 3.2.1. The results are presented in the following.

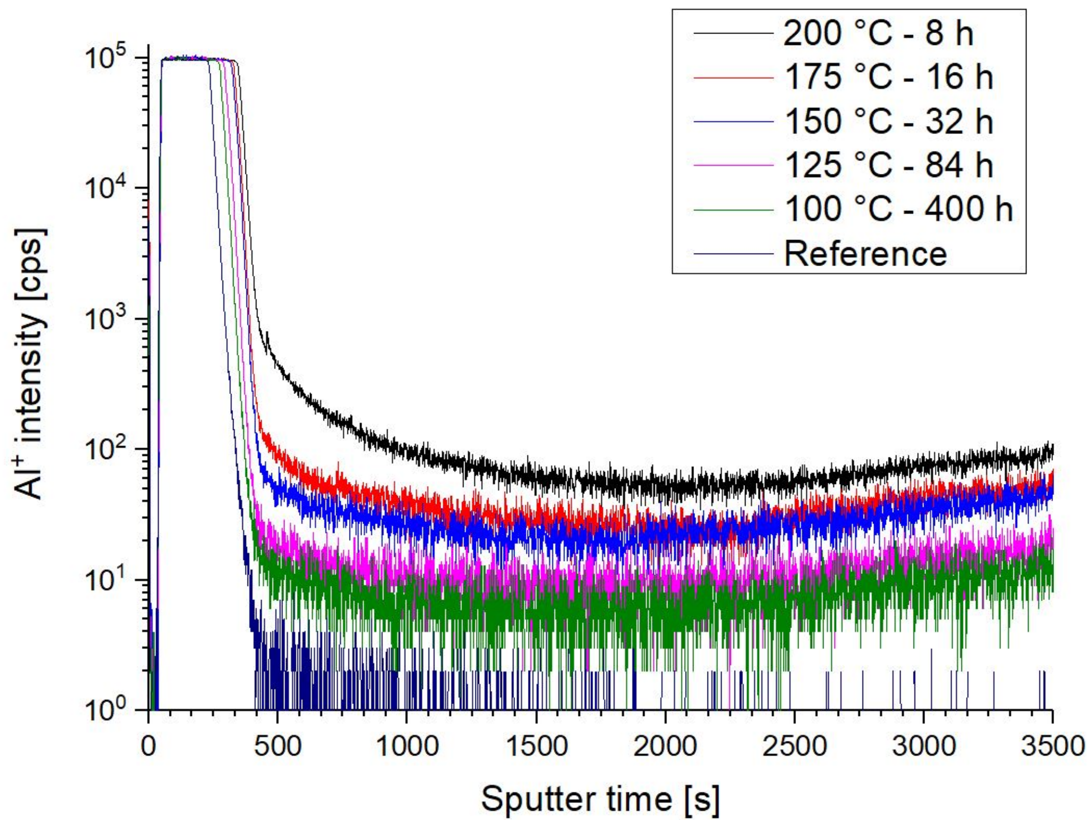

Fig. 5.5: ToF-SIMS depth profiling of the Al concentration for annealing up to 200 °C. There, the sputter time is plotted versus the logarithm of the Al^+ intensity. The depth is proportional to the sputtering time if a constant ToF-SIMS sputter rate is assumed.

To discuss diffusion processes, the results of annealing series 2 (100 - 200 °C for different durations) are explained here first. The samples with a grain size of 4.7 μm deposited at a substrate temperature of 410 °C were used because of the large grain size and their nearly columnar orientation. The sputter time plotted in the ToF-SIMS graphs is proportional to the depth assuming a constant ToF-SIMS sputter rate. Due to the formation of intermetallic compounds, this assumption is not entirely satisfied. In approximation, the sputter rates vary from 1.4 to 1.8 nm/s depending on the sample.

According to the theory in chapter 2, a depth profile should consist of 3 parts: bulk diffusion at the beginning followed by a transition zone and finally the grain boundary diffusion zone. For the curves up to 175 °C, this assumption seems to be valid. Up to approximately 300 s sputter time, one can see a constant Al^+ intensity value. This happens due to the fact, that the ToF-detector is saturated there. Then, the signal starts to drop rapidly. There, the

end of the Al layer has been reached and therefore, the Al^+ concentration drops. 3 effects are possible to see:

- **Roughness:** During the measurement, two different ion beams are aimed onto the target: one measurement beam and one sputter beam. The sputter beam is creating a crater and due to destruction of the surface, the roughness of the sputtered area increases. This is one effect one can see in a ToF-SIMS depth profile.
- **Bulk Diffusion:** According to Harrison [12] the annealing conditions trigger diffusion processes on the boundary between B- and C-regime. For B-type diffusion, bulk diffusion should appear and can be measured in this area.
- **Interface Effects:** When reaching the boundary between 2 layers, ToF-SIMS measures an enhanced ion concentration. This circumstance is called "interface effect".

These 3 effects explain, why a precise determination of a bulk diffusion coefficient is so hard in this system. There are many influences that superpose the curvature of the bulk diffusion profile making a quantitative analysis of the zone almost impossible.

Then, for increasing sputter times, the profile starts to shift up. That would be the transition zone. Remarkable for this zone is the sample annealed at a substrate temperature of 200 °C , where the signal at approximately 500 s is higher compared to the other curves. This rise can be explained by the start of formation of intermetallic compounds (IMC). After that transition or reaction zone, the signal falls almost linearly up to 2000 s, what can be identified as grain boundary diffusion.

After that point, the signal starts to rise again. This can have 3 different reasons as well:

- **Grain Boundaries are saturated:** When Al atoms are reaching the lower Cu-TiW interface (see Fig. 5.1), they are forced to stop there. When further atoms are diffusing through the Cu layer, this leads to an accumulation and therefore an increase in the signal.
- **Smaller grains:** Taking a closer at look at fig. 5.3, one can recognize that Cu grains closer to the bottom TiW layer are smaller than Cu grains closer to the Al layer. When Cu is deposited, the grains have to arrange themselves at first. That is the reason why the first deposited Cu grains are smaller than the upper ones. Smaller grains lead to more grain boundaries per volume were more Al atoms can be stored. For the case

that the grain boundaries are saturated, this can be a further explanation for the rise of the signal.

- **Interface Effects:** The last option is again a ToF-SIMS interface effect. In that zone, the measurement is close to the Cu-TiW interface what can again lead to an enhanced measured signal.

The second series of depth profile comparisons to be discussed is the one according to the first annealing series (100 - 300 °C for an annealing duration of 1 h). The samples chosen are again with a Cu grain size of 4.7 μm deposited at a substrate temperature of 410 °C. The results can be seen in Fig. 5.6

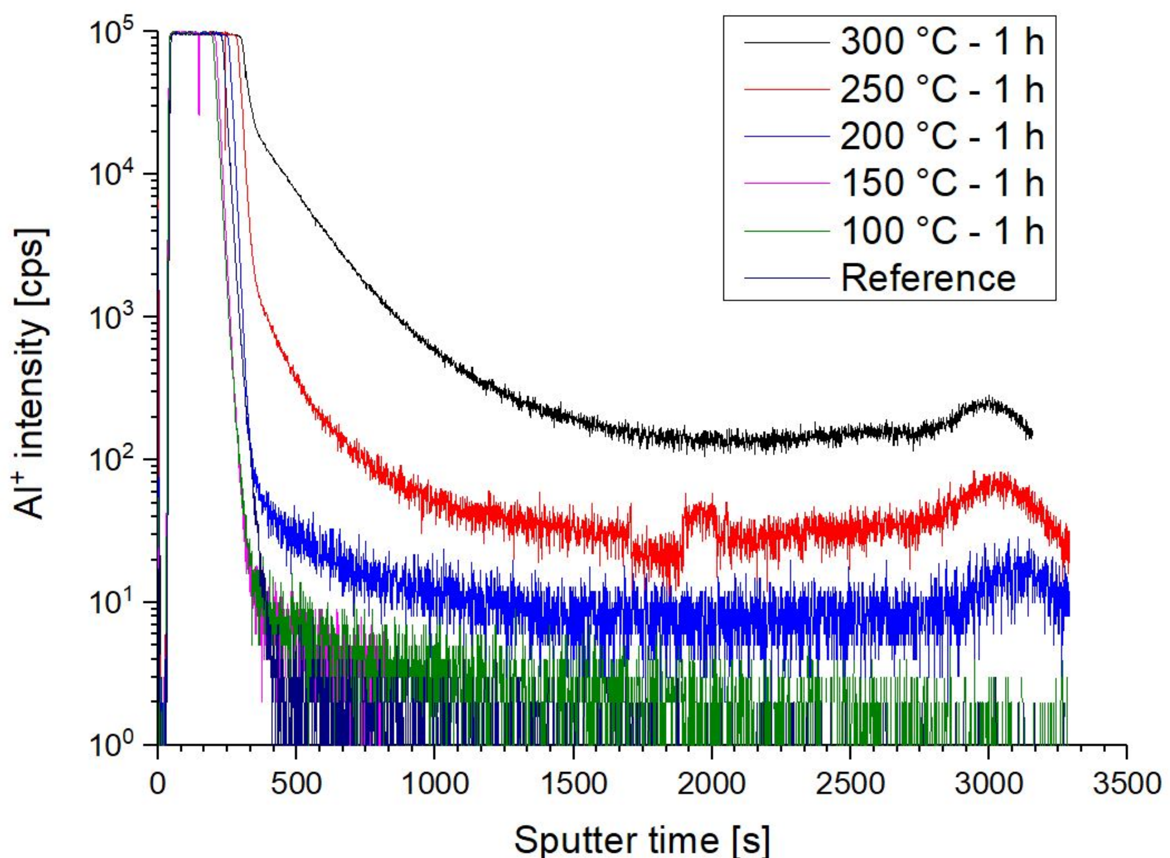

Fig. 5.6: ToF-SIMS depth profiling of the Al concentration for annealing up to 300 °C. There, the sputter time is plotted versus the logarithm of the Al^+ intensity. The depth is proportional to the sputtering time if a constant ToF-SIMS sputter rate is assumed.

Compared to the first series of depth profiles (Fig. 5.5), the annealing temperature is much higher here. The zones can be divided similar as in the first profiles. In the initial part up to

300 s, the Al^+ signal is again flat and at a constant to level due to detector saturation. The rapid drop of the signal at the Al-Cu interface was already discussed at Fig. 5.6.

When analysing at the curvatures of the profiles of the samples annealed at 250 °C and 300 °C, the reaction zone becomes larger. Here, one can see an extreme rise in concentration compared to the other curves. According to the phase formation discussed in section 5.5 and the studies by YY Tan et al. [6], that fact can be explained by an even more pronounced phase formation due to the higher temperature. There, the compound Al_2Cu or already the compound Al_4Cu_9 may be formed.

Compared to Fig. 5.5 are the signals of the samples below 200 °C lower and are disappearing in the noise. Based on this circumstance, the annealing duration for series 2 were increased. Another detail to be seen in the 250 °C sample signal is a peak below 2000 s, however that was a measurement artefact due to the gun of the primary ion beam. Another interesting fact can be found in the detail. Therefore, a close up for Figure 5.6 in the range from 0 zu 500 s is shown in Fig. 5.7:

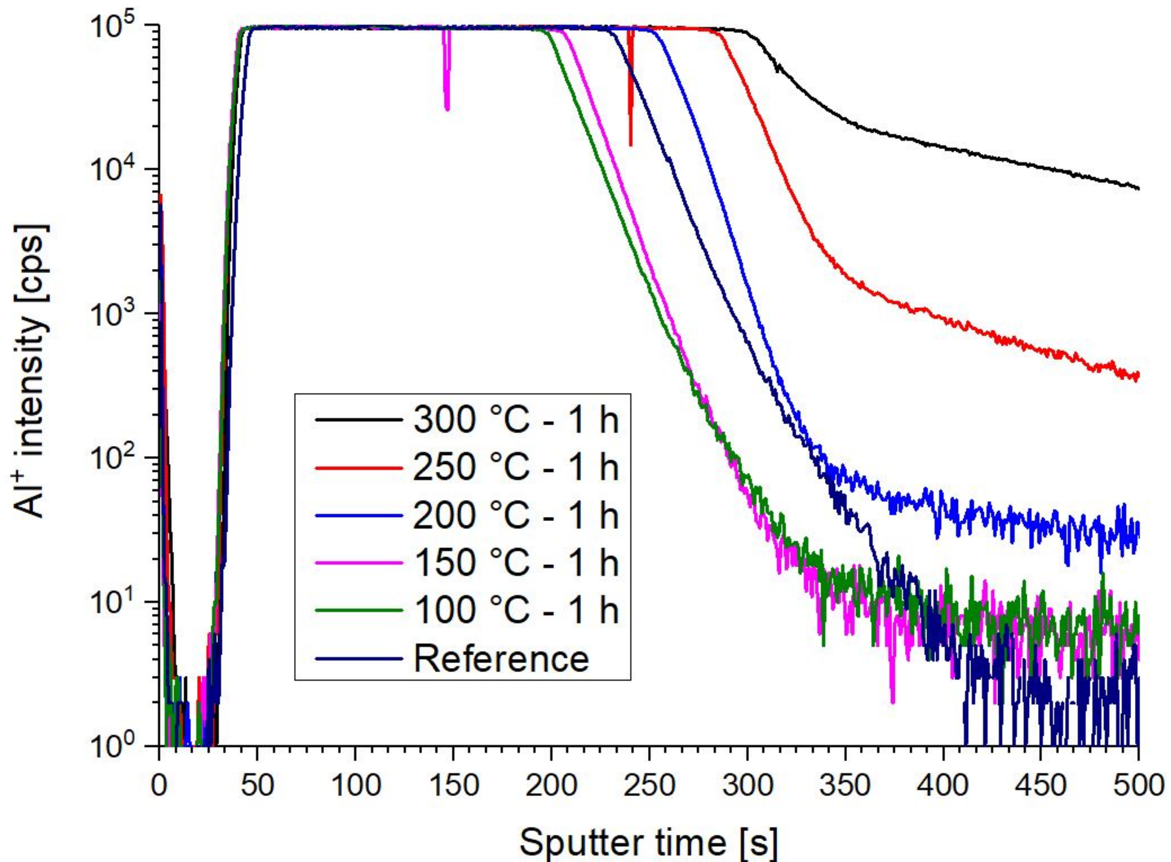

Fig. 5.7: ToF-SIMS depth profiling close up (initial 500 seconds) of the Al concentration for annealing up to 300 °C. There, the sputter time is plotted versus the logarithm of the Al^+ intensity. The depth is proportional to the sputtering time if a constant ToF-SIMS sputter rate is assumed.

There one can recognize that the different signals drop at different sputter times between 200 and 350 s, the Al layer seems to grow. That is a further result of of the start of the formation of intermetallic compounds. According to the Al-Cu phase-diagram (fig. 2.1) many possible phases can form. Previous studies [6] showed, that at first, Al-rich phases are forming. Over time and temperature, those are consumed by Cu-rich phases. So, phases in Al-Cu system are forming and disappearing again, dependent on time and temperature. In general it can be stated: the higher the temperature, the larger the phase.

Finally, the influence of the different deposition conditions on the diffusion behaviour is discussed. Therefore, 3 different samples were annealed for 1 h at 250 °C. The first sample was deposited at 60 °C at 10 mTorr with a thickness of 1 μm. There, small Cu grains (see Fig. 5.2) are created leading to a high density of grain boundaries per area. For the second

specimen, 2 μm of Cu were deposited at 320 °C at 3 mTorr Ar pressure. Here, the conditions are in Thornton's transition zone (see Fig. 2.6, Zone T) and Cu grains are starting to grow and to orient themselves columnar. The last sample is the one with 4.7 μm thickness of Cu deposited at 410 °C substrate temperature and 3 mTorr pressure. Here, large grains appear and ideal, but slower diffusion behaviour is expected. The corresponding ToF-SIMS measurements are shown in Fig. 5.8:

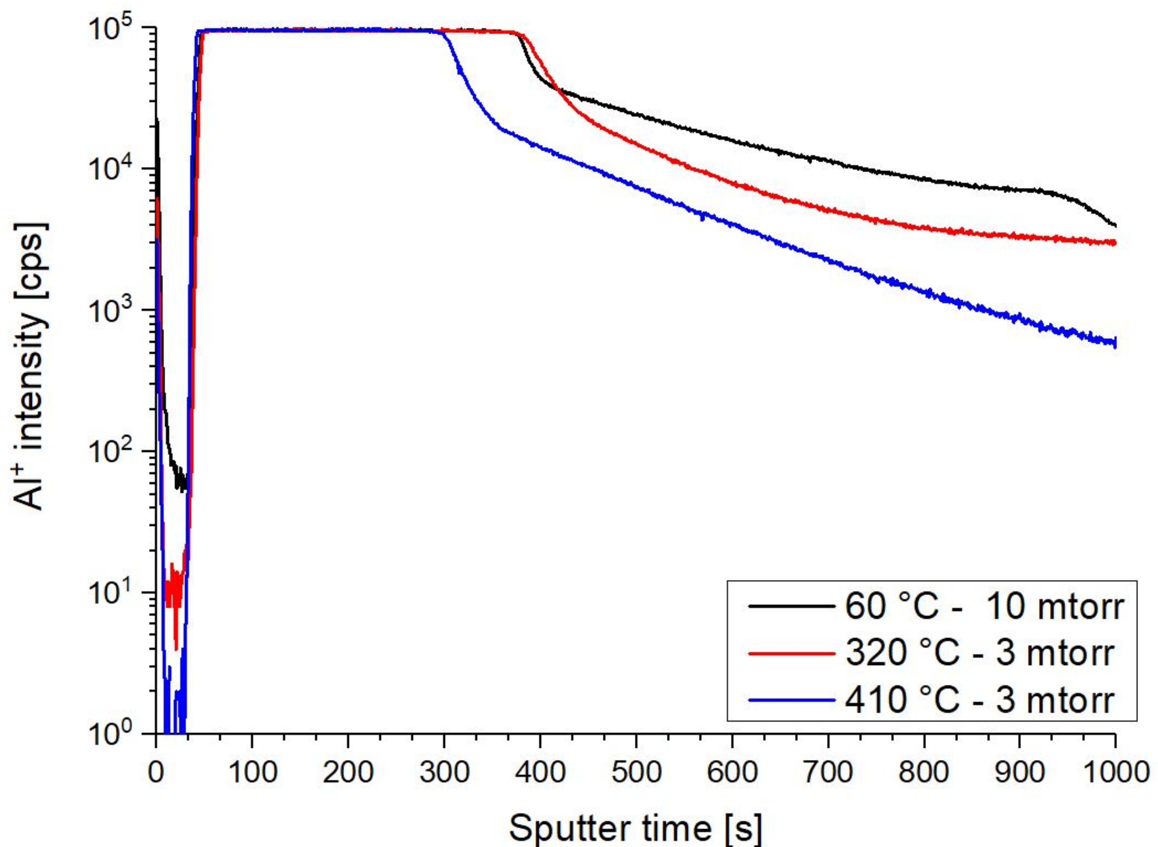

Fig. 5.8: ToF-SIMS depth profiles: 3 specimens deposited with different sputter conditions (see legend) and annealed afterwards at 250 °C for 1 h. There, the sputter time is plotted versus the logarithm of the Al^+ intensity. The depth is proportional to the sputtering time if a constant ToF-SIMS sputter rate is assumed.

Similar to the previous ToF-SIMS depth profiles, a saturated Al^+ signal is measured below the TiW layer. Then, the first obvious difference can be recognized. The signal of the samples with smaller grains drop later compared to specimen deposited at a substrate temperature of 410 °C. Higher grain boundary density per area due to small grains leads to a higher Al concentration in the Cu layer. Reaction can take place faster because of more Al atoms available. Furthermore, the Al^+ signal is enhanced for samples deposited the 60 °C and the

320 °C compared to the one at 410 °C. Increasing substrate temperature during deposition leads to larger grains. Less grain boundaries are available and therefore diffusion is slower. As a result, the diffusion behaviour of a layer can be tuned by varying the deposition conditions. It has to be taken into account that the sample produced with a substrate temperature of 60 °C was deposited at a lower temperature than the anneal afterwards (250 °C - 1 h). This leads to a further growth of the grains during annealing. This has to be taken into account for the development of new applications too.

5.5 Phase Formation in Al-Cu system

Phase formation in the Al-Cu system has already been investigated earlier (see, e.g., Ref. [6]) and is not the main objective of this thesis. However, due to its outstanding importance for the interpretation of the ToF-SIMS profiles, it will be briefly discussed here.

To demonstrate the occurrence of phase formation in the samples of this work and to be able to estimate the progress of phase growth, FIB (Fig. 5.9) and TEM (Fig. 5.10) analysis was performed.

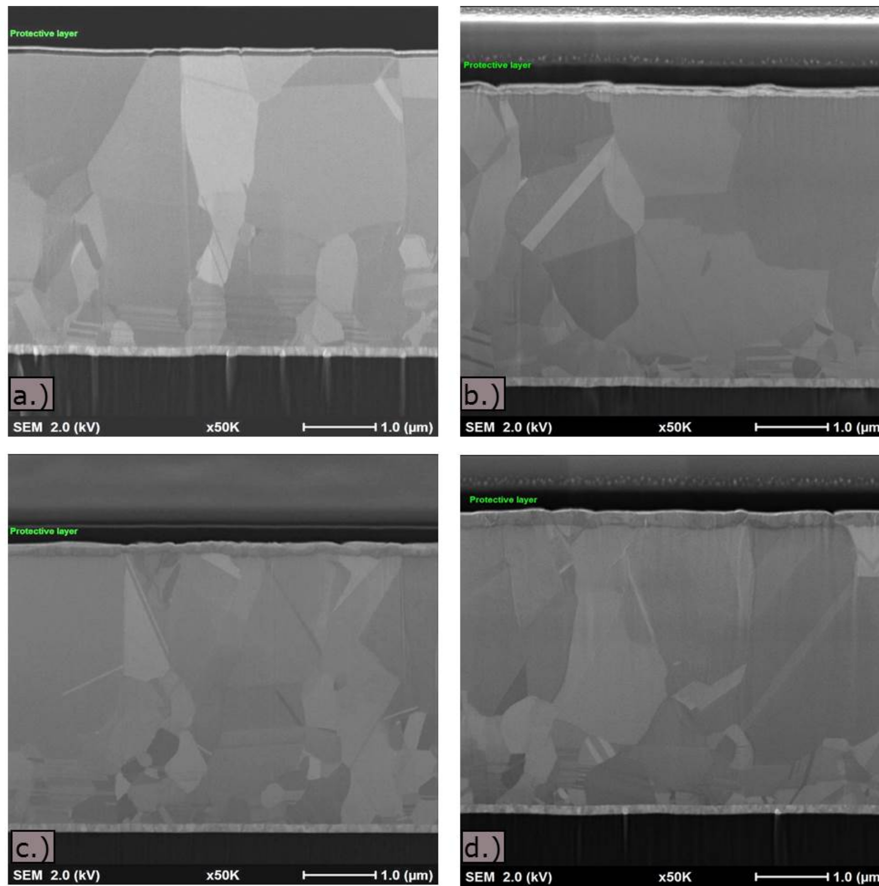

Fig. 5.9: FIB images of samples with a thickness of 4.7 μm Cu deposited at 410 °C for phase formation investigation after annealing at different temperatures for 1 h: a.) 100 °C - 1 h; b.) 200 °C - 1 h; c.) 250 °C - 1 h; d.) 300 °C - 1 h

When looking at the layers starting from the top of the FIB images, one can see a difference between Al and Cu layers. After annealing at 100 °C (a), the Al-Cu interface is sharp and no reaction process has taken place yet. After an anneal at 200 °C (b), IMC formation starts at the Al-Cu interface and one can see a white-gray shimmer. When taking a look at Fig. 5.7, the Al concentration of the sample annealed at 200 °C drops later than the reference measurement. That is a result of starting phase formation and growth into the Cu layer. For higher temperatures (c,d) the whole Al layer already reacted and a phase has formed. Due to its complexity, an identification of the phases was not possible. According to YY Tan [6], Al_2Cu or Al_4Cu_9 phases are possible in this temperature range. Furthermore, one can see a slight difference between 250 °C and 300 °C in color and size. The color can be an indicator for different phase formation. The size change occurs due to further phase growth (Fig. 5.7).

To get a closer look at the Al-Cu interface, TEM images for samples annealed at 100 °C and

300 °C were taken:

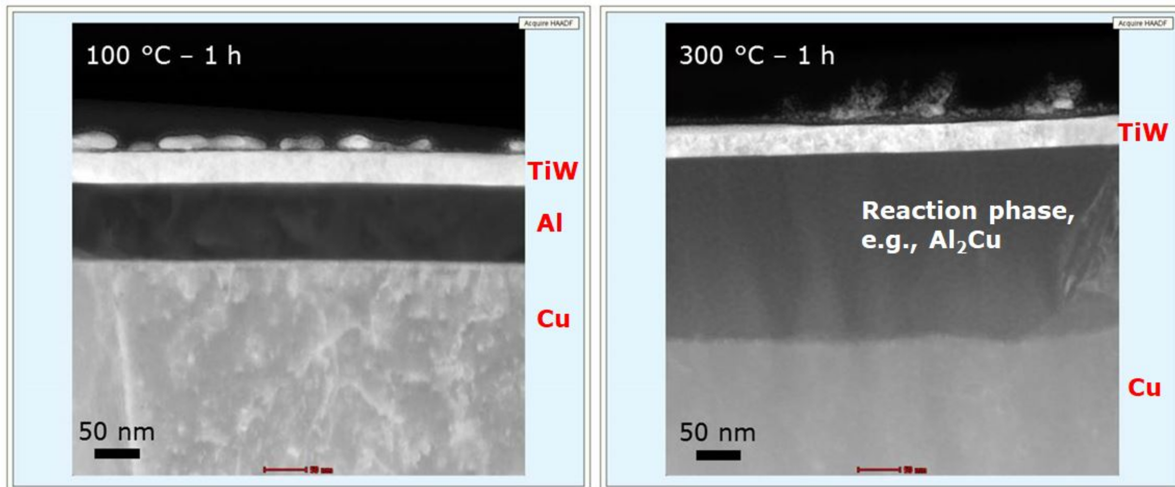

Fig. 5.10: TEM images for phase formation investigation for samples with a Cu layer thickness of 4.7 μm deposited at 410 °C: no reaction (100 °C - left panel) vs. full phase formation (300 °C - right panel)

There, a close-up of the Al-Cu interface is shown. While there is a 100 nm pure Al layer on the left hand side, one can see a different coloured, larger Al-Cu phase at the right side. This phase growth confirms what actually has been seen in the ToF-SIMS results (Fig. 5.6 and 5.7). According to YY Tan et al., the first phase to be formed should be the Al_2Cu-Phase at 175 °C to 200 °C. For 300 °C and longer annealing duration, many more possibilities exist, so that no clear identification of the phase was possible within this work.

Additionally, an EDX analysis (Fig. 5.11 and 5.12) for those 2 samples was performed. The linescan was across the Al layer starting in the TiW and reaching the Cu layer. In the upper image Fig. 5.11, one can clearly see 3 different phases. From 0 to 20 nm, the TiW layer can be seen. There is no sharp distinction between TiW and Al layer due to the natural line width of the measurement. From 20 to 102 nm, the Al layer is measured. Most important: there is no Cu in the Al layer yet showing that no interdiffusion and no reaction has taken place yet.

When looking at the second analysis (Fig. 5.12), this behaviour changed completely. After the 20 nm of TiW, the former Al layer can be seen. The big difference here is the high Cu concentration in the former Al layer, which even reaches the TiW-Al interface. That means that the layer is already fully consumed by a phase and interdiffusion has taken place. Here, the theory for ideal diffusion is not applicable anymore and no temperature dependence of the diffusivity could be determined due to the different diffusion mechanisms and coefficients for

each phase. Phase identification using EDX is not straight forward, so that signal comparison does not tell much about element ratio.

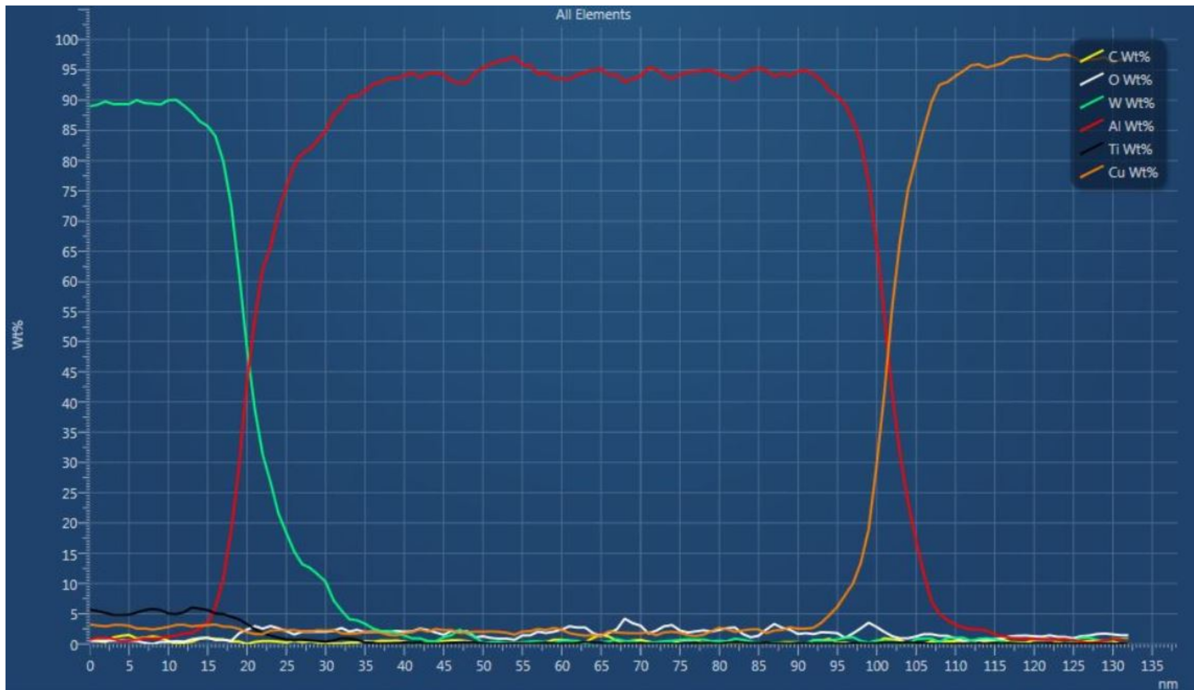

Fig. 5.11: EDX analysis for a sample with a Cu thickness of 4.7 μm deposited at 410 °C for phase formation investigation annealed at 100 °C for 1 h

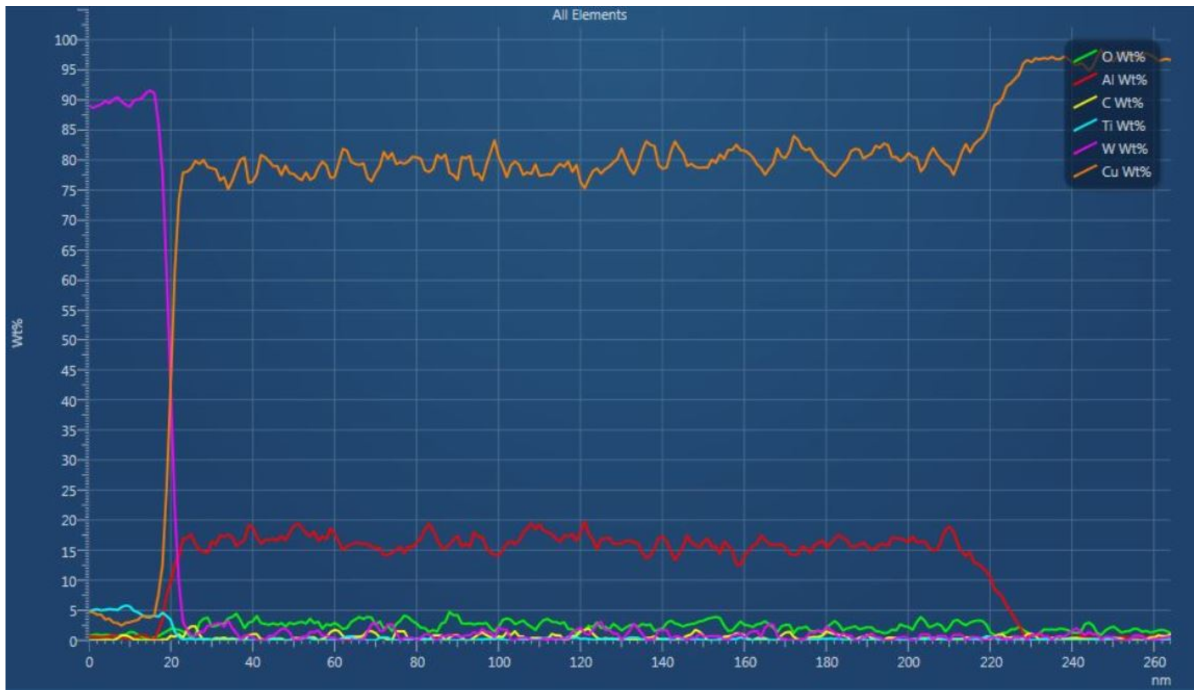

Fig. 5.12: EDX analysis for a sample with a Cu thickness of 4.7 μm deposited at 410 °C for phase formation investigation annealed at 300 °C for 1 h

5.6 Determination of the temperature dependence for Al-Cu Diffusion using FDM

In diffusion research, the determination of the activation energy for diffusion mechanisms is one of the fundamental tasks. There are several different experimental approaches such as SIMS or radiotracer methods to obtain depth profiles. Fitting of these profiles gives diffusion coefficients. One well-established approach is the already described Crank-Nicolson finite difference method used in this thesis. The fitting procedure is a complicated task and is not described here.

In general, the diffusion coefficients obtained show a specific temperature dependent behaviour, according to an Arrhenius behavior:

$$D = D_0 \cdot e^{-\frac{E_a}{k_B T}} \tag{5.3}$$

Here, D is the diffusion coefficient, D_0 is the pre-factor, E_a the activation energy, k_B the Boltzmann constant and T the temperature. When measuring diffusion coefficients at different temperatures, a plot ln(D) vs. 1/T is then linear and can be fitted to obtain E_a

and D_0. Such a plot is shown in Fig. 5.13:

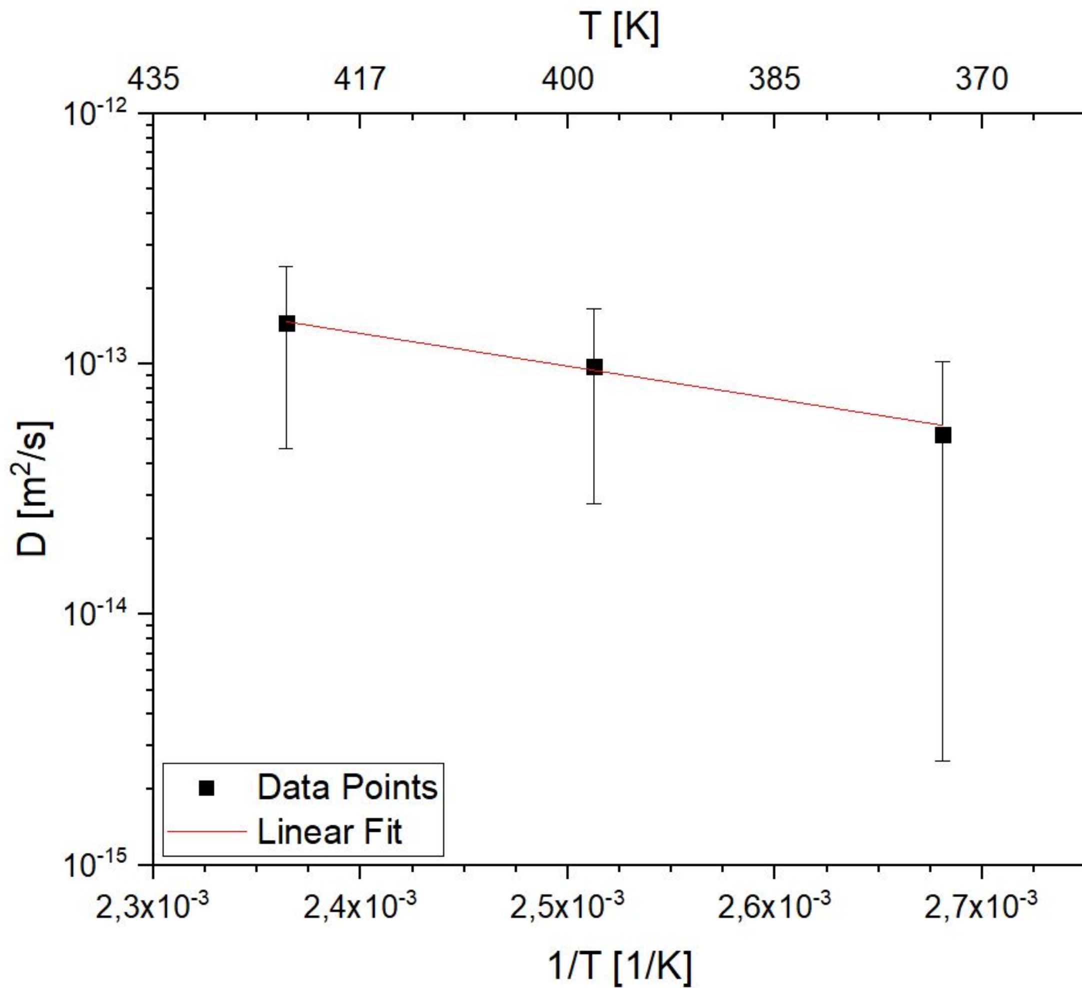

Fig. 5.13: Arrhenius plot for fitted diffusion coefficients at 100 °C, 150 °C and 200 °C for different annealing duration.

The diffusion coefficients obtained in this work show this linear behaviour, however, several remarks why a activation energy determination is impossible have to be made. The numerical error of a diffusion coefficient fit is about half a magnitude, consisting of:

- Numerical errors because of the method
- Measurement errors during ToF-SIMS depth profiling (interface effects, roughness ...)
- data quality (noise)

In this plot, the resulting error bars would be larger than the whole plot making an accurate fit impossible. Another issue is the temperature range. Diffusion experiments for reliable

determination of activation energies are normally performed for temperature ranges of 600 K or more. Here, only a limited range with 100 K variation is possible without the occurrence of reaction processes. Furthermore, the layer thickness has a major role as well. In general, diffusion experiments are performed with mm thick layers to avoid saturation, i.e., that the condition of $\frac{dc}{dx} = 0$ at the far end is still valid. In comparison, here only thin layers with a maximum thickness of 4.7 μm were used.

5.7 Mechanical Characterization

Additionally to the SIMS analysis and FIB/TEM investigations of the intermetallic phases, mechanical characterization via NanoIndentaion is possible as well. The main idea is the following: when the Cu grain boundaries are filled with Al atoms via grain boundary diffusion, e.g., C-regime-diffusion similar to the Al segregation between the grains, hardening of the layer is expected [36, 37]. Thus, the mechanical properties of polycrystalline material can be tuned by diffusion-reaction of atoms. With the NanoIndentation method, it is possible to determine mechanical properties such as hardness or Young's modulus from a force-displacement curve. The results of those measurements are shown in figures 5.14 and 5.15. To eliminate errors due to local variations, 20 measurements per curve were performed and averaged:

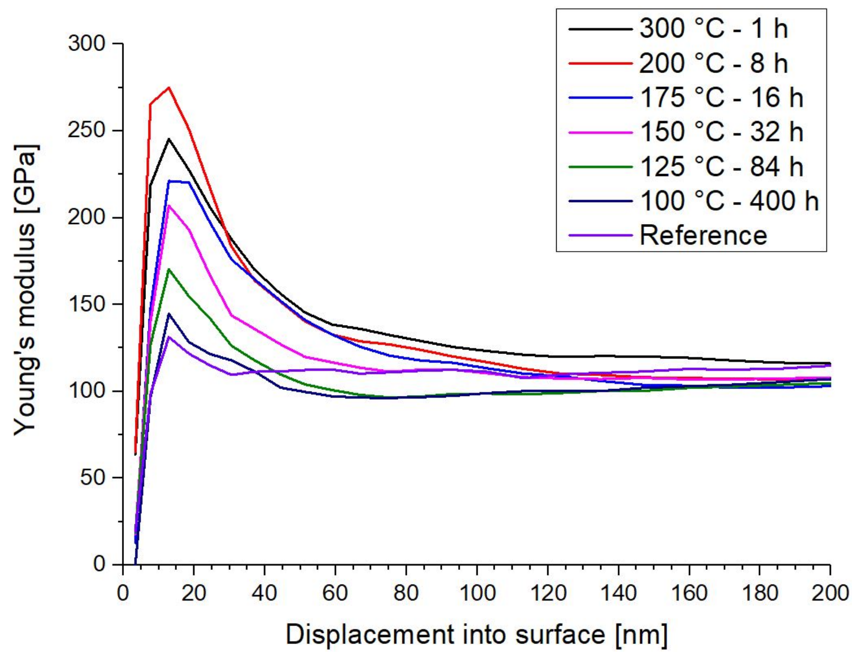

Fig. 5.14: NanoIndentation measurement of Young's modulus for various annealing conditions in a range of 100 °C for 400 h to 300 °C for 1 h. The sample contains a Cu layer of 4.7 μm thickness deposited at 410 °C.

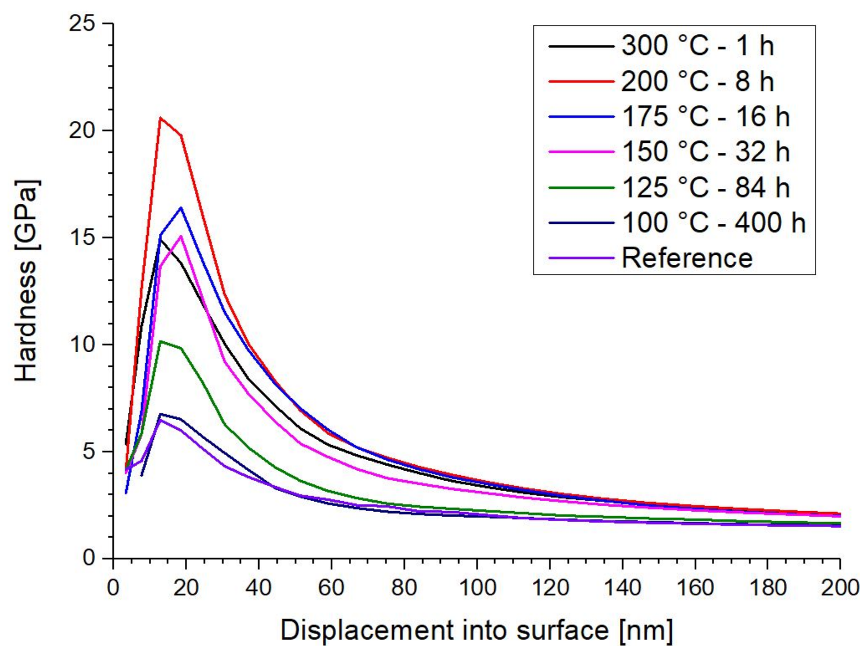

Fig. 5.15: NanoIndentation measurement of hardness for various annealing conditions in a range of 100 °C for 400 h to 300 °C for 1 h. The sample contains a Cu layer of 4.7 μm thickness deposited at 410 °C.

The averages for all the signals show a clear trend: the higher the annealing temperature, the harder the material. The rise from zero to a maximum peak is a NanoIntendation artefact. Due to the fact that the tip interacting with the surface has a round shape, it needs some distance till the full pressure is applied. Another important issue is the interaction volume. For hardness, 3 times the displacement into the surface is actually measured. That means, if the tip is displaced 30 nm into the surface, the measured volume contains actually information from a depth of 90 nm. For Young's modulus measurements, even 10 times the displacement is measured [25].

For the temperatures from 100 °C to 175 °C, one can see a rise in hardness and Young's modulus. But those results have to be taken with care. Here, all the layers are actually measured together, the TiW, Al and the Cu layer. It cannot directly be proven, that the increase in total hardness with increasing annealing temperature is only due to the effect of copper. But several experiments in other projects have shown, that no big difference in TiW hardness with changing temperature has been observed. Another interesting fact is the behaviour of the sample that has been annealed at 300 °C, of which the hardness and the modulus is actually lower than the one of the one annealed at 200 °C. One possible explanation is the formation of different phases. At low temperatures, Al-rich phases come up while at higher temperatures, Cu-rich phases dominate. It might be that more Al means harder material, but at 300 °C, already Cu richer phases form what leads to a decrease in hardness and modulus. Another fact is, that Al becomes ductile from 250 °C upwards leading to a decrease in total hardness.

5.8 NanoSIMS Investigations

Due to its superior lateral resolution, nanoSIMS is able to detect atoms on the nm-scale and for instance the localization of atoms can be determined that way. For this work, these features of the nanoSIMS method are used to visualize the distribution of Al atoms at specific depths. The initial questions were: Where are the Al atoms located? Is there only grain boundary diffusion? When and where takes reaction place? According to those points, 2 specimens were selected: samples with a deposited Cu thickness of 4.7 μm at 410 °C annealed at 100 °C for 400 h and at 200 °C for 8 h. The sample deposited at 410 °C has large grains with a diameter in μm range. For the comparable low annealing temperature of 100 °C, no phase formation processes are expected. An anneal of 200 °C is, according to YY Tan [6], high enough to trigger IMC formation. Due to the low sputter rate of the nanoSIMS technique [20], craters in specific depths have been prepared via ToF-SIMS.

The first specimen to investigate was the one annealed at 100 °C for 400 h. There, only diffusion is expected. The ToF-SIMS depth profile with the measurement location for nanoSIMs are shown in figure 5.16:

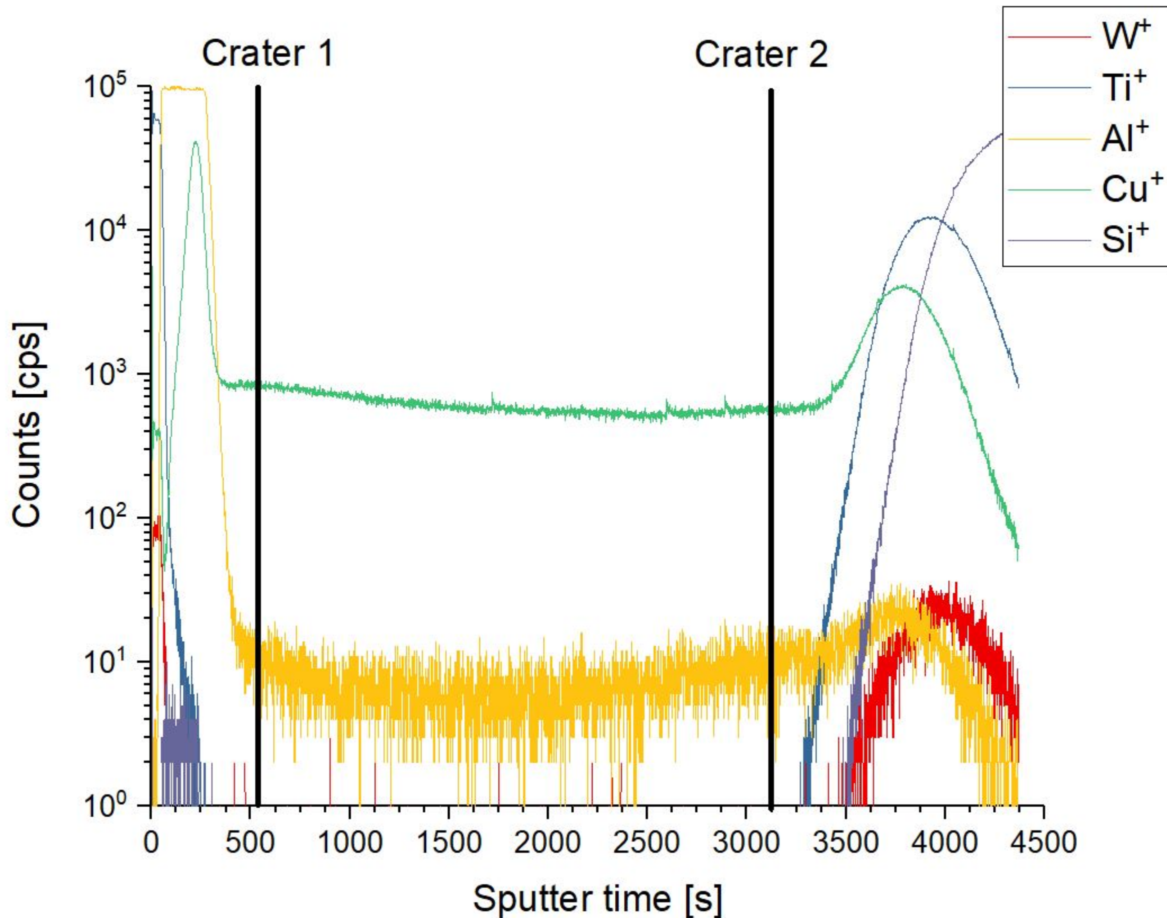

Fig. 5.16: ToF-SIMS depth profile of 100 °C - 400 h sample with marked crater depth for nanoSIMS investigations. There, the sputter time is plotted versus the logarithm of the Al^+ intensity. The depth is proportional to the sputtering time if a constant ToF-SIMS sputter rate is assumed.

The bottom of the two craters in this sample are located in depths, where only grain boundary diffusion should take place. To verify this, the position of Al atoms is determined making use of the good lateral resolution of nanoSIMS. The depths of the prepared craters were measured using a Dektak profilometer.

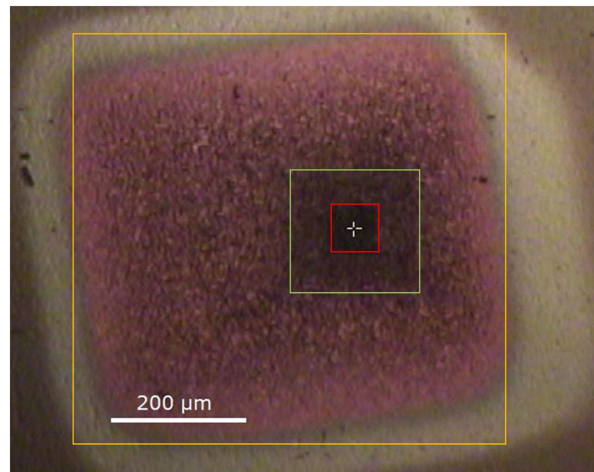

Fig. 5.17: Micrograph of the ToF-SIMS crater 1 with a nanoSIMS measurement spot for the sample annealed at 100 °C for 400 h; orange: ToF-SIMS prepared crater; green: pre-cleaned spot via nanoSIMS; red: nanoSIMS measurement spot

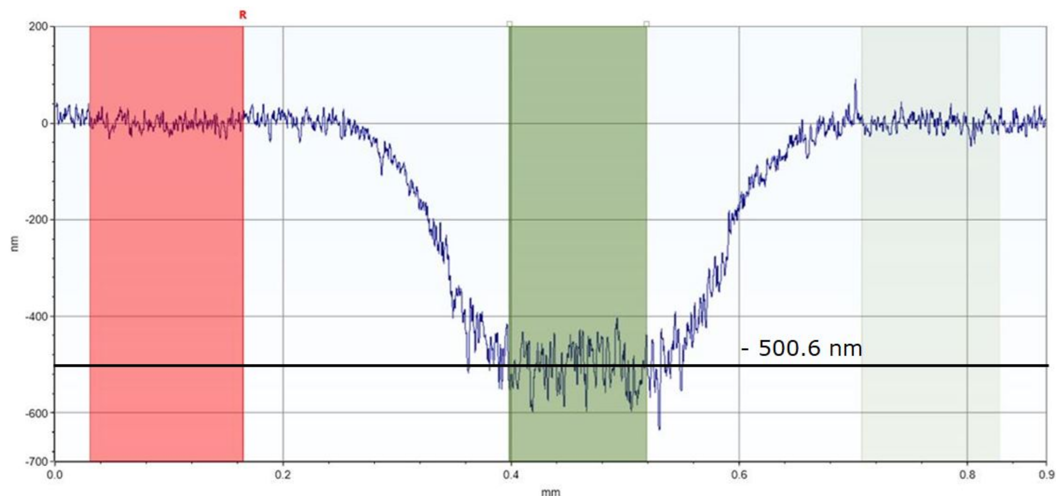

Fig. 5.18: Depth profile across the ToF-SIMS crater 1 taken from the specimen that had been annealed at 100 °C for 400 h. The mean depth: -500.57 nm

The first measurement was performed in a depth of approximately 500 nm. According to the ToF-SIMS depth profiles from the previous chapter, only grain diffusion processes should take place there. The corresponding nanoSIMS images are shown in figure 5.19

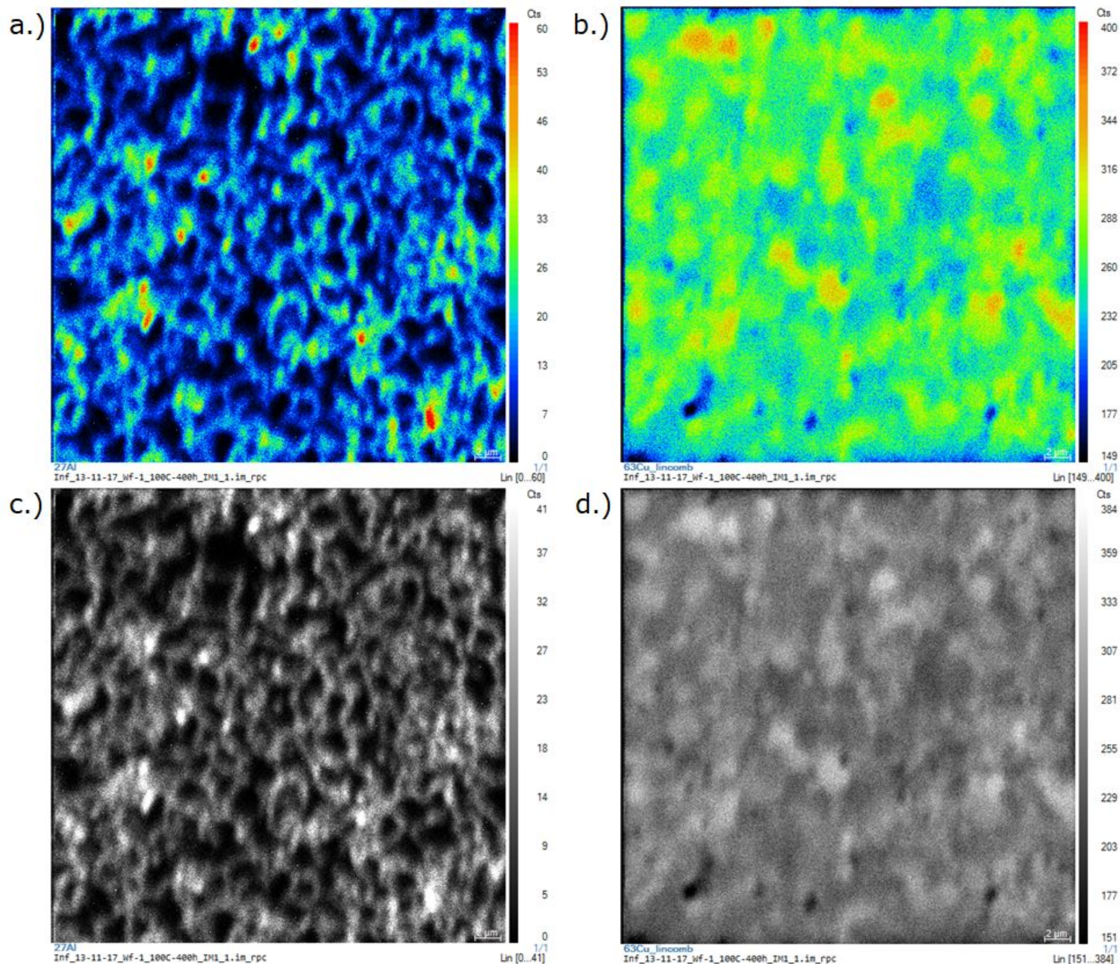

Fig. 5.19: Micrographs of the nanoSIMS measurement for the specimen annealed at 100 °C for 400 h, crater 1 (40 μm x 40 μm area): a.) ^{27}Al signal (heatmap, red: 60 counts, black 0 cts); b.) ^{63}Cu signal (heatmap, red: 400 counts, black: 149 counts); c.) ^{27}Al signal (black-white, white: 41 counts, black: 0 counts); d.) ^{63}Cu signal (black-white, white: 384 counts, black: 151 counts)

The ^{27}Al images on the left hand side (Fig. 5.19 a.) and c.)) show the Al distribution. As expected, the Al atoms are only found at the grain boundaries, i.e., they decorate the grain boundaries. Some hotspots (red spots in Fig. 5.19 a.): 60 counts) can be seen as well. Those appear because of a higher density of grain boundaries (if smaller grains appear) or because of pinholes within the Cu-layer, that create diffusion paths for Al atoms. Therefore, the main information is, that grain boundary diffusion is actually the only diffusion mechanism in this depth after an anneal of 100 °C for 400 h. The ^{63}Cu signal seen in Fig. 5.19 b.) and d.) show no remarkable spots. The difference in counts and therefore in colour comes from different signals due to, e.g., different orientation of the Cu grains. The black-white

images in c.) and d.) can be used to estimate the shape of the Cu grains.

The second crater investigated is in a much larger depth. Here, the question of what happens in the "saturation" zone of the ToF-SIMS profile has to be answered. When looking at Fig. 5.6, a stagnation of Al concentration can be seen at sputter times higher than 2000 seconds. As mentioned in section 5.4 can this be an indication for saturated grain boundaries. Furthermore, this measurement should also give information about the rise of intensity in Al^{+} signal upon approaching the Cu-TiW interface.

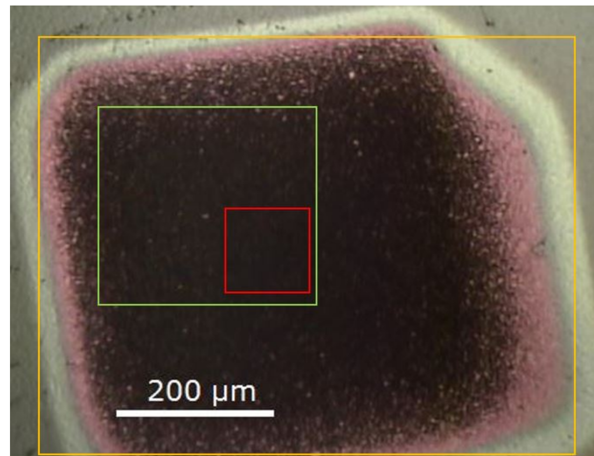

Fig. 5.20: Micrograph of the ToF-SIMS crater 2 with a nanoSIMS measurement spot for the sample annealed at 100 °C for 400 h; orange: ToF-SIMS prepared crater; green: pre-cleaned spot via nanoSIMS; red: nanoSIMS measurement spot

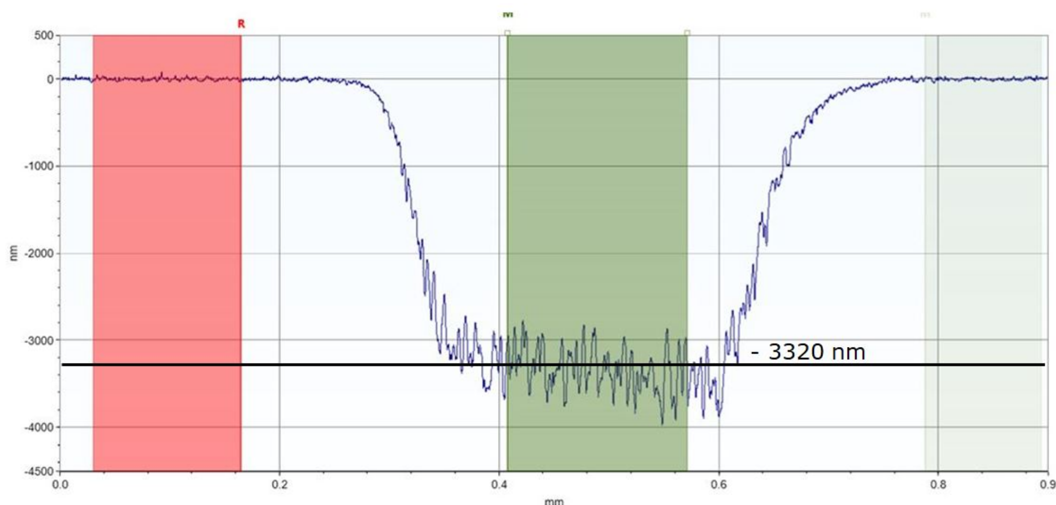

Fig. 5.21: Depth profile across the ToF-SIMS crater 2 taken from the specimen that had been annealed at 100 °C for 400 h. The mean depth: -3321.90 nm

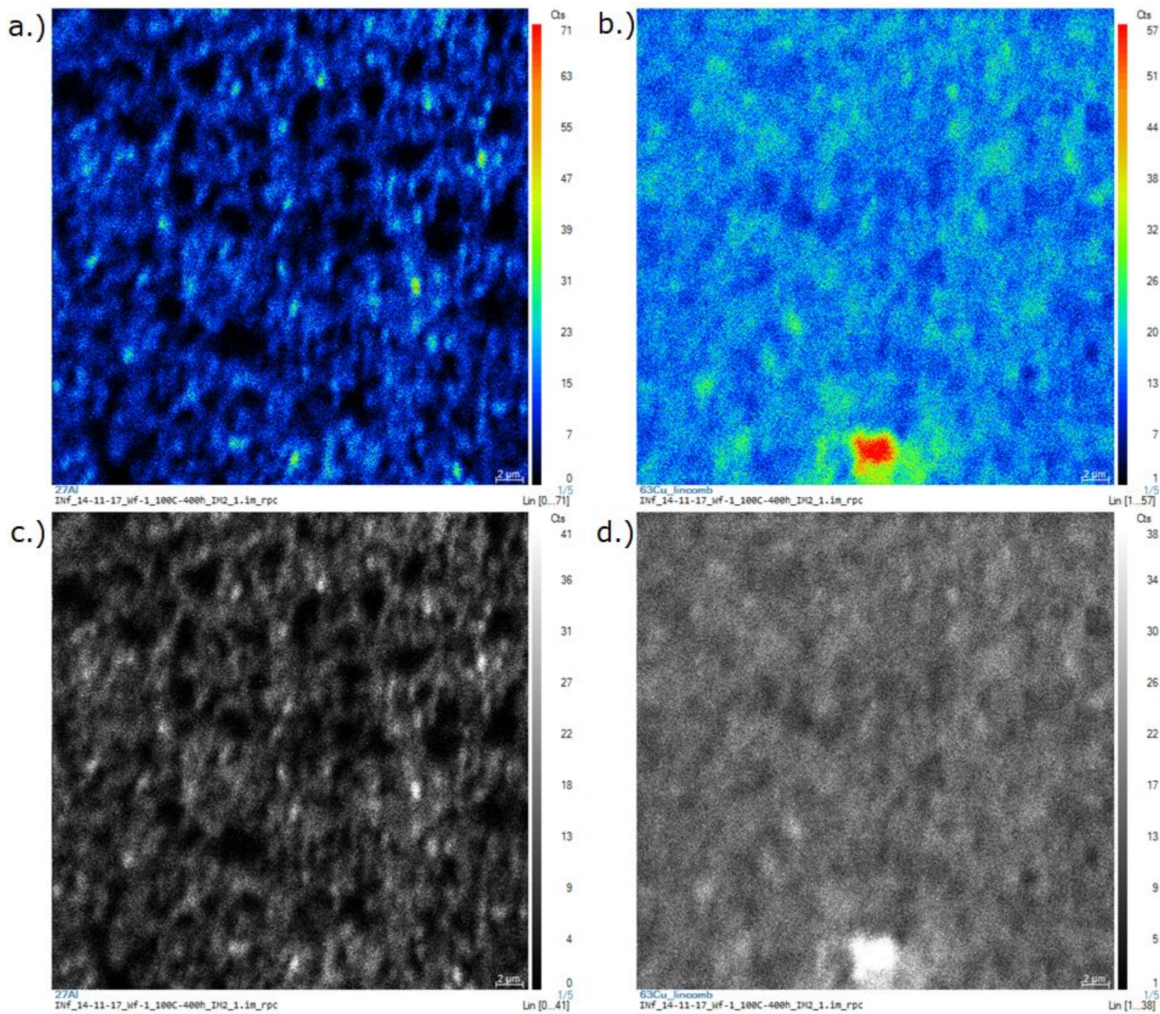

Fig. 5.22: Micrographs of the nanoSIMS measurement for the specimen annealed at 100 °C for 400 h, crater 2 (40 μm x 40 μm area): a.) ^{27}Al signal (heatmap, red: 71 counts, black: 0 counts); b.) ^{63}Cu signal (heatmap, red: 57 counts, black: 1 count); c.) ^{27}Al signal (black-white, white: 41 counts, black: 0 counts); d.) ^{63}Cu signal (black-white, white: 38 counts, black: 1 count)

As one can see in Fig 5.22, the Al atoms are arranged at the grain boundaries as well. The rise in intensity in ToF-SIMS depth profile is therefore not only a measurement specific effect. Furthermore, some of the grains seem smaller than in a depth of 500 nm. That issue would match with the fact found in FIB images, that the grain size becomes smaller upon approaching the lower TiW interface due to grain growth mechanisms. A comparison of Fig. 5.19 d.) and Fig. 5.22 d.) shows, that the distinct Cu grains seen in a depth of 500 nm disappeared for a depth of 3000 nm. That matches the fact mentioned above, that Cu grains are smaller closer to the lower Cu-TiW interface due to grain growth. So the rise in intensity can either be due to the enhanced grain boundary density or simply due

to the saturation with Al atoms, what implies that the laws of diffusion are not valid anymore.

In the ^{65}Cu image (Fig. 5.22 b.) and d.)), a hotspot at the lower edge of the picture can be found. However, this is actually a ^{28}Si contamination. This can be interpreted as a Si-Cu interface and therefore, SIMS typical interface/matrix effects appear explaining the enhanced Cu signal in that area.

The second sample investigated had been annealed at 200 °C for 8 hours. At that point, reaction process should have already started [6]. As an hypothesis, reaction should preferentially take place at the grain boundaries due to higher Al atom concentration there. The crater here is again in a depth of approximately 500 nm and therefore comparable to the sample before, where a reaction was not observed.

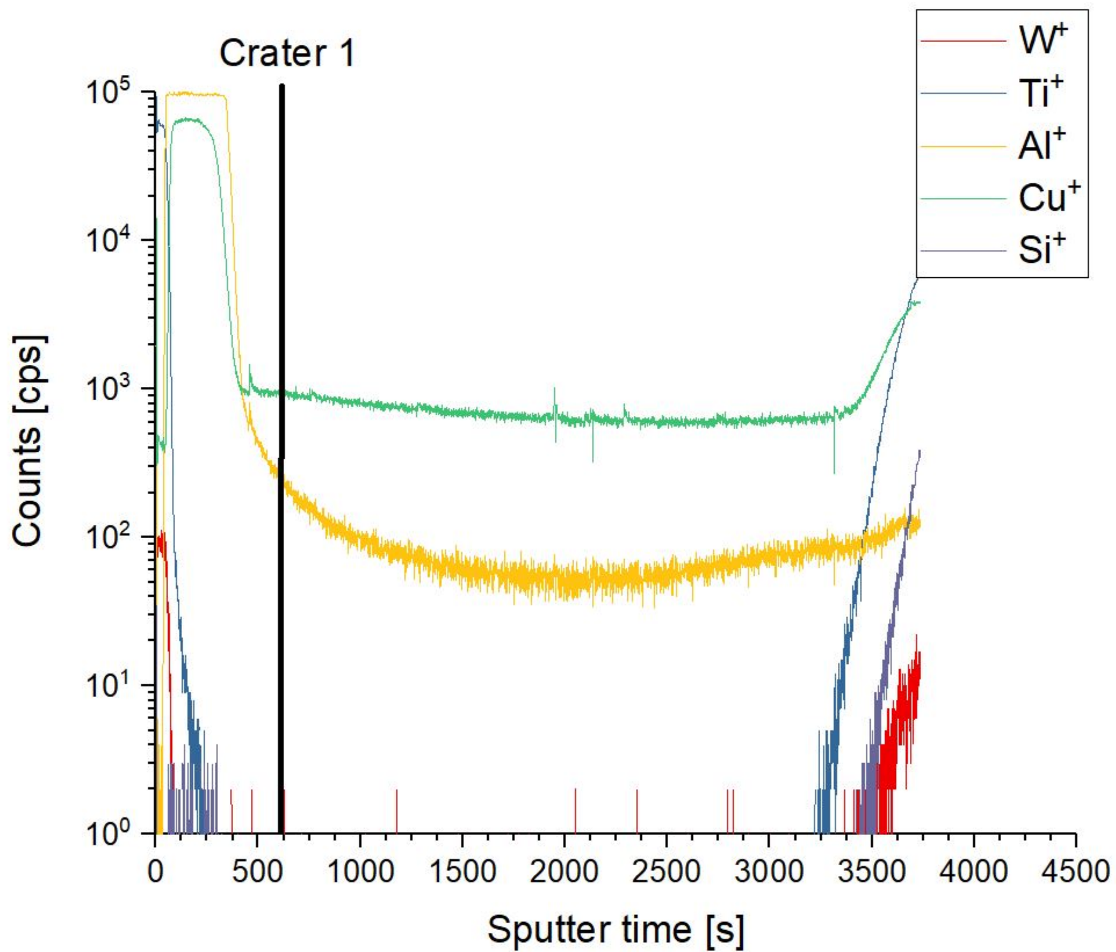

Fig. 5.23: ToF-SIMS depth profile of 200 °C - 8 h sample with marked crater depth for nanoSIMS investigations. There, the sputter time is plotted versus the logarithm of the Al^+ intensity. The depth is proportional to the sputtering time if a constant ToF-SIMS sputter rate is assumed.

Now in that area of the ToF-SIMS depth profile, one can see an enhanced Al concentration due to reaction processes. More the interesting question is: Are the Al atoms distributed differently compared to the specimen without reaction?

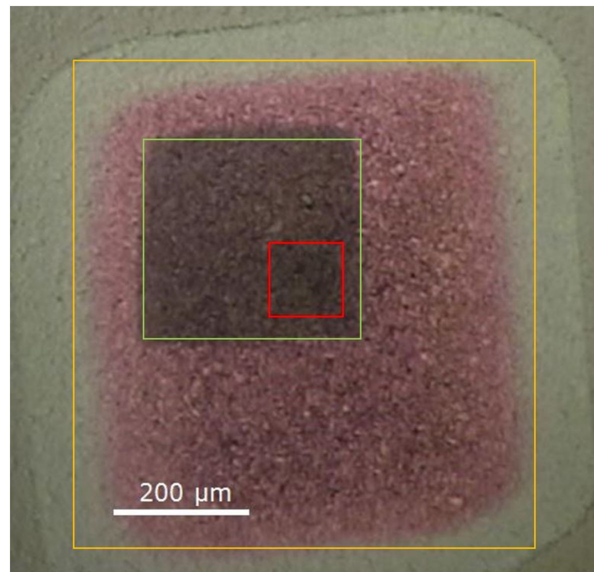

Fig. 5.24: Micrograph of the ToF-SIMS crater with a nanoSIMS measurement spot for the sample annealed at 200 °C for 8 h; orange: ToF-SIMS prepared crater; green: pre-cleaned spot via nanoSIMS; red: nanoSIMS measurement spot

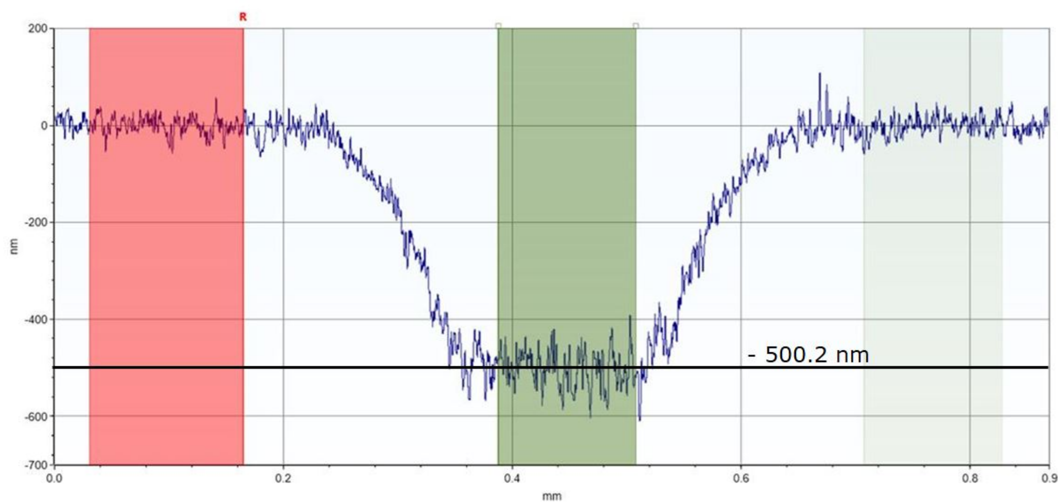

Fig. 5.25: Depth profile across the ToF-SIMS crater taken from the specimen that had been annealed at 200 °C for 8 h. The mean depth: -500.15 nm

As in the previous images (Fig. 5.19 and 5.22) already seen are the Al atoms again distributed at the grain boundaries and several Al hotspots appear (Fig. 5.26 a.)). In the images before, those hotspots belonged to an enhanced grain boundary concentration, e.g., at points were 3 grains met each other. Smaller Cu grains lead to an enhanced Al signal as well. In the case of the sample annealed at 200 °C, IMC formation has to be considered as well. One big difference this time can be found when looking at the Cu image (Fig. 5.26 b.). The Al hotspots are at

the same position as the Cu hotspots. Comparing this fact to Fig. 5.19, one can see that at that points, no hotspots in the Cu signal can be seen. One possible explanation for this issue is starting phase formation at those locations. Furthermore this phase formation seems to start at the grain boundaries. There, several explanations are possible. The hypothesis used in this thesis was IMC formation due to higher Al concentration due grain boundary diffusion. Considering the fact, that some of those hotspots are found at triple grain boundaries, other effects influencing the reaction behaviour can be imagined as well. This was not covered in this work.

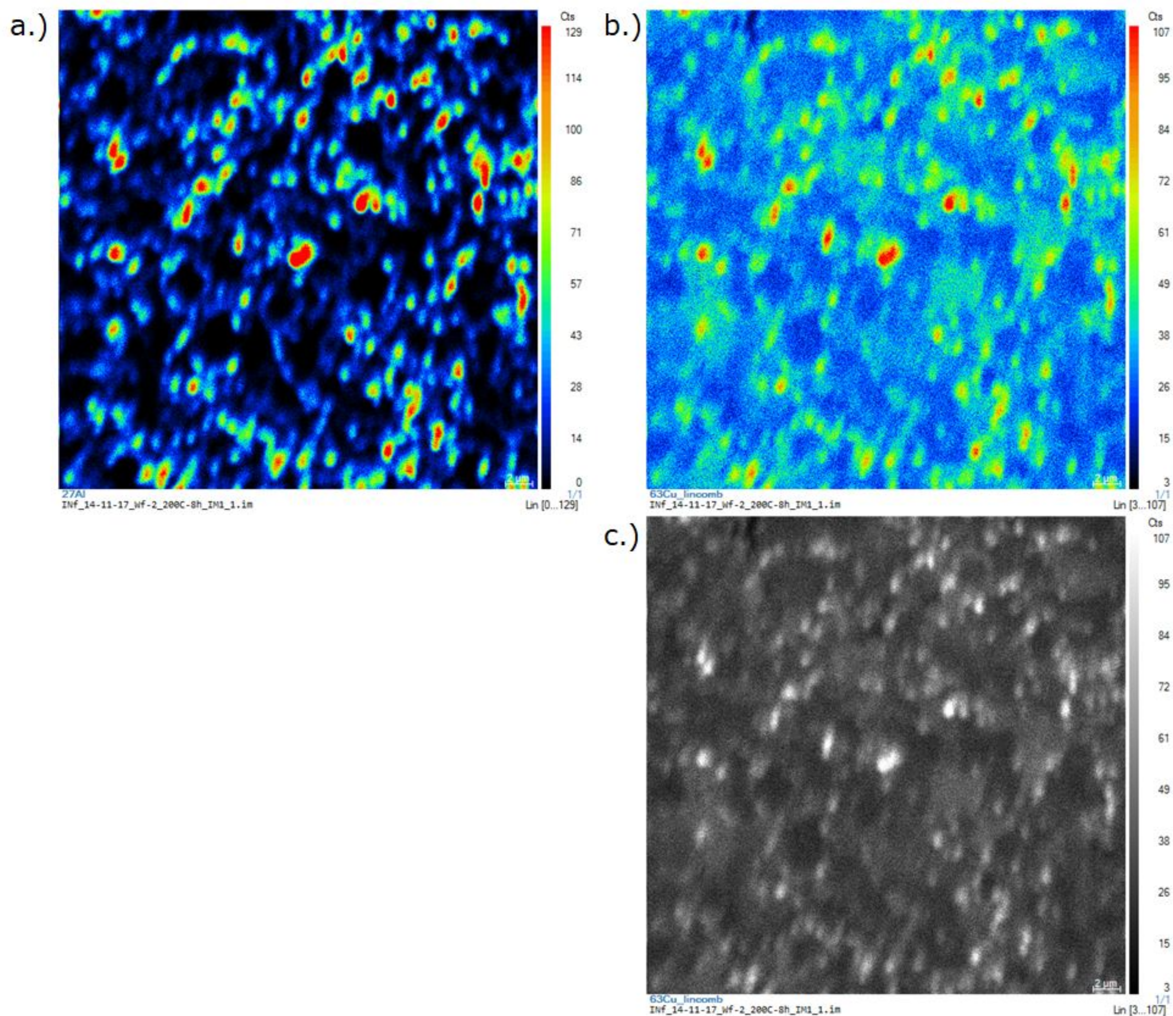

Fig. 5.26: Micrographs of the nanoSIMS measurement for the specimen annealed at 200 °C for 8 h (40 μm x 40 μm area): a.) ^{27}Al signal (heatmap, red: 129 counts, black: 0 counts); b.) ^{63}Cu signal (heatmap, red: 107 counts, black: 3 counts); c.) ^{63}Cu signal (black-white, white: 107 counts, black: 3 counts)

6 Simulation Results

6.1 The Diffusion Model for a NiV-Cu and Ag-Cu

Another important part of this work deals with the simulation of diffusion processes. Now, the application of FEM basics mentioned in chapter 4 will be discussed. The first model considered is the classical diffusion model based on the works by Fick. Here, Fick's second law is solved using FEM and FEniCs. Examples for material systems where this simulation can be applied to are Ni-Cu and Ag-Cu. According to their phase diagrams, those are materials that are completely miscible and where a reaction does not occur even up to high temperature.

Furthermore, Arrhenius laws for bulk- and grain boundary diffusion were determined from data obtained with the radiotracer diffusion method (Divinski at el. [7, 8]). Those values were implemented into the diffusion-only model. The code used for the the model itself will not be discussed here, but can be found in the appendix of this thesis.

The first step in building up a simulation is creating a proper model. Therefore, as described in section 4.2.2, the Gmsh program was used. The ideal model for diffusion consists of columnar grains with straight grain boundaries, where diffusion can take place. As the easiest possible representation, this model was used in the first step. Finally, this model was meshed to create the nodes for the calculation (6.1). This model can be used for the simulation of material systems with columnar grains and grain boundaries under an angle of 90 $^{\circ}$ with respect to the surface. Copper is, as seen in previous FIB images (Fig. 5.3), not columnar under the conditions chosen in that work. Some Cu phases, e.g., the Al-Cu phase, are columnar under these circumstances. Due to it's simplicity and applicability to Fick's model of diffusion, this was the first model to be used for simulation.

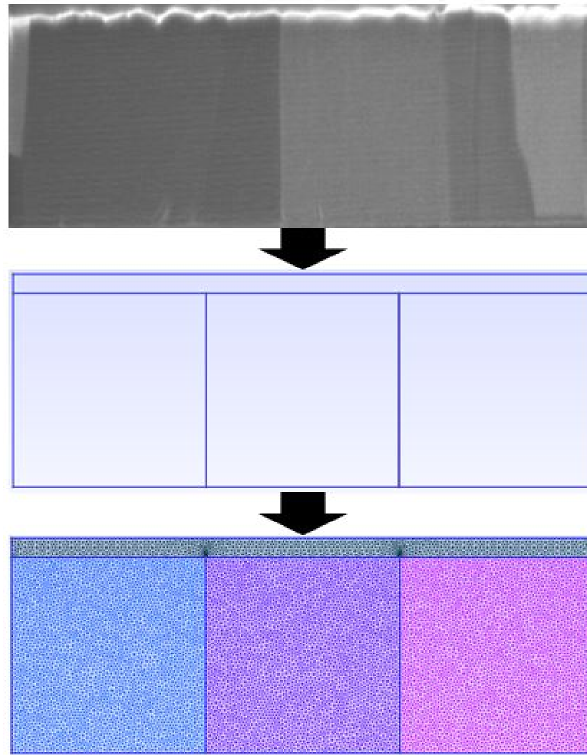

Fig. 6.1: From FIB image to mesh: Here, a SEM image of an Al-Cu layer with TiW on top was taken after a FIB cut. The picture was redrawn in Gmsh and meshed with finite CG elements.

Here, grain boundaries with a width δ of $\sim$ 0.5 nm were used which is consistent to literature (e.g. [15]) and the grain size (or distance between to neighbouring grain boundaries) was taken to be 1 μm, representing an average value for several grains. The values for d and δ can be easily adjusted by changing the model. In the program, the diffusion coefficients D_b and D_{gb} as well as the simulation (= annealing) time and the number of steps can be chosen. For systems like Ni-Cu or Ag-Cu, where Arrhenius laws are available, the temperature T substitutes D_b and D_{gb}. Those values have not to be specified in that case anymore. At first Fig. 6.2 and Fig. 6.3 show the simulation results for a fictive diffusion system with $D_{gb} = 10^{-10}$ cm^2/s and $D_{bulk} = 10^{-16}$ cm^2/s for a diffusion duration of $t = 1000$ s. These simulation are used to demonstrate the influence of various diffusion times on the resulting diffusion profile. Furthermore, these conditions can be used as approximate values for diffusion of Al in Cu estimated from ToF-SIMS depth profiles at 150 °C. In comparison to that, Fig. 6.4 shows the results of a simulation, where the grain boundary diffusion coefficient is varied over 4 magnitudes (10^{-9} cm^2/s to 10^{-12} cm^2/s) for a simulation time of 1000 s. This serves as a demonstration of how a variation of the diffusion coefficient influences the overall diffusion

behaviour. The evolution of the depth profile for the case of D_{gb} of 10^{-12} cm^2/s for different time steps is shown in Fig. 6.5.

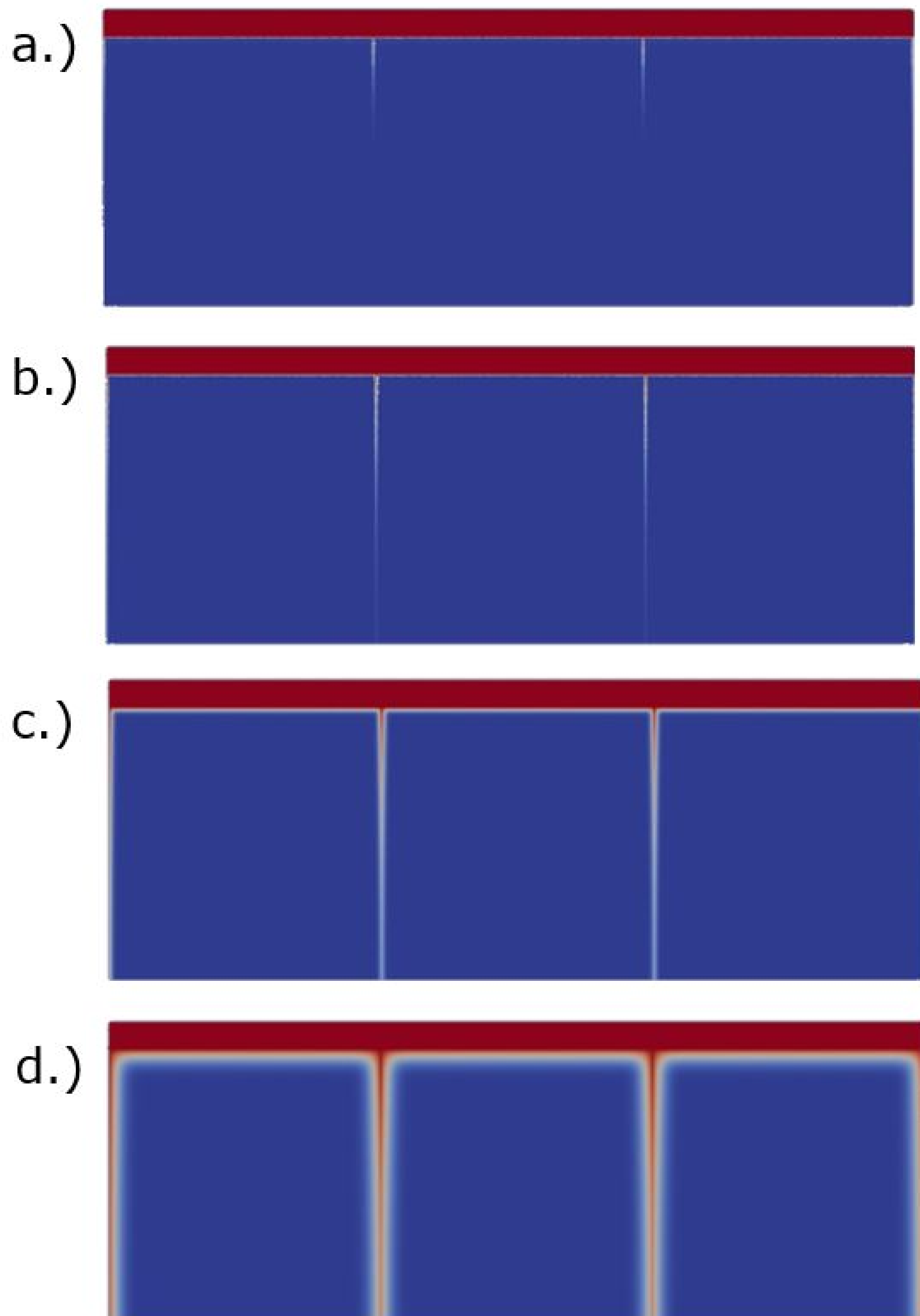

Fig. 6.2: Simulation of a diffusion system with columnar grains and grain boundaries orientated at an angle of 90 ° with respect to the surface with $D_{gb} = 10^{-10}$ cm^2/s and D_{bulk} of 10^{-16} cm^2/s for a duration of 1000 s: a.) 1 s; b.) 10 s; c.) 100 s; d.) 1000 s; The concentration is coded in a linear color scale: blue = 0, red = 1

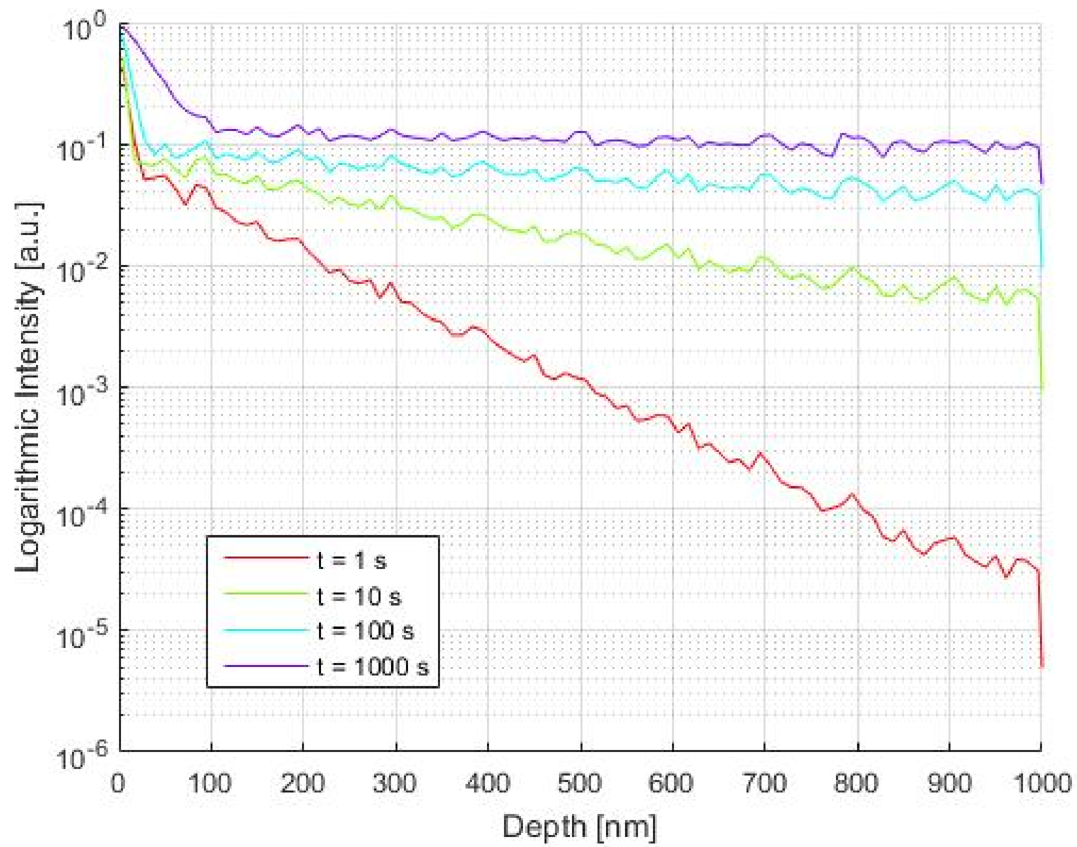

Fig. 6.3: Depth profile of the atom concentration for a diffusion system with columnar grains and grain boundaries orientated at an angle of 90 ° with respect to the surface with $D_{gb} = 10^{-10}$ cm^2/s and D_{bulk} of 10^{-16} cm^2/s for a duration of 1000 s

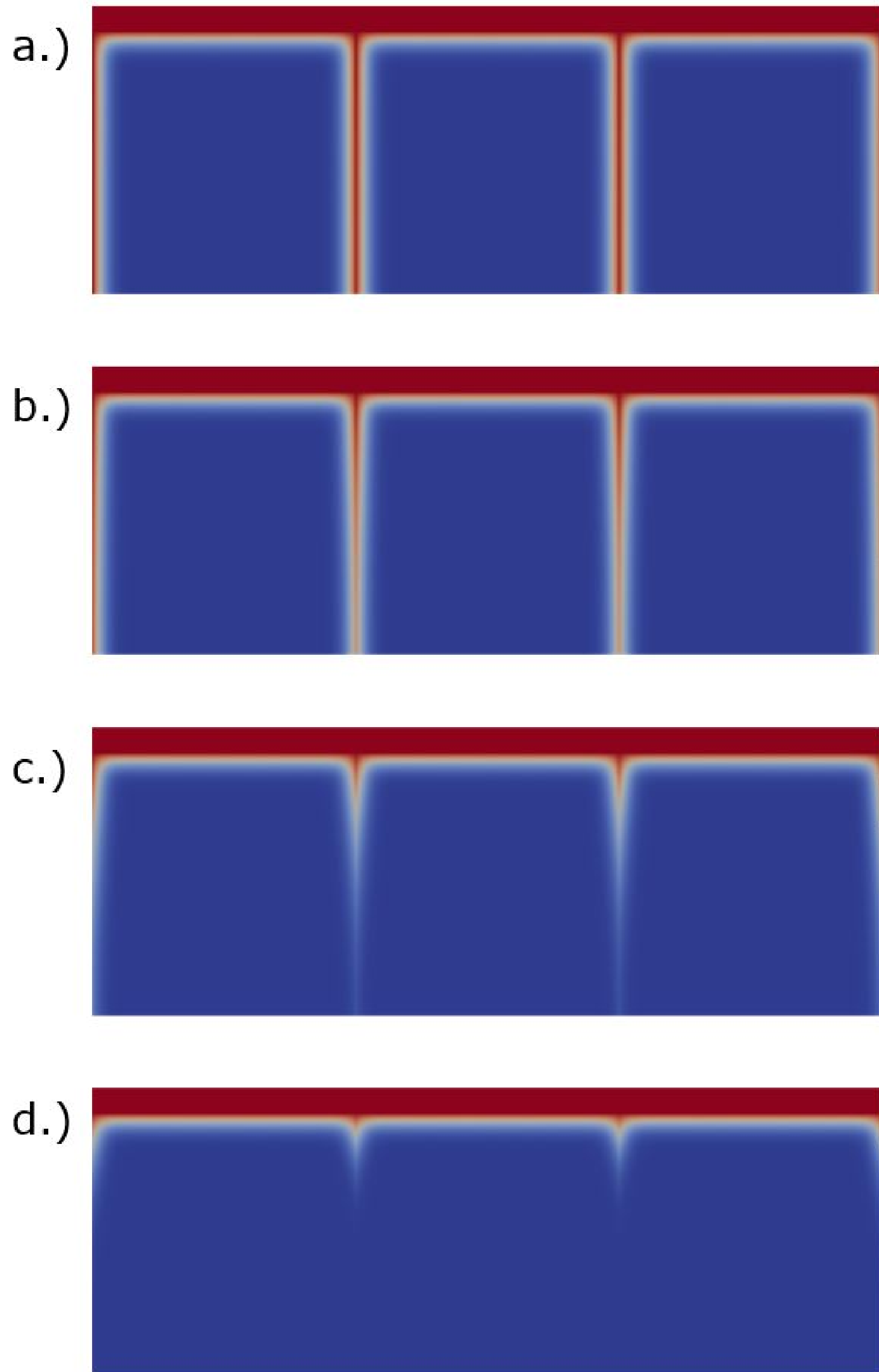

Fig. 6.4: Simulation of a diffusion system with columnar grains and grain boundaries orientated at an angle of 90 $^\circ$ with respect to the surface with D_{bulk} of 10^{-16} cm^2 for a duration of 1000 s and various grain boundary diffusion coefficients: a.) $D_{gb} = 10^{-9}$ cm^2/s; b.) $D_{gb} = 10^{-10}$ cm^2/s; c.) $D_{gb} = 10^{-11}$ cm^2/s; d.) $D_{gb} = 10^{-12}$ cm^2/s; The concentration is coded in a linear color scale: blue = 0, red = 1

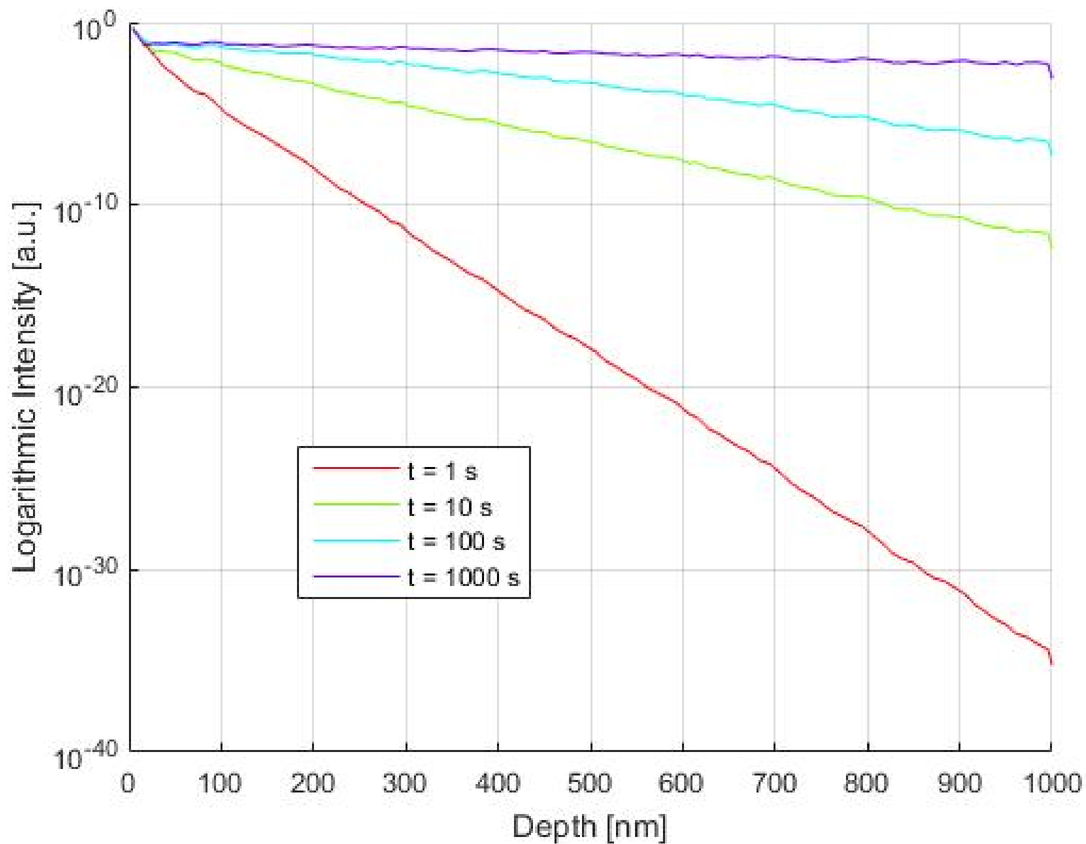

Fig. 6.5: Depth profile of the atom concentration for a diffusion system with columnar grains and grain boundaries orientated at an angle of 90 ° with respect to the surface with $D_{gb} = 10^{-12}$ cm^2/s and D_{bulk} of 10^{-16} cm^2/s for a duration of 1000 s

In the first simulation a classical type-B regime of diffusion is observed. Atoms diffuse fast through the grain boundaries, while bulk diffusion is negligible and significantly starts with longer annealing duration (Fig. 6.2). Furthermore as seen in Fig. 6.2 d.), diffusion from the grain boundaries into the grains starts leading to an approximated U-shaped diffusion profile (comparison to Harrison: Fig. 2.4, b-type). The depth profile (Fig. 6.3) shows bulk diffusion within the first 100 nm at the 1000 s curve. In comparison to that, the overall intensity in the second simulation is several magnitudes lower than in the first one showing, that differences in diffusion coefficient have a big impact on the simulation results. This explains, why an exact determination of diffusion coefficients is necessary for a proper simulation. The diffusion coefficient determination via FDM have an uncertainty of approximately half a magnitude due to numerical errors and noise as already discussed in Sec. 5.6. Furthermore, the simulated depth profile should show no noise. This noise seen within the depth profiles (Figs. 6.3 and 6.5) appear due to the finite number of nodes within in the model that could

be avoided using with a finer mesh and more computational power.

If a system shows no reaction processes, i.e., complete miscibility, over a large temperature range, e.g., Ni-Cu, this system can be applied to study bulk diffusion and grain boundary diffusion processes. The next simulation show the diffusion of Ni atoms into Cu using diffusion coefficients experimentally determined by Divinski et al. [8]. The calculated Arrhenius law is implemented into the model, so that the only parameters left are temperature and annealing time (analogous to a temper process in a furnace) and the number of simulation steps. The images show simulated profiles at 800 °C (B-Regime) (Figs. 6.6 and 6.7) for a duration of 1000 s.

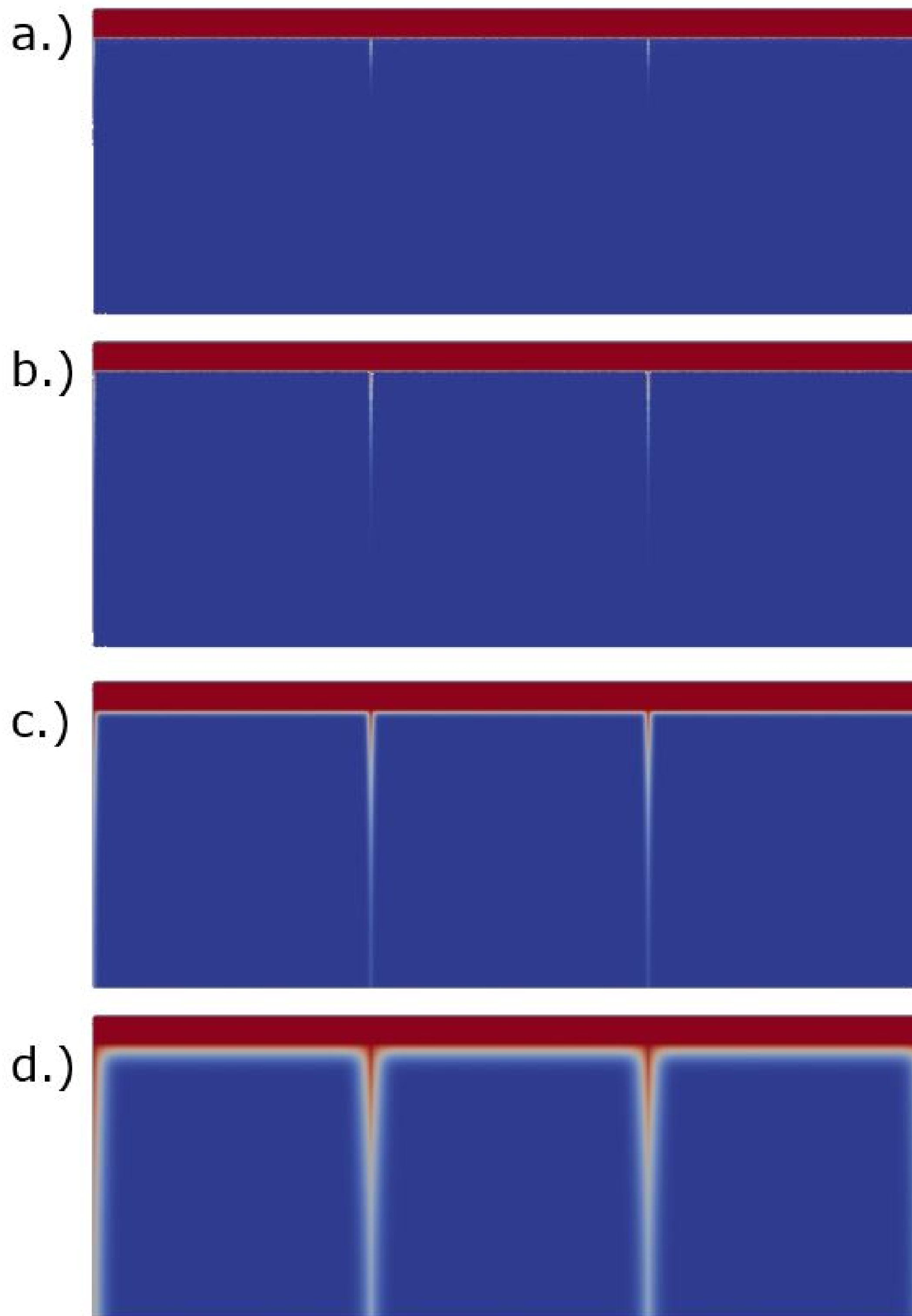

Fig. 6.6: Simulation of diffusion in the Ni-Cu system at a temperature of 800 °C (type-B regime) for a maximum duration of 1000 s using diffusion coefficients determined by Divinski et al. [8]. The grain boundaries are orientated at an angle of 90 ° with respect to the surface. The diffusion times for the different figures are as follows: a.) 1 s; b.) 10 s; c.) 100 s; d.) 1000 s; The concentration is coded in a linear color scale: blue = 0, red = 1

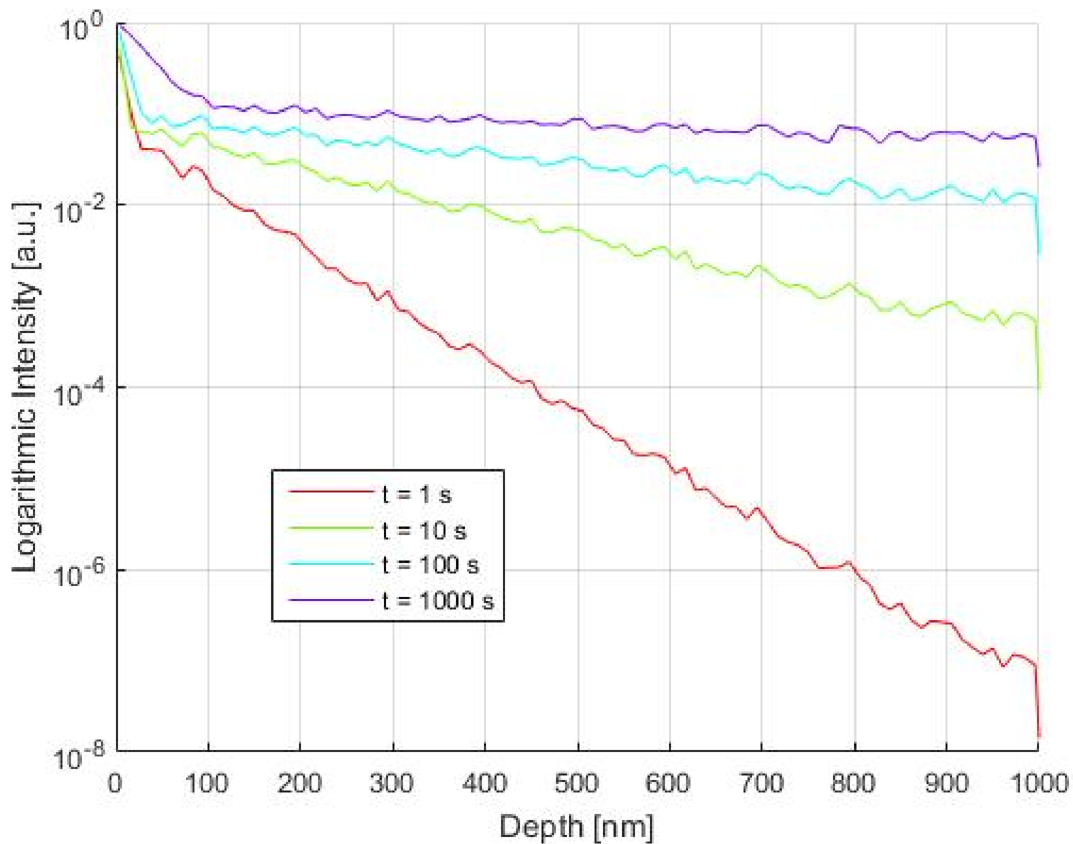

Fig. 6.7: Depth profile of the atom concentration for diffusion in the Ni-Cu system at a temperature of 800 °C (type-B regime) for a maximum duration of 1000 s using diffusion coefficients determined by Divinski et al. [8].

The type-B regime diffusion looks similar to the first example given (Fig. 6.2). Fig. 6.6 a.) and b.) show only grain boundary diffusion while with increasing simulation time, significant bulk diffusion is observed additionally (Fig. 6.6 c.) and d.)). Profiles and results like this can only be compared to real measurements under the assumption that nearly the same grain size and structure is implemented into the model. That is the reason why an exact quantitative comparison to Divinski's results is not possible.

This leads to the fact, that many materials do not show columnar grains like the system used up to now. Grain size and microstructure can vary and form complex arrangements that significantly influence the simulation behaviour. For that reason, a second model, a FIB cut imaged during this thesis was drawn in Gmsh and modelled. This "real" model can be seen in Fig. 6.8. In comparison to the ideal model (Fig. 6.1), the grain boundaries are not arranged at an angle of 90 ° with respect to the surface. Furthermore, there is no uniform

grain size. E.g., the grains closer to the lower TiW-Cu interface are smaller compared to the grains above. The FIB-Cut seen in Fig. 6.8 is a 5 μm broad part of the sample deposited at a temperature of 410 °C with a Cu layer of 4.7 μm.

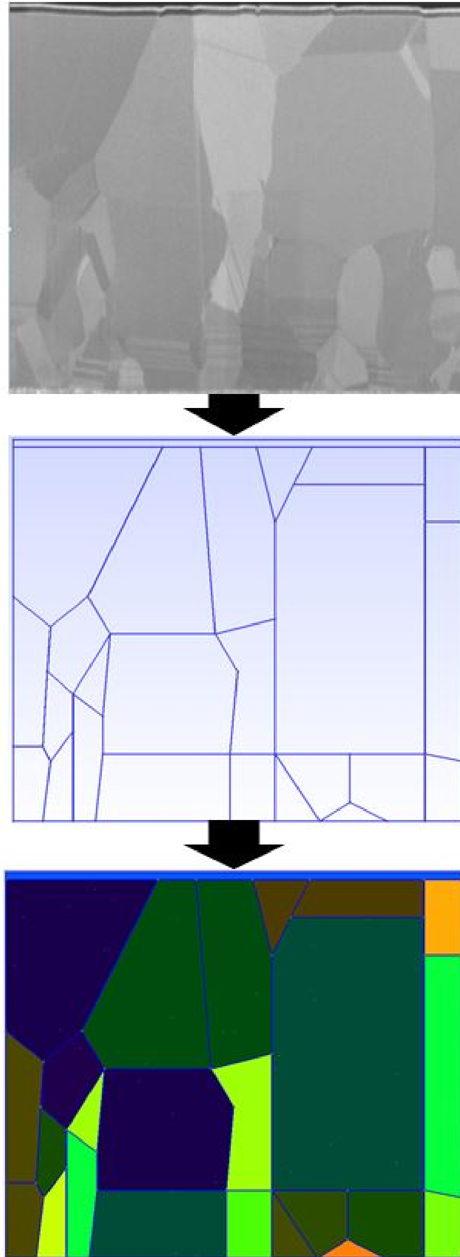

Fig. 6.8: From FIB image to mesh: Here, a SEM image of an layer stack with TiW on top followed by Al and Cu was taken after a FIB cut. The picture was redrawn in Gmsh and meshed with finite CG elements.

The same parameters for the Ni-Cu simulation at 800 °C were now applied to the real model

for a annealing duration of 1000 s. The results can be seen in fig. 6.9 and 6.11.

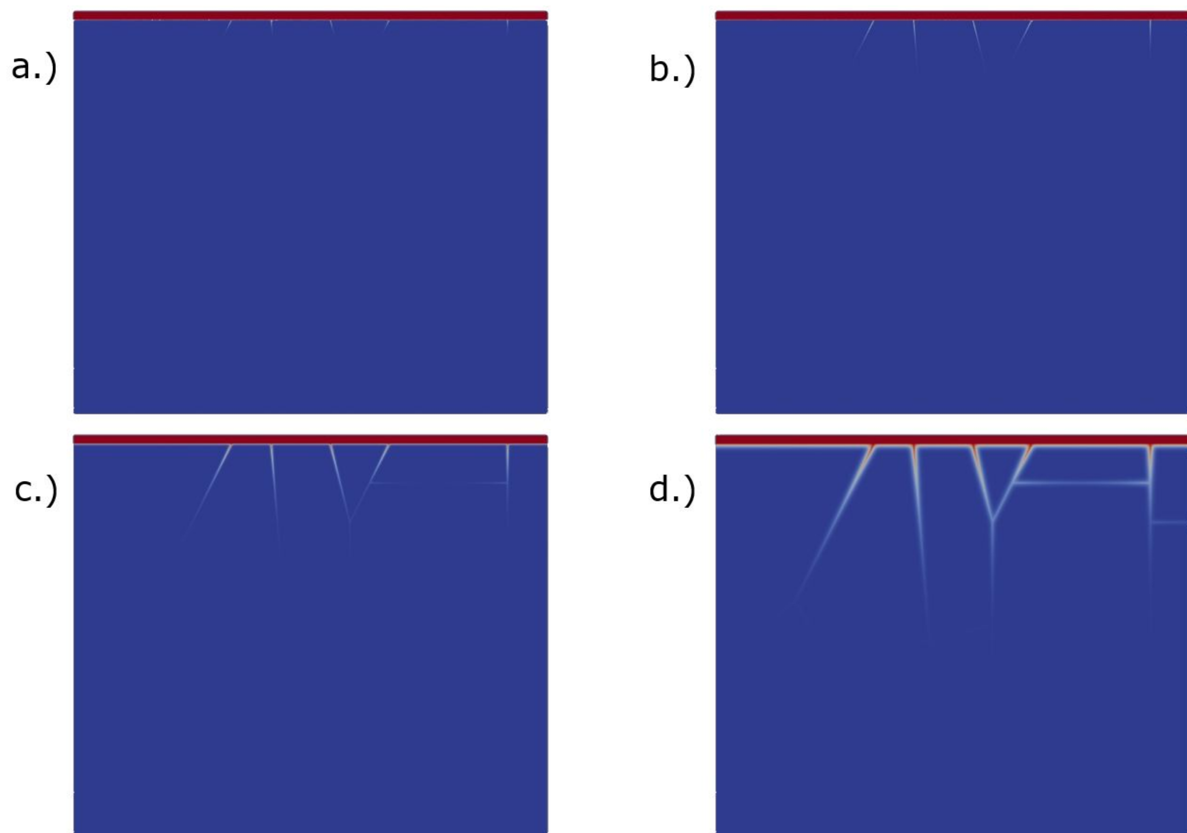

Fig. 6.9: Simulation of diffusion in the Ni-Cu system at a temperature of 800 °C (type-C regime) for a maximum duration of 1000 s using diffusion coefficients determined by Divinski et al. [8] and the real model. The grain boundary orientation has no specific order. The diffusion times for the different figures are as follows: a.) 1 s; b.) 10 s; c.) 100 s; d.) 1000 s; The concentration is coded in a linear color scale: blue = 0, red = 1

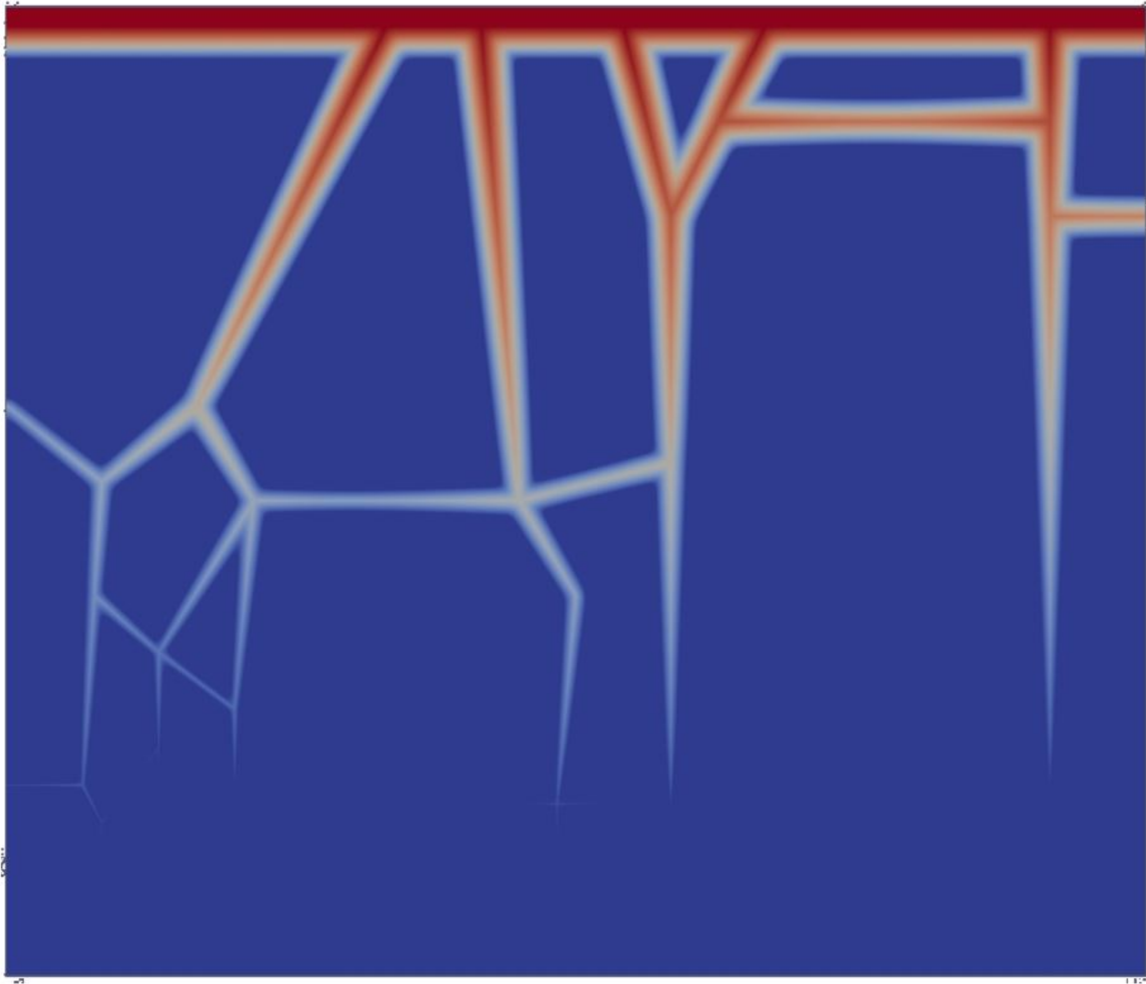

Fig. 6.10: Logarithmic representation of the concentration of the 1000 s simulation step from Fig. 6.9; The concentration is coded in a logarithmic color scale: blue = 0, red = 1

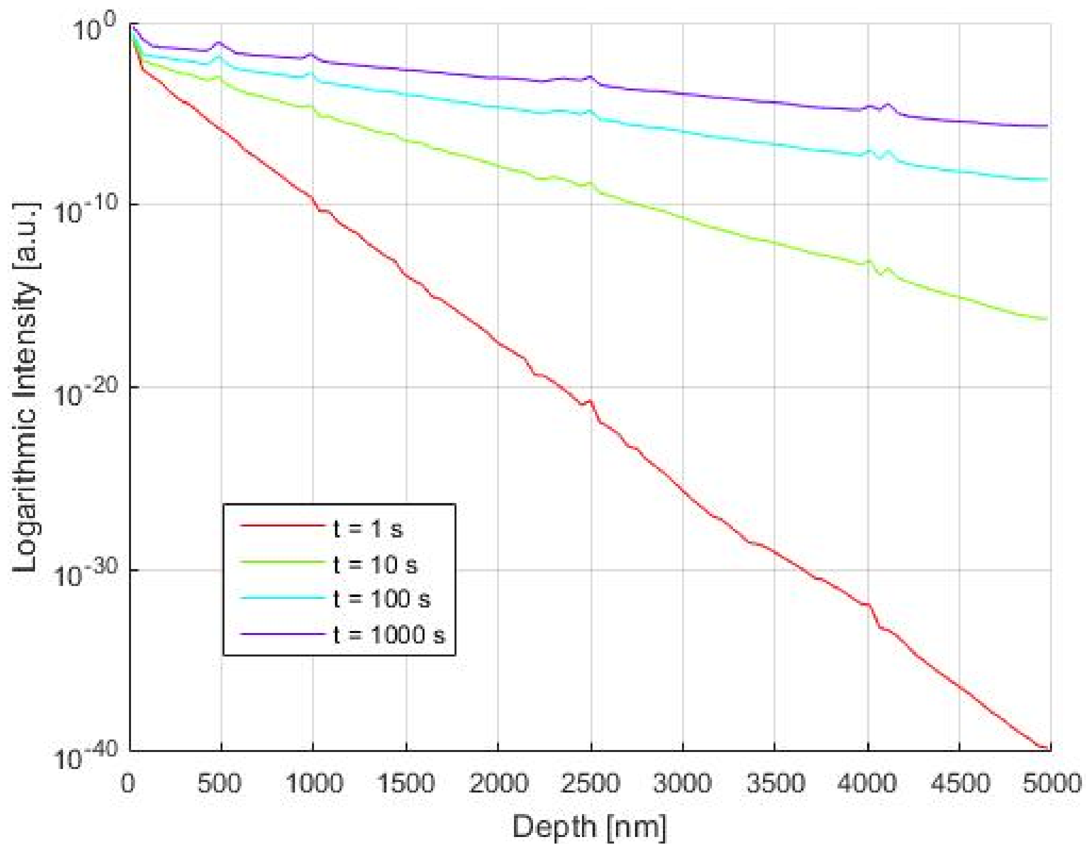

Fig. 6.11: Depth profile of the atom concentraion for diffusion in the Ni-Cu system at a temperature of 800 °C (type-B regime) for a maximum duration of 1000 s using diffusion coefficients determined by Divinski et al. [8] and the real model.

Fig. 6.9 shows the diffusion profiles for the real model at different time staps. With increasing time, the Ni atoms diffuse through the Cu grain boundaries into the material. The logarithmic representation seen in Fig. 6.10 gives a more detailed look at the 1000 s time step. There, diffusion from the grain boundaries in the grains can be seen implying that the chosen diffusion temperature and diffusion time are conditions for b-type diffusion. When looking at the evolution of the depth profiles with time (Fig. 6.11) the signal rises with increasing temperature. Small "peaks" in the depth profile (e.g, at depths of 500 nm, 1000 nm or 2500 nm) are again due to different grain boundary concentrations in the system or due to grain boundary orientation, e.g., horizontal grain boundaries. Compared to Fig. 6.7, the signal is a bit lower because of a higher distance between neighbouring grain boundaries. That shows again, that a good knowledge of the microstructure of the sample is needed before a precise simulation is possible. This calculation shows, that practically every structure can be simulated with a proper model and enough computational power.

6.2 The Diffusion-Reaction Model

The next step to a more complete description of Al-Cu interaction processes is adding additional effect to diffusion using the source terms. The so far most important influence beside diffusion is reaction, which was added using the Gray-Scott model (Sec. 4.2.4). For computational reasons, the ideal model with columnar grains (Fig. 6.1) is used. As mentioned in Sec. 6.1, there is no Arrhenius law available for Al-Cu and therefore, values for D_b and D_{gb} where estimated using the ToF-SIMS depth profiles presented in Sec. 5.4 for an anneal at 200 $^{\circ}$C. For the reaction-diffusion model, further parameters describing the reaction behaviour have to chosen as well. As, according to Tan YY [6], the Al_2Cu phase is the first one to form, kill and feed rate were adjusted that the phase formation behaviour matches the one observed in this work.

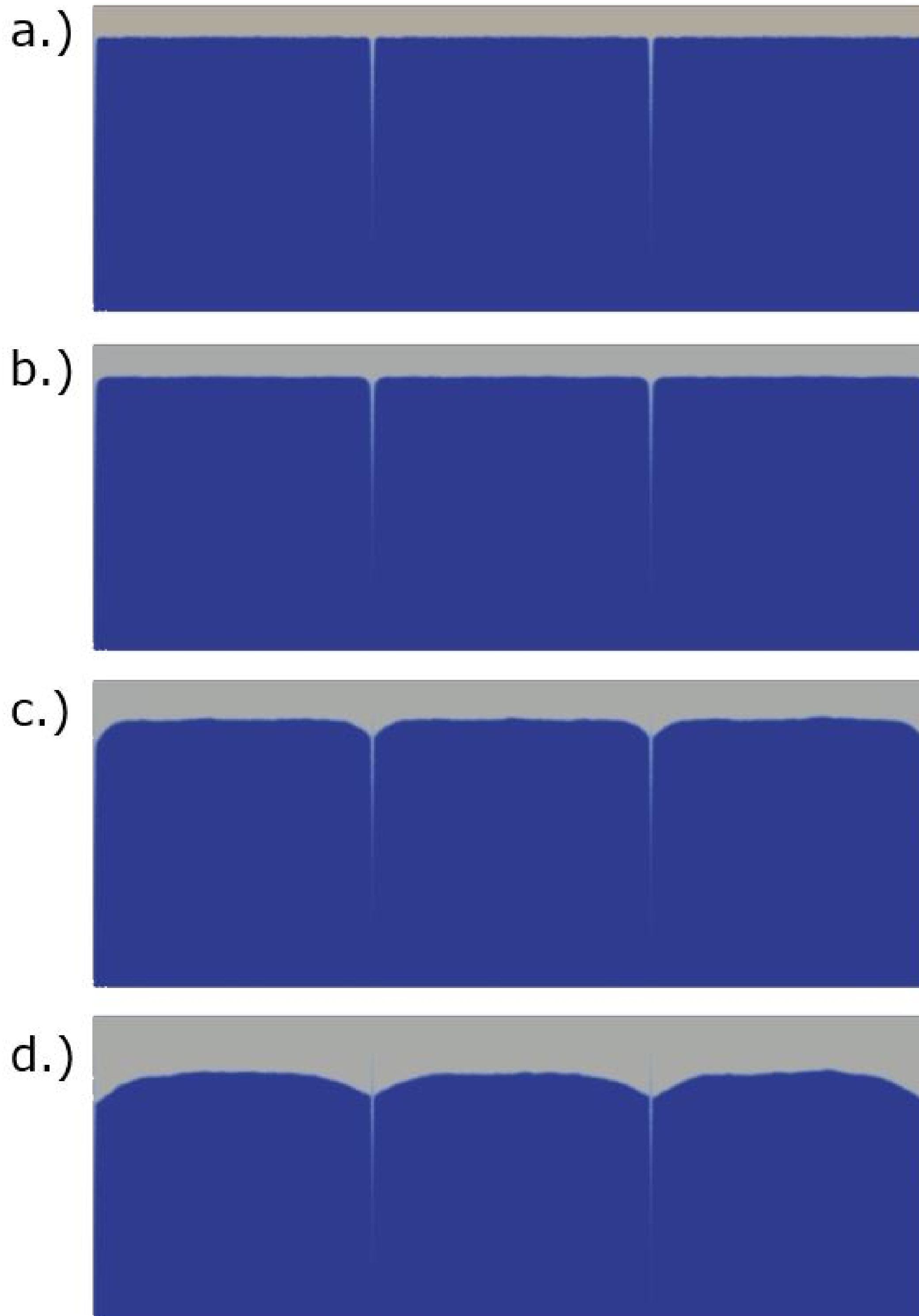

Fig. 6.12: Simulation of reaction-diffusion in the Al-Cu system at a temperature of approximately 200 °C for a maximum duration of 3600 s. The grain boundary are orientated at an angle of 90 ° with respect to the surface. The diffusion times for the different figures are as follows: a.) 18 s; b.) 90 s; c.) 990 s; d.) 3600 s; The concentration is coded in a linear color scale: blue = 0, red = 1, grey represents the phase

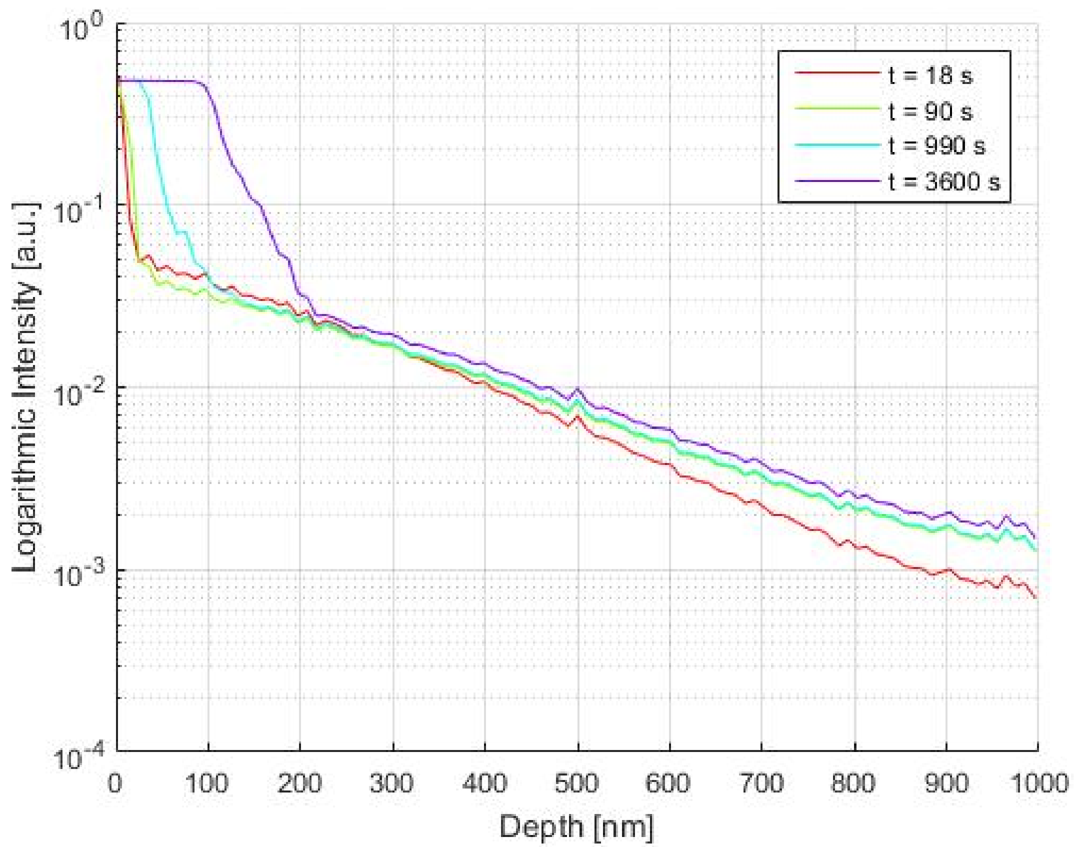

Fig. 6.13: Depth profile of the Al concentration for reaction-diffusion in the Al-Cu system at a temperature of approximately 200 °C for a maximum duration of 3600 s. The grain boundaries are orientated at an angle of 90 ° with respect to the surface.

Figure 6.13 can now be compared to the measured ToF-SIMS depth profile for the sample annealed at 200 °C for 8 h in Fig. 6.14. For easier comparison, this figure is plotted again at this point.

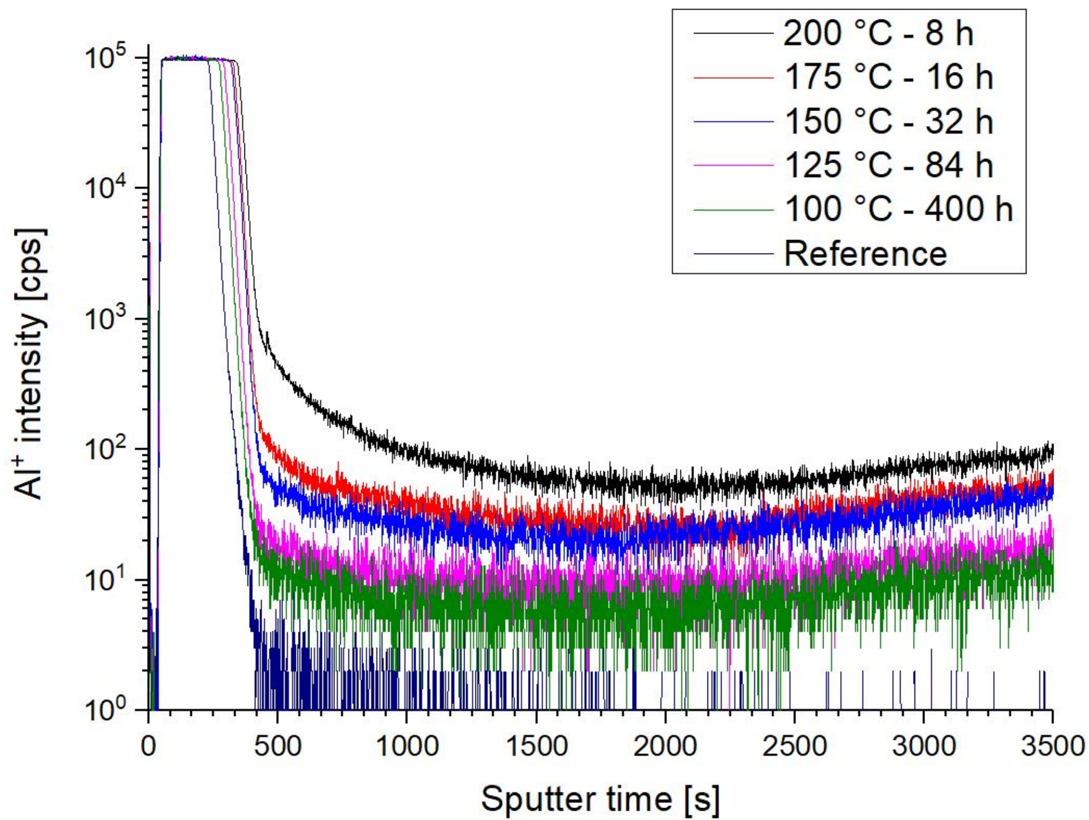

Fig. 6.14: ToF-SIMS depth profiling of the Al concentration for annealing up to 200 °C. There, the sputter time is plotted versus the logarithm of the Al^+ intensity. The depth is proportional to the sputtering time if a constant ToF-SIMS sputter rate is assumed.

The first interesting fact are the processes of phase formation and phase growth. In Fig. 6.12 a.) to d.), a growth of the gray Al layer into the blue Cu grains can be seen. This growth is the process of phase formation, meaning that Al signal can be detected in the Cu layer due to a specific IMC forming. When looking at the depth profile in Fig. 6.13, the intensity signal at $t = 1000$ s seems to be at a constant level. This means that the Al is already consumed by the phase and growing into the Cu layer. The same effect can be observed in the real measurement (Fig. 6.14) as well. The Al signal of the sample annealed at 200 °C for 8 h falls off later compared to the samples with less or no phase formation.

The next remarkable detail is the shape of the Al layer especially in Fig. 6.12 c.) and d.). There, kind of horns are forming at the position of the grain boundaries implying that an enhanced concentration of the Al atoms can be found there. Furthermore it allows the hypothesis, that IMC formation at first takes place at the grain boundaries, where more

material for reaction is available. A look at the depth profile in Fig. 6.13 shows a sharp decrease between a depth from 100 and 200 nm. This can be explained with the enhanced Al concentration at the grain boundaries. The sharp descend appears due to phase formation and can be interpreted as an additional layer with different diffusion behaviour. This can be observed again in the real measurement as well. The signal of the sample annealed at 200 °C for 8 h shows this kind of behaviour at sputter times betweeen 500 and 700 seconds. Furthermore, this fact was observed in the nanoSIMS images (Fig. 5.26), where the Al and Cu signal hotspots were located at the grain boundaries.

The last part in Fig. 6.12 is the gray line along the grain boundaries. This is classical grain boundary diffusion. After some time, this stops because no more material is available and the whole Al layer has reacted. In the depth profile in Fig. 6.13, this fact can be seen at depths from 200 to 900 nm. The signal shows a stable decent, where the slope is proportional to the grain boundary diffusion coefficient. Here, the real measurement (Fig. 6.14) looks a bit different. From 700 to approximately 1700 seconds sputter time, this decreasing behaviour can be seen as well. After that, the Al signal starts to rise again due to effects like saturation, smaller grains or ToF-SIMS interface effects. This can not be observed in the simulated profile, were saturation effects and sputtering effects are not possible. Those interactions could only be considered by adding additional terms to the model, what was not part of this work.

7 Summary

Thornton's diagram shows the two main influences for grain structure and size during Ar sputtering: pressure and temperature. While varying the pressure from 3 to 10 mTorr shows no significant impact on grain behaviour, the substrate temperature seems to be the dominant parameter. FIB and AFM images show grain size changes from a few nm to several μm, meaning that varying the temperature from 60 °C to 400 °C is a way to adjust the grain size for applications. It has to be taken into account, where this layer system will actually be used afterwards; if the temperature gets higher than during the production process, the grains will grow further.

The investigation of reaction-diffusion processes was the next point of focus. As prior studies [6] and the phase diagram show, the Al-Cu system allows combinations with many possible stabile phases. As a critical temperature, 175 °C has been defined. Below that temperature no significant reaction processes are observed and bulk and grain boundary diffusion investigations of Al in Cu can be performed. Unfortunately, the temperature range from 100 °C to 175 °C is too small to determine Arrhenius parameters for bulk and grain boundary diffusion and so, only qualitative investigations were possible. Another fact beside the starting phase formation at 175 °C is the upcoming diffusion of Cu in Al, that leads to the theory of reaction-diffusion. The first phases that can be found are the Al_2Cu and the Al_4Cu_9 phase. With increasing temperature and time, the Al rich phases are more and more replaced by Cu rich phases [6]. From the mechanical point of view, diffusion of Al in Cu as well as phase formation lead to a change in hardness of the whole stack. In the diffusion zone, an increase in hardness due to grain boundary diffusion can be observed in the range from 100 to 175 °C. At higher temperatures, mechanical properties of phases or the Al layer itself tend to dominate the hardness measurements.

For the simulation, two different approaches were used. At first, a diffusion-only system was modelled. As an example, diffusion of Ni in Cu as a system, where no reaction processes over a wide temperature range take place, was used. Furthermore, many of those material combinations have already been investigated experimentally, so that the simulation can be started with approved diffusion coefficients. Classical B- and C-regime diffusion according to the Fickian laws and Whipple-LeClaire [13, 14] can be visualized for any kind of geometry.

Starting from this point, a kind of qualitative computational analysis of reaction-diffusion

processes was also possible using the semi-empirical Gray-Scott model. According to those simulations, reaction processes seem to take place preferentially at grain boundaries. One possible explanation could be the enhanced Al concentration within the grain boundaries due to diffusion processes. Furthermore, it explains the effect of enhanced Al signal intensity in ToF-SIMS depth profiles between the Al-Cu interface and the grain boundary diffusion zone. Additional nanoSIMS measurements seem to prove this fact.

References

[1] Helmut Mehrer. *Diffusion in solids*. Springer, 2007.

[2] Thaddeus B. Massalski, Hiroaki Okamoto, P.R. Subramanian, and Linda Kacprzak, editors. *Binary Alloy Phase Diagrams - Second Edition*, volume 1 - Ac-Ag to Ca-Zn. ASM International - The Materials Information Society, 1991.

[3] Thaddeus B. Massalski, Hiroaki Okamoto, P.R. Subramanian, and Linda Kacprzak, editors. *Binary Alloy Phase Diagrams - Second Edition*, volume 2 - Cd-Ce to Hf-Rb. ASM International - The Materials Information Society, 1991.

[4] J.A. Thornton. Influence of apparatus geometry and deposition conditions on the structure and topography of thick sputtered coatings. *Journal of vaccum science and technology*, 11(666), 1974.

[5] H.P. Langtangen and Anders Logg. *Solving PDEs in Minutes - The FEniCS Tutorial Volume 1*, 2016.

[6] Yik Yee Tan, Heinrich Koerner, Juergen Walter, Sergey Ananiev, and Robert Bauer. Growth and reactivity of al-cu intermetallic compounds under ideal conditions. In *Proceedings of MAL Technical and Innovation Symposium 2016*, 2016.

[7] S. Divinski, M. Lohmann, and Chr. Herzig. Ag grain boundary diffusion and segregation in cu: Measurements in the types b and c diffusion regimes. *Acta Materialia*, 49:249–261, 2001.

[8] Sergiy Divinski, Jens Ribbe, Guido Schmitz, and Christian Herzig. Grain boundary diffusion and segregation of ni in cu. *Acta Materialia*, 55:3337–3346, 2007.

[9] Martin Eden Glicksman. *Diffusion in solids - Field Theory, Solid-State Principles and Applications*. John Wiley & Sons, 2000.

[10] Till Froemling. *Oxide Ion Transport in Donor Doped Lead Zirconate Titanate*. PhD thesis, TU Vienna, 2011.

[11] A.E. Austin and N.A. Richard. Grain-boundary diffusion. *Journal of Applied Physics*, 32(8):1462–1471, 1961.

[12] L.G. Harrison. Influence of dislocation on diffusion kinetics in solids with particular reference to the alkali halides. *Transactions of the Faraday Society*, 57:1991, 1961.

[13] R.T.P. Whipple. Diffusion processes in thin films. *Philos. Mag*, 45:1225, 1954.

[14] A.D. LeClaire. The analysis of grain boundary diffusion measurements. *Brit. J. Appl. Phys.*, 14:351, 1963.

[15] P. Fielitz, G. Borchardt, and M. Schmuecker. How to measure volume diffusivities and grain boundary diffusivities of oxygen in polycrystalline oxides. *Solid State Ionics*, 160:73–83, 2003.

[16] Andre Anders. A structure zone diagram including plasma-based deposition and ion etching. *Thin Solid Films*, 518:4087–4090, 2010.

[17] Donald L. Smith. *Thin-Film Deposition*. McGraw-Hill, 1995.

[18] Hans-Gerd Severin. Sputtern - die erzeugung duenner schichten. *Physik in unserer Zeit*, 17(3):71–79, 1986.

[19] Stefan Krivec. *Investigations of mobile ion transport processes in thin layers upon bias-temperature stress*. PhD thesis, Vienna University of Technology, 2011.

[20] Peter Hoppe, Stephanie Cohen, and Anders Meibom. Nanosims: Technical aspects and applications in cosmochemistry and biological geochemistry. *Geostandards and Geoanalytical Research*, 37(2):111–154, 2013.

[21] J. Goldstein, D.E. Newbury, D.C. Joy, C.E. Lyman, P. Echlin, E. Lifshin, L. Sawyer, and J.R. Michael. *Scanning Electron Microscopy and X-Ray Microanalysis - Third Edition*. Springer, 2003.

[22] Ivo Utke, Stanislav Moshkalev, and Phillip Russell. *Nanofabrication Using Focused Ion and Electron Beams - Principles and Applications*. Oxford Series in Nanomanufacturing, 2012.

[23] David B. Williams and C. Barry Carter. *Transmission Electron Microscopy - A Textbook for Materials Science*. Springer, 2009.

[24] G. Binnig and C. F. Quate. Atomic force microscope. *Physical Review Letters*, 56(9), 1986.

[25] A.C. Fisher-Cripps. Critical review of analysis and interpretation of nanoindentation test data. *Surface & Coatings Technology*, 200:4153–4165, 2006.

[26] J. Hay. Introduction to instrumented indentation testing. *Experimental Techniques*, 2009.

[27] J. Crank. *The Mathematics of Diffusion*. Clarendon Press - Oxford, 1975.

[28] K. Levenberg. A method for the solution of ceratin problems in least squares. *Quart. Appl. Math.*, **2**:164 – 168, 1944.

[29] D. Marquardt. An algorithm for least-squares estimationof nonlinear parameters. *SIAM J. Appl. Math.*, **11**:431 – 441, 1963.

[30] Anders Logg, Kent-Andre Mardal, and Garth Wells, editors. *Automated Solution of Differential Equations by the Finite Element Method*. Springer, 2011.

[31] Mats G. Larson and Fredrik Bengzon. *The Finite Element Method: Theory, Implementation and Applications*. Springer, 2013.

[32] Mark S. Gockenbach. *Understanding and Implementing the Finite Element Method*. Society of Industrial and Applied Mathematics, 2006.

[33] N.K. Möse. Development of a simulation framework to study moisture propagation in packaged electronic devices. Master's thesis, Universität Bremen, 2016.

[34] M.R. Sörensen, Yuri Mishin, and A.F. Voter. Diffusion mechanism in cu grain boundaries. *Physical Review B*, 62(6), 2000.

[35] P. Gray and S.K. Scott. Sustained oscillations and other exotic patterns of behavior in isothermal reactions. *J. Phys. Chem.*, 89:22–32, 1985.

[36] K.T. Aust, R.E. Hanneman, P. Niessen, and J.H. Westbrook. Solute induced hardening near grain boundaries in zone refined metals. *Acta Metallurgica*, 16(3):291–302, 1968.

[37] K. Lu, L. Lu, and S. Suresh. Stregthening materials by engineering coherent internal boundaries at the nanoscale. *Science*, 324(5925):349–352, 2009.

Appendix

Python-Code for Diffusion Simulation Using FEniCs

```python
from fenics import *
import numpy as np
import matplotlib.pyplot as plt
import time
import os

print 'FEM Simulation for Diffusion Processes V1.0'
print '(C) Manuel Kleinbichler (IFAT FE UPD 3)'
print 'September 2017'
print ''

diffusionSystem = 1     # 1: Al-Cu, 2: Ni-Cu, 3: Ag-Cu
T = 1000                # Diffusion time
Temp = 100              # System temperature
lin_log = 2             # 1 = log, 2 = lin - Scale
num_steps = 100         # No. of iteration steps
k_boltz = 8.62E-05      # Boltzmann constant
c0 = 1                  # Initial conentration

#T = T*3600
Temp = Temp + 273.15
tic = time.clock()

dt_log = np.zeros(num_steps+1)
dt_log[1:] = np.logspace(0,np.log10(T),num_steps)
dt_lin = T / num_steps
n = 0

if lin_log == 1:
        stepTypeName = 'log'
else:
        stepTypeName = 'lin'
        dt = T / num_steps

TName = str(T)+'s_'
TempName = str(Temp)+'K_'
numStepsName = str(num_steps)+'steps_'
meshName = 'meshMedium'          # Name of Gmsh model file

dataLinescan = np.zeros(100)
dataLinescan = np.reshape(dataLinescan,(len(dataLinescan),1))


# Function for calculation of diffusion coefficient according to Arrhenius law
def Arrhenius(Ea,D0,Temp,k_boltz):
        Diff = D0*exp(Ea/(Temp*k_boltz))
        return Diff

# Function for LineScan
def LineScan(u_vec,V,mesh,t,dataLinescan):

        # Initialization
        interval = 100                           # Intersections for LineScan
        depth = np.linspace(0,-1100,interval)    # Boundaries for intersections
        concentration = np.zeros(interval)       # Pre-calibration for concentration
        depthPlot = np.zeros(interval)           # Final depth for plot
        concentration[0] = c0
        depthPlot[0] = 0

        # Extraction of values as function of depth
        coordinates = V.tabulate_dof_coordinates()
        n = V.dim()
        d = mesh.geometry().dim()
        coordinates.resize((n,d))
        y_coor = coordinates[:,1]
        y_coor = y_coor[1::2]
```

```
67          u_vec = u_vec[1::2]
68
69          # Averaging and scanning
70          print 'LineScan running'
71          ticLinescan = time.clock()
72          for i in range(interval -1):
73
74                  L = y_coor <= depth[i]
75                  depthUpperLimit = y_coor[L]
76                  concUpperLimit = u_vec[L]
77
78                  L1 = depthUpperLimit >= depth[i+1]
79                  depthRange = depthUpperLimit[L1]
80                  concRange = concUpperLimit[L1]
81
82                  depthFinal = np.mean(depthRange)
83                  concFinal = np.mean(concRange)
84
85                  concentration[i+1] = concFinal
86                  depthPlot[i+1] = depthFinal
87
88          # Extraction and Plot
89          tocLinescan = time.clock()
90          executionLinescan = tocLinescan-ticLinescan
91          fig1 = plt.gcf()
92          plt.semilogy(pow(np.abs(depthPlot),6/5),concentration)
93          axes = plt.gca()
94          axes.set_ylim([10E-6,1])
95          print np.size(y_coor)
96          fig1.savefig('Solution Files/Diffusion Equation/'+fullFileName+'/'+ ...
97          ... fullFileName+'_time_'+str(round(t))+'s.jpg')
98          plt.clf()
99
100         depthPlot = np.reshape(depthPlot,(len(depthPlot),1))
101         concentration = np.reshape(concentration,(len(concentration),1))
102         dataLinescan = np.concatenate((dataLinescan,depthPlot,concentration),axis=1)
103         print 'LineScan finished: ',executionLinescan,' s'
104         print ' '
105         return dataLinescan
106
107 # Ea and D0 from Data in papers, calculated in Excel-File
108 # Diffusion coefficient calculation via Arrhenius law
109 # Al-Cu Diffusion (Option 1)
110 if diffusionSystem == 1:
111         diffName = 'AlCu_'
112         Ea_gb_al_c = -1.53E-01
113         D0_gb_al_c = 9.53E-12
114         D_bulk = 8E-16
115         D_gb = 1E-10
116
117 # Ni-Cu Diffusion (Option 2)
118 elif diffusionSystem == 2:
119         diffName = 'NiCu_'
120         if Temp <= 700:
121                 Ea_gb_niv_c = -9.36E-01
122                 D0_gb_niv_c = 6.86E-07
123                 D_bulk = 10E-30
124                 D_gb = Arrhenius(Ea_gb_niv_c,D0_gb_niv_c,Temp,k_boltz)
125         else:
126                 Ea_gb_niv_b = -9.52E-01
127                 D0_gb_niv_b = 9.72E-07
128                 D_bulk = 7E-5*exp(-225000/(8.314*Temp))
129                 D_gb = Arrhenius(Ea_gb_niv_b,D0_gb_niv_b,Temp,k_boltz)
130
131         print D_gb
132         print D_bulk
133
134 # Ag-Cu Diffusion (Option 3)
135 elif diffusionSystem == 3:
136         diffName = 'AgCu_'
137         if Temp <= 600:
138                 Ea_gb_ag_c = -1.1
```

```
139                 D0_gb_ag_c = 6.1E-5
140                 D_bulk = 10E-30
141                 D_gb = Arrhenius(Ea_gb_ag_c, D0_gb_ag_c, Temp, k_boltz)
142         else:
143                 Ea_gb_ag_b = -1.02
144                 D0_gb_ag_b = 1.5E-5
145                 D_bulk = 0.61E-4*exp(-194400/(8.314*Temp))
146                 D_gb = Arrhenius(Ea_gb_ag_b, D0_gb_ag_b, Temp, k_boltz)
147
148 fullFileName = diffName+TempName+TName+numStepsName+stepTypeName+'_'+meshName
149 if not os.path.exists('Solution Files/Diffusion Equation/'+fullFileName):
150         os.makedirs('Solution Files/Diffusion Equation/'+fullFileName)
151
152 # Boundary Conditions
153 class upperBoundary(SubDomain):
154         def inside(self,x,on_boundary):
155                 return between(x[0], (0.0, 6000.0)) and between(x[1], (0.0, 1000.0))
156
157
158 # class for assigning D to area
159 class D(Expression):
160         def __init__(self, material, D1, D2, **kwargs):
161                 self.material = material
162                 self.D1 = D1
163                 self.D2 = D2
164
165         def eval_cell(self, values, x, cell):
166                 if self.material[cell.index] == 47:
167                         values[0] = self.D1
168                 else:
169                         values[0] = self.D2
170
171 # Create mesh and define function
172 mesh = Mesh(meshName+'.xml')
173 V = FunctionSpace(mesh, 'P', 1)
174 u_D = Constant(0.0)
175
176 c0 = 100
177 upperBoundary = upperBoundary()
178 bc = DirichletBC(V, c0, upperBoundary)
179
180 # Subdomain-Management
181 material = MeshFunction('size_t',mesh,meshName+'_physical_region.xml')
182 D_bulk = D_bulk*10E+14
183 D_gb = D_gb*10E+14
184
185 D = D(material, D_bulk, D_gb, degree=0)
186 u_n = interpolate(u_D, V)
187
188 # Define variational problem
189 u = TrialFunction(V)
190 v = TestFunction(V)
191 f = 0
192
193 F = u*v*dx + D*dt*inner(grad(u),grad(v))*dx - (u_n+dt*f)*v*dx
194 a, L = lhs(F), rhs(F)
195 vtkfile = File('Solution Files/Diffusion Equation/'+fullFileName+'/'+fullFileName+'.pvd')
196
197 # Time-stepping
198 u = Function(V)
199 t = 0
200 numCount = 1
201 vtkfile << u,t
202
203 for n in range(num_steps):
204
205         # Update current time
206         ticStep = time.clock()
207         print 'Step ',numCount,' of ',num_steps
208         t += dt
209         u_D.t = t
210         print 'Simulation Time: ',t,' s'
```

```
211
212         # Compute solution
213         solve(a == L, u, bc)
214         numCount = numCount+1
215         vtkfile << u,t
216
217         # LineScan
218         u_vec = u.vector().array() # Fenics Data to np.array
219         dataLinescan = LineScan(u_vec,V,mesh,t,dataLinescan)
220
221         # Update solution
222         u_n.assign(u)
223         tocStep = time.clock()
224         stepExecutionTime = tocStep-ticStep
225         print 'Step execution time: ',stepExecutionTime,' s'
226         print ''
227
228 np.savetxt('Solution Files/Diffusion Equation/'+fullFileName+'/'+fullFileName+'_dp.txt',dataLinescan)
229
230 toc = time.clock()
231 executionTime = toc-tic
232
233 print 'Overall execution time: ',executionTime,' s'
```

Python-Code for Diffusion-Reaction Simulation Using FEniCs

```
1  from fenics import *
2  import numpy as np
3  import matplotlib.pyplot as plt
4  import time
5  import os
6
7  print 'FEM Simulation for Diffusion-Reaction Processes V1.0'
8  print '(C) Manuel Kleinbichler (IFAT FE UPD 3)'
9  print 'September 2017'
10 print ''
11
12 diffusionSystem = 1     # 1: Al-Cu, 2: Ni-Cu, 3: Ag-Cu
13 T = 1000                # Diffusion time
14 Temp = 100              # System temperature
15 lin_log = 2             # 1 = log, 2 = lin - Scale
16 num_steps = 100         # No. of iteration steps
17 k_boltz = 8.62E-05      # Boltzmann constant
18 g = 1                   # Coefficient for intermediate term
19 k = 0.045               # "Kill Rate"
20 c = 0.099               # "Feed Rate"
21 c0 = 1                  # Initial conentration
22
23 #T = T*3600
24 Temp = Temp + 273.15
25 tic = time.clock()
26
27 dt_log = np.zeros(num_steps+1)
28 dt_log[1:] = np.logspace(0,np.log10(T),num_steps)
29 dt_lin = T / num_steps
30 n = 0
31
32 if lin_log == 1:
33         stepTypeName = 'log'
34 else:
35         stepTypeName = 'lin'
36         dt = T / num_steps
37
38 TName = str(T)+'s_'
39 TempName = str(Temp)+'K_'
40 numStepsName = str(num_steps)+'steps_'
41 meshName = 'meshMedium'          # Name of Gmsh model file
42
```

```
43  dataLinescan = np.zeros(100)
44  dataLinescan = np.reshape(dataLinescan,(len(dataLinescan),1))
45
46
47  # Function for calculation of diffusion coefficient according to Arrhenius law
48  def Arrhenius(Ea,D0,Temp,k_boltz):
49          Diff = D0*exp(Ea/(Temp*k_boltz))
50          return Diff
51
52  # Function for LineScan
53  def LineScan(u_vec,V,mesh,t,dataLinescan):
54
55          # Initialization
56          interval = 100                          # Intersections for LineScan
57          depth = np.linspace(0,-1100,interval)   # Boundaries for intersections
58          concentration = np.zeros(interval)      # Pre-calibration for concentration
59          depthPlot = np.zeros(interval)          # Final depth for plot
60          concentration[0] = c0
61          depthPlot[0] = 0
62
63          # Extraction of values as function of depth
64          coordinates = V.tabulate_dof_coordinates()
65          n = V.dim()
66          d = mesh.geometry().dim()
67          coordinates.resize((n,d))
68          y_coor = coordinates[:,1]
69          y_coor = y_coor[1::2]
70          u_vec = u_vec[1::2]
71
72          # Averaging and scanning
73          print 'LineScan running'
74          ticLinescan = time.clock()
75          for i in range(interval-1):
76
77                  L = y_coor <= depth[i]
78                  depthUpperLimit = y_coor[L]
79                  concUpperLimit = u_vec[L]
80
81                  L1 = depthUpperLimit >= depth[i+1]
82                  depthRange = depthUpperLimit[L1]
83                  concRange = concUpperLimit[L1]
84
85                  depthFinal = np.mean(depthRange)
86                  concFinal = np.mean(concRange)
87
88                  concentration[i+1] = concFinal
89                  depthPlot[i+1] = depthFinal
90
91          # Extraction and Plot
92          tocLinescan = time.clock()
93          executionLinescan = tocLinescan-ticLinescan
94          fig1 = plt.gcf()
95          plt.semilogy(pow(np.abs(depthPlot),6/5),concentration)
96          axes = plt.gca()
97          axes.set_ylim([10E-6,1])
98          print np.size(y_coor)
99          fig1.savefig('Solution Files/Gray Scott Equation/'+fullFileName+'/'+fullFileName+'_time_'+ ...
100         ... str(round(t))+'s.jpg')
101         plt.clf()
102
103         depthPlot = np.reshape(depthPlot,(len(depthPlot),1))
104         concentration = np.reshape(concentration,(len(concentration),1))
105         dataLinescan = np.concatenate((dataLinescan,depthPlot,concentration),axis=1)
106         print 'LineScan finished: ',executionLinescan,' s'
107         print ' '
108         return dataLinescan
109
110 # Ea and D0 from Data in papers, calculated in Excel-File
111 # Diffusion coefficient calculation via Arrhenius law
112 # Al-Cu Diffusion (Option 1)
113 if diffusionSystem == 1:
114         diffName = 'AlCu_'
```

```
115 	Ea_gb_al_c = -1.53E-01
116 	D0_gb_al_c = 9.53E-12
117 	D_bulk = 8E-16
118 	D_gb = 1E-10
119 
120 # Ni-Cu Diffusion (Option 2)
121 elif diffusionSystem == 2:
122 	diffName = 'NiCu_'
123 	if Temp <= 700:
124 		Ea_gb_niv_c = -9.36E-01
125 		D0_gb_niv_c = 6.86E-07
126 		D_bulk = 10E-30
127 		D_gb = Arrhenius(Ea_gb_niv_c, D0_gb_niv_c, Temp, k_boltz)
128 	else:
129 		Ea_gb_niv_b = -9.52E-01
130 		D0_gb_niv_b = 9.72E-07
131 		D_bulk = 7E-5*exp(-225000/(8.314*Temp))
132 		D_gb = Arrhenius(Ea_gb_niv_b, D0_gb_niv_b, Temp, k_boltz)
133 
134 	print D_gb
135 	print D_bulk
136 
137 # Ag-Cu Diffusion (Option 3)
138 elif diffusionSystem == 3:
139 	diffName = 'AgCu_'
140 	if Temp <= 600:
141 		Ea_gb_ag_c = -1.1
142 		D0_gb_ag_c = 6.1E-5
143 		D_bulk = 10E-30
144 		D_gb = Arrhenius(Ea_gb_ag_c, D0_gb_ag_c, Temp, k_boltz)
145 	else:
146 		Ea_gb_ag_b = -1.02
147 		D0_gb_ag_b = 1.5E-5
148 		D_bulk = 0.61E-4*exp(-194400/(8.314*Temp))
149 		D_gb = Arrhenius(Ea_gb_ag_b, D0_gb_ag_b, Temp, k_boltz)
150 
151 fullFileName = diffName+TempName+TName+numStepsName+stepTypeName+'_'+meshName
152 if not os.path.exists('Solution Files/Gray Scott Equation/'+fullFileName):
153 	os.makedirs('Solution Files/Gray Scott Equation/'+fullFileName)
154 
155 # Class representing the initial conditions
156 class InitialConditions(Expression):
157 	def eval(self, val, x):
158 		if x[1] >= 0:
159 			val[1] = 1
160 			val[0] = 0
161 		else:
162 			val[1] = 0
163 			val[0] = 1
164 
165 	def value_shape(self):
166 		return (2,)
167 
168 # Class for interfacing with the Newton solver
169 class GrayScottEquations(NonlinearProblem):
170 	def __init__(self, a, L):
171 		NonlinearProblem.__init__(self)
172 		self.L = L
173 		self.a = a
174 	def F(self, b, x):
175 		assemble(self.L, tensor=b)
176 	def J(self, A, x):
177 		assemble(self.a, tensor=A)
178 
179 # Class for differentiating between different domains and diffusion coefficients
180 class D(Expression):
181 	def __init__(self, material, D1, D2, **kwargs):
182 		self.material = material
183 		self.D1 = D1
184 		self.D2 = D2
185 
186 	def eval_cell(self, values, x, cell):
```

```
187                 if self.material[cell.index] == 47:
188                         values[0] = self.D1
189                 else:
190                         values[0] = self.D2
191 
192 # Form compiler options
193 parameters["form_compiler"]["optimize"]          = True
194 parameters["form_compiler"]["cpp_optimize"]      = True
195 parameters["form_compiler"]["representation"]    = "quadrature"
196 
197 # Define mesh and function space
198 print 'Creating mesh'
199 mesh = Mesh(meshName+'.xml')
200 V = VectorFunctionSpace(mesh,'CG',1)
201 print 'Mesh completed'
202 
203 # Subdomain-Management
204 material = MeshFunction('size_t',mesh,meshName+'_physical_region.xml')
205 D_bulk = D_bulk*10E+14
206 D_gb = D_gb*10E+14
207 Du = D(material, D_bulk, D_gb, degree=0)
208 Ea_CuAl = -1.399
209 D0_CuAl = 0.647E-4
210 Dv = 10E-21
211 Dv = Dv*10E+18
212 
213 # Define Functions
214 W_init  = InitialConditions(degree=2)
215 phi     = TestFunction(V)
216 dp      = TrialFunction(V)
217 W0      = Function(V)
218 W       = Function(V)
219 print 'Functions defined'
220 
221 # Interpolate initial conditions and split functions
222 W0      = interpolate(W_init,V)
223 W       = interpolate(W_init,V)
224 q, p    = split(phi)
225 u, v    = split(W)
226 u0, v0  = split(W0)
227 print 'Interpolation and Split done'
228 
229 
230 # Weak form of equations
231 F1 = u*q*dx - u0*q*dx + Dv*inner(grad(u), grad(q))*dt*dx  + g*u*v*v*q*dt*dx  - c*(1-u)*q*dt*dx
232 F2 = v*p*dx - v0*p*dx + Du*inner(grad(v), grad(p))*dt*dx  - g*u*v*v*p*dt*dx  + (c+k)*v*p*dt*dx
233 F = F1 + F2
234 
235 # Compute directional derivative about W in the direction of dp (Jacobian)
236 a = derivative(F, W, dp)
237 
238 # Create nonlinear problem and Newton solver
239 problem = GrayScottEquations(a, F)
240 solver = NewtonSolver()
241 solver.parameters["linear_solver"] = "petsc"
242 solver.parameters["convergence_criterion"] = "incremental"
243 solver.parameters["relative_tolerance"] = 1e-2
244 solver.parameters["maximum_iterations"] = 100
245 vtkfile = File('Solution Files/Gray Scott Equation/'+fullFileName+'/'+fullFileName+'_Al.pvd')
246 vtkfile1 = File('Solution Files/Gray Scott Equation/'+fullFileName+'/'+fullFileName+'_Cu.pvd')
247 
248 t = 0.0
249 numCount = 1
250 print 'Solver started'
251 while (t<T):
252 
253         # Update current time
254         ticStep = time.clock()
255 
256         t += dt
257         solver.solve(problem, W.vector())
258 
```

```
259        # LineScan
260        W_test = W.split()[1]
261        W_vec = W.vector().array() # Fenics Data to np.array
262        dataLinescan = LineScan(W_vec,V,mesh,t,dataLinescan)
263        vtkfile << W.split()[0]
264        vtkfile1 << W.split()[1]
265        print 'Simulation Time: ',t,' s'
266
267        # Update solution
268        W0.assign(W)
269        tocStep = time.clock()
270        stepExecutionTime = tocStep-ticStep
271        numCount = numCount + 1
272        print 'Step execution time: ',stepExecutionTime,' s'
273        print ''
274
275 np.savetxt('Solution Files/Gray Scott Equation/'+fullFileName+'/'+fullFileName+'_dp.txt',dataLinescan)
276
277 toc = time.clock()
278 executionTime = toc-tic
279
280 print 'Overall execution time: ',executionTime,' s'
```